Structural Properties of III-Nitride Semiconductors

by

Yong Wei

A Dissertation Presented in Partial Fulfillment
of the Requirements for the Degree
Doctor of Philosophy

Approved November 2014 by the
Graduate Supervisory Committee:

Fernando Ponce, Chair
Andrew Chizmeshya
Martha McCartney
José Menéndez
Hongbin Yu

ARIZONA STATE UNIVERSITY

December 2014

ABSTRACT

Group III-nitride semiconductors have been commercially used in the fabrication of light-emitting diodes and laser diodes, covering the ultraviolet-visible-infrared spectral range and exhibit unique properties suitable for modern optoelectronic applications. InGaN ternary alloys have energy band gaps ranging from 0.7 to 3.4 eV. It has a great potential in the application for high efficient solar cells. AlGaN ternary alloys have energy band gaps ranging from 3.4 to 6.2 eV. These alloys have a great potential in the application of deep ultra violet laser diodes. However, there are still many issues with these materials that remain to be solved. In this dissertation, several issues concerning structural, electronic, and optical properties of III-nitrides have been investigated using transmission electron microscopy. First, the microstructure of $In_xGa_{1-x}N$ (x = 0.22, 0.46, 0.60, and 0.67) films grown by metal-modulated epitaxy on GaN buffer /sapphire substrates is studied. The effect of indium composition on the structure of InGaN films and strain relaxation is carefully analyzed. High luminescence intensity, low defect density, and uniform full misfit strain relaxation are observed for x = 0.67. Second, the properties of high-indium-content InGaN thin films using a new molecular beam epitaxy method have been studied for applications in solar cell technologies. This method uses a high quality AlN buffer with large lattice mismatch that results in a critical thickness below one lattice parameter. Finally, the effect of different substrates and number of gallium sources on the microstructure of AlGaN-based deep ultraviolet laser has been studied. It is found that defects in epitaxial layer are greatly reduced when the structure is deposited on a single crystal AlN substrate. Two gallium sources in the growth of

multiple quantum wells active region are found to cause a significant improvement in the quality of quantum well structures.

To my parents, my wife, and my daughter.

ACKNOWLEDGEMENTS

I would like to gratefully thank my advisor, Prof. Fernando Ponce, for offering me the great opportunity in study of the III-nitrides as well as his academic guidance and support during my attendance at Arizona State University. I would also like to thank my committee members, Prof. Andrew Chizmeshya, Prof. Martha McCartney, Prof. José Menéndez, and Prof. Hongbin Yu.

I want to express my special thanks and appreciation to Dr. Alec Fischer, for his enthusiastic and effective help in my research, in the writing of reports and papers, and in the writing of this dissertation. I have spent a wonderful time working with my knowledgeable and friendly colleagues, and I thank their generous help during my Ph. D studies, they are: Mr. Hongen Xie, Mr. Shuo Wang, Mr. Hanxiao Liu as well as former group members Dr. Qiyuan Wei, Dr. Kewei Sun, Dr. Yu Huang, Dr. Ti Li, Dr. Jingyi Huang, and Dr. Reid Juday. I would like to thank Mr. Karl Weiss, Dr. Zhenquan Liu, Dr. John Mardinly and Dr. Toshihiro Aoki of LeRoy Erying Center for Solid State Science at Arizona State University for their excellent facilities and technical help with TEM.

I sincerely thank my parents for their support throughout my education. I deeply appreciate my wife Yifang Chen for her constant love.

TABLE OF CONTENTS

Page

LIST OF FIGURES

Figure Page

Figure Page

Figure Page

Figure Page

Figure Page

Figure Page

LIST OF TABLES

CHAPTER 1

INTRODUCTION TO GROUP-III NITRIDES

1.1. III-Nitride Materials

Group-III nitrides semiconductors, including AlN, GaN, and InN and their ternary (AlGaN and InGaN), quaternary (AlGaInN), have direct bandgaps ranging from 0.7 eV (InN) to 6.2eV (AlN), covering the spectral range of the infrared, visible, and ultraviolet. There is no other semiconductor material systems has such a wide tunable direct bandgap. It is one of the most important research fronts in both fundamental knowledge and applications. Red, blue, green light emitting devices (LEDs), blue-violet, ultraviolet (UV) laser diodes (LDs), UV light detectors and high power electronic devices have been achieved and commercialized based on group-III nitride materials. Fig 1.1 shows the bandgap and chemical bond length of typical compound semiconductors for optoelectronic applications. Table 1.1 shows some basic constants for group III-nitride semiconductors.

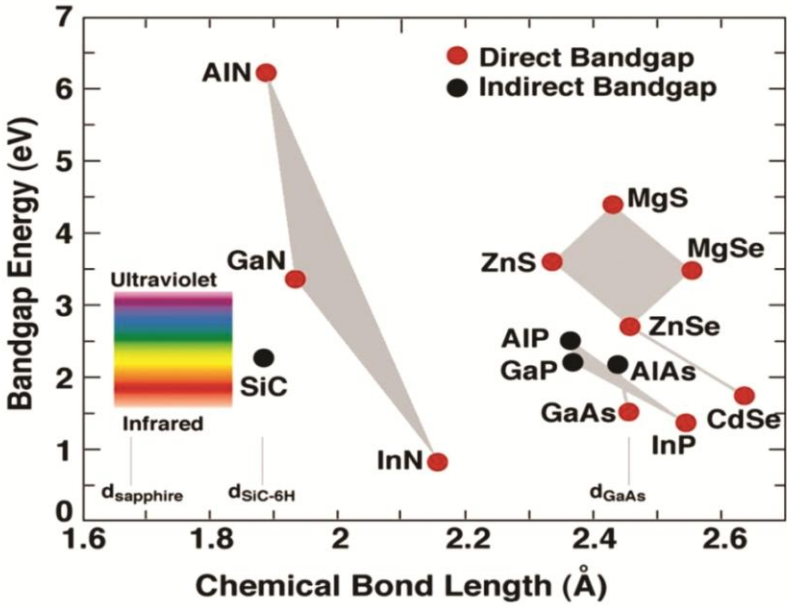

FIG. 1.1. Bandgap energy vs. chemical bond length for compound semiconductors that emit in the visible range of the electromagnetic spectrum.[1]

Table 1.1. Comparison of basic properties of group III-nitride semiconductors.[2][3][4]

Physical Properties	AlN	GaN	InN
Eg (eV)	6.2	3.39	0.7
Thermal Expansion coefficient (300 K)			
a (× 10-6 K-1)	4.2	5.59	5.59
c (× 10-6 K-1)	5.3	3.17	3.7
Bond length (Å)	1.89	1.94	2.15
Cohesive Energy per Bond (eV)	2.88	2.24	1.93
Melting point (^{o}C)	>3000	>2500	>1100
Density (g/cm^{3})	3.26	6.10	6.99

1.2. III-Nitrides Structures

There are mainly two types of crystal structures for group-III nitrides: cubic zincblende and hexagonal wurtzite. Both can coexist under the various parameters used for crystal growth.[5] The cubic structure is thermodynamically metastable and wurtzite structure is thermodynamically stable. The wurtzite structure belongs to the $P6_3mc$ space group with an ABAB stacking sequences along the *c*-direction. Lattice points in hexagonal wurtzite structures are indexed by four indices *h, k, i, l,* where $i = -h - k$. The first three indices correspond to the equivalent *a*-direction vector in the basal plane and the last index corresponds to *c*-direction vector. Figure 1.2 shows fundamental lattice vectors of basal plane in hexagonal structure. For negative vectors, a bar is used over index. In general, indices surrounded by square brackets "[ ]" or angled brackets "< >" are applied to describe a direction and a family of direction, respectively. Indices surrounded by parentheses "( )" and curly brackets "{ }" are used to describe a plane and a family of planes, respectively. It is necessary to point out that [*h k i l*] direction is not the normal to (*h k i l*) plane in real space unless $l = 0$ or $h = k = 0$. In hexagonal lattice system, the equations used to calculate angles between planes and directions are different.[6] In hexagonal systems, the angle between two planes ($h_1\, k_1\, i_1\, l_1$) and ($h_2\, k_2\, i_2\, l_2$):

$$cos\theta = \frac{h_1h_2+k_1k_2+\frac{1}{2}(h_1k_2+k_2h_1)+\frac{3}{4}l_1l_2(\frac{a}{c})^2}{\sqrt{h_1{}^2+k_1{}^2+h_1k_1+\frac{3}{4}l_1{}^2(\frac{a}{c})^2}\sqrt{h_2{}^2+k_2{}^2+h_2k_2+\frac{3}{4}l_2{}^2(\frac{a}{c})^2}} \quad (1.1)$$

The angle between ($h_1\, k_1\, i_1\, l_1$) plane and [$h_2\, k_2\, i_2\, l_2$] direction is:

$$cos\theta = \frac{h_1h_2+k_1k_2+i_1i_2+l_1l_2}{\sqrt{h_1{}^2+k_1{}^2+i_1{}^2+\lambda^2l_1^2}\sqrt{h_2{}^2+k_2{}^2+l_2^2/\lambda^2}} \quad (1.2)$$

The angle between [$h_1\,k_1\,i_1\,l_1$] direction and [$h_2\,k_2\,i_2\,l_2$] direction is:

$$cos\theta = \frac{h_1h_2+k_1k_2+i_1i_2+\lambda^2 l_1 l_2}{\sqrt{{h_1}^2+{k_1}^2+{i_1}^2+\lambda^2 l_1^2}\sqrt{{h_2}^2+{k_2}^2+{i_2}^2+\lambda^2 l_2^2}} \tag{1.3}$$

In the wurtzite structure, the lattice constants *a* and *c* should satisfy the value for a tetrahedron where $c/a = \sqrt{8/3}$ = 1.633 and an internal parameter u = 0.375. We usually use u_c to denote the length of bonds along [0001] direction. Table 1.2 lists lattice constant *a*, c, internal parameter *u*, and *c*/*a* ratio of wurtzite structure. In III- nitrides, the *c*/*a* is slightly smaller than 1.633 and *u* is larger than 0.375. Due to these structure deformations, a relative displacement between the center of the mass of the cations and anions along [0001] direction creates a dipole moment, resulting in an intrinsic spontaneous polarization in the crystal as depicted in Fig. 1.3(a). The strain in material can deform structure and hence further affect the displacement cations and anions, resulting in a piezoelectric polarization as illustrated in Fig. 1.3(b).

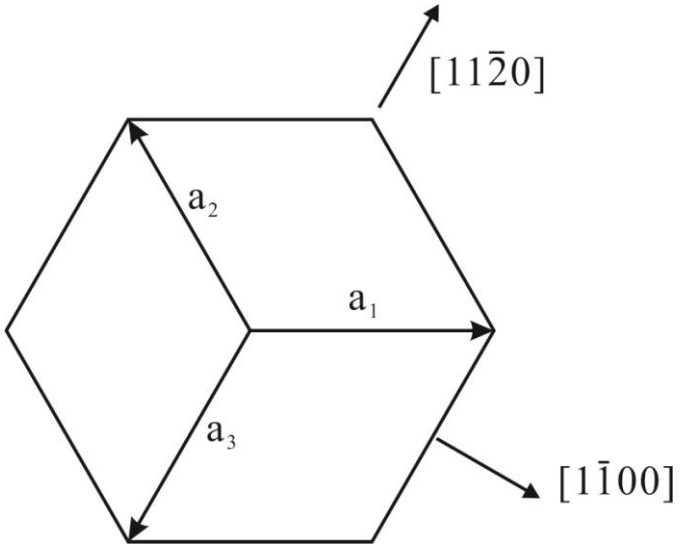

FIG. 1.2. Fundamental lattice vectors of basal plane in hexagonal structure.

Table 1.2. Lattice constant *a*, *c*, internal parameter *u*, and *c*/*a* ratio of wurtzite structure.[7][8]

	a	*c*	*u*	*c/a*
AlN	3.112	4.982	0.38	1.601
GaN	3.189	5.185	0.376	1.626
InN	3.545	5.703	0.377	1.609

.

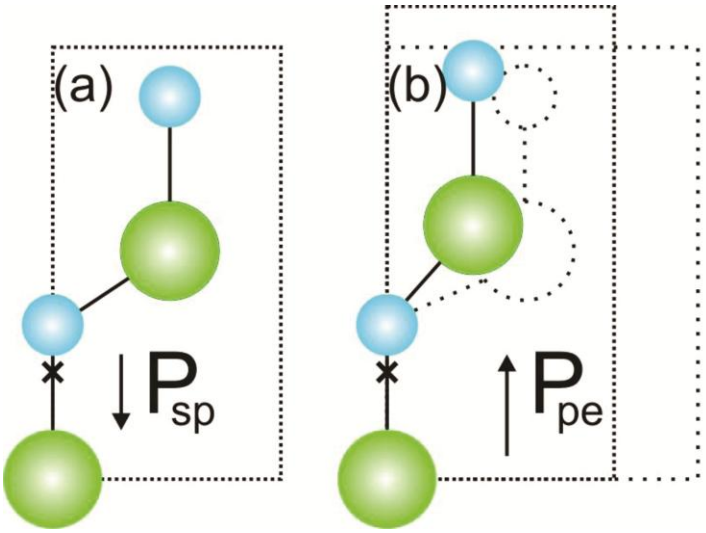

FIG. 1.3. The fields present in wurtzite materials. (a) Spontaneous fields due to natural charge separation; (b) Piezoelectric fields due to induce strain in material.[9]

It is important to point out that the (0001) and $(000\bar{1})$ surfaces of the wurtzite structure are not equivalent and their chemical properties are different. The (0001) and $(000\bar{1})$ polarity depends on whether Ga atoms or N atoms lie at the top of (0002) bilayer as shown in Fig. 1.4. It has been reported that high-quality epitaxial GaN films deposited

by metal organic chemical vapor deposition (MOCVD) on *c*-plane sapphire substrates grow in the (0001) direction with Ga-faced surfaces,[10] while Molecular beam epitaxy (MBE) growth commonly occurs in the $(000\bar{1})$ direction, yielding an N-faced film.[11] The Ga-faced GaN usually has a smooth and more chemically stable surface.

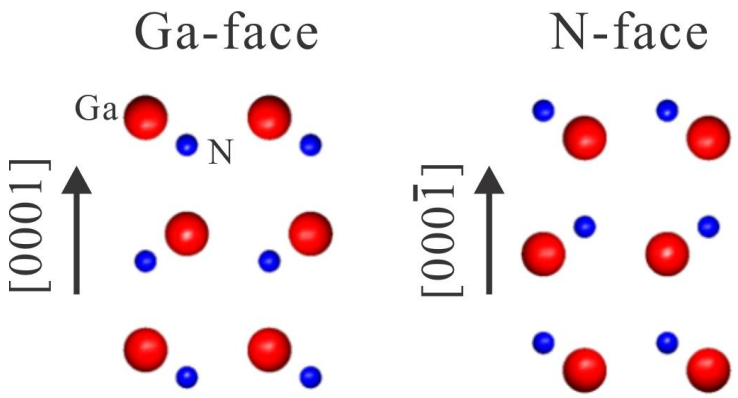

FIG. 1.4. Different polarities (Ga- and N-face) of wurtzite GaN.[12]

1.3. III-Nitride Growth

Growth of high quality III-nitride films is the perquisite for highly-efficient III-nitride based devices. The first single crystalline GaN layer was successfully grown in 1969 by Maruska and Tietjen using the hydride vapor-phase epitaxy (HVPE) technique.[13] For HVPE growth, the gallium and the nitrogen sources are gallium chloride and ammonia. The growth rate of GaN depends linearly on the input partial pressure of gallium chloride. The main advantage of this growth technique is the high growth rate, which offers the possibility to fabricate single crystal GaN for subsequent nitrides epitaxy. However, the film surface using this growth technique is rough.

Metal-organic vapor phase epitaxy (MOVPE) is another commonly used III-nitride growth technique which uses metal organic (e.g., trimethylgallium) gases and ammonia as reactants. GaN are typically deposited on sapphire substrates, the large lattice mismatch between them and their differences in thermal coefficient leads to a GaN film with grains and rough surface. In 1986, Akasaki and Amano found that a thin layer of low temperature AlN buffer could improve the crystalline quality of GaN.[14] This technique is called a "two-step" method. Nowadays, the MOVPE growth is widely used for commercial application in the III-nitrides. It has a relatively high growth rate of ~2 μm/h. The epitaxial film has high quality and usually abrupt interfaces at the atomic scale. MOVPE growth of III nitrides always results in Ga-face polarity irrespective of the nucleation layer used. For MOVPE growth of GaN, the typical growth happens at a temperature of ~1150^{o}C, a nitrogen pressure between 40 and 100 torr, and a V/III ratio of 1000-2000. MOVPE growth of InGaN film requires lower growth temperatures below 1000^{o}C because the In-N bond is thermally unstable for temperatures higher than 630^{o}C.[15] However, the ammonia cracking efficiency is low at temperatures below than 1000^{o}C. In order to compensate these issues, a higher III/V ratio >5000 is usually required with a growth temperature around 700^{o}C-900^{o}C. On the contrary, MOVPE growth of AlGaN requires a higher growth temperature >1100^{o}C because the Al-N bond begins to dissociate at about 1040^{o}C,[15] therefore, a lower V/III ratio <1000 is suggested. Quaternary alloy InAlGaN growth is quite difficult and indium incorporation is currently quite low (i.e. [In] <5%) because of the different growth conditions for InN vs. GaN and AlN.

MBE is another commonly used growth technique in the III-nitrides. Elemental sources in the ultra-pure gas form are directed towards a heated substrate under ultra-high vacuum, typically in the range of 10^{-5}-10^{-11} Torr. The growth temperature off III nitrides is usually in the range of 800 - 850 ^{o}C. A higher growth temperature will result in lower growth rate because the forward and reverse reactions happen at the same time with different rates. Higher V/III ratio will prevent the dissociation of GaN. A low growth rate of less than 1μm/hr enables a layer-by-layer growth. Epilayers exihibit very abrupt interfaces. The ultra-high vacuum environment allows real-time monitoring of growth rate, film thickness, alloy composition, and atom reconstruction using in-situ reflection high-energy electron diffraction (RHEED).[16] The MBE growth of III-nitrides usually produces films with a N-polarity. There are some disadvantages of MBE growth of III-nitrides such as the requirement of ultra-high vacuum, a slower growth rate than MOVPE, and the difficulty to process multiple wafers. Because of these drawbacks, MBE is not widely used for commercial applications. However, MBE is very promising for the growth of high-indium-content InGaN films because of the lower growth temperature.

1.4. InGaN for Solar Cells

III-nitrides are widely used for solid-state lighting. Recently, the InGaN alloy system has attracted major attention for solar cell applications [17][18][19] because its bandgap energy falls in the range from 0.7 eV (InN) to 3.4 eV (GaN), covering most of the solar spectrum.[20][21][22] InGaN is a potential candidate for multiple junction tandem solar cell applications due to its tunable bandgap by varying indium

composition.[23] An InGaN p-i-n homojunction with [In] ~ 55% can obtain a maximum efficiency ~ 25.5% for one junction solar cell based on theoretical calculations.[24] A two junction $In_xGa_{1-x}N$ tandem solar cell with one bandgap tuned to 1.7 eV (x ~ 0.5) and the other one tuned to 1.1 eV (x ~ 0.75) could theoretically attain 50% efficiency. All the development of the next generation high efficiency InGaN-based solar cells requires increasing indium composition to absorb lower energy photons.

1.5. Challenges in Realization of High Quality InGaN Alloy

We have discussed the challenge of InGaN growth by MOVPE in section 1.3. The second challenge for InGaN alloy is the lattice mismatch. InGaN films are usually grown on GaN epilayers on sapphire substrates. InGaN alloys have the hexagonal wurtzite structure, with a chemical bond length ranging from 0.1951 to 0.2171 nm, for GaN and InN, respectively, corresponding to a difference of ~10.7%. Lattice mismatch strain relaxation in InGaN/GaN layers has been observed to occur in various ways. In *c*-plane epitaxy, misfit dislocations can be introduced by glide along the basal plane and along the $\{11\bar{2}2\}\langle 11\bar{2}3\rangle$ slip system,[26][27] by a punch-out mechanism involving slip on inclined prismatic planes,[28] and by bending of dislocations threading from the GaN underlayer.[29] The misfit strain relaxation will be discussed in chapter 2.

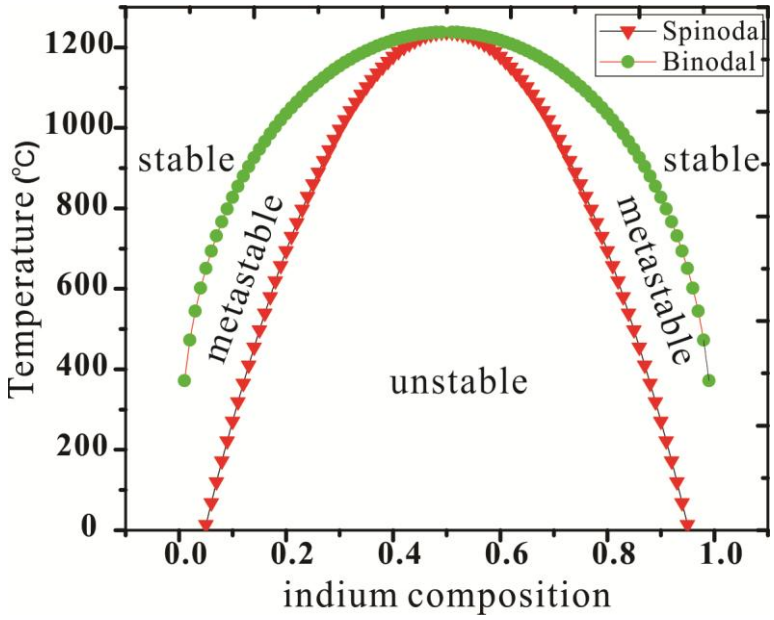

FIG. 1.5. Calculated phase diagram for binary alloys of GaN and InN, showing the binodal (green filled circles), spinodal (filled triangles) curves, and the critical temperature (~1250 ℃).[34] Stable, metastable, and unstable regions are shown.[30]

Another challenging issue for growth of InGaN is compositional instability.[30] The difference in interatomic spacing is said to lead to a solid phase miscibility gap as shown in Fig 1.5.[30] A systematic study of the microstructure evolution of $In_xGa_{1-x}N$ alloys grown using organometallic vapor phase epitaxy (OMVPE), in the temperature range from 700 to 900^{o}C, showed a variety of microstructures.[25] For $x < 0.08$, the indium content is uniform and unperturbed by threading dislocations. Secondary phases nucleating at threading dislocations are observed for $In_xGa_{1-x}N$ with $0.08 < x < 0.20$. Severe limitations in the synthesis reaction prevent proper epitaxial growth and result in inhomogeneous layers with possible phase separation in $In_xGa_{1-x}N$ with $x \geq 0.20$.

Due to these difficulties, MBE could be a suitable growth method for the high-indium-content InGaN growth because of the advantages of MBE growth discussed in the previous section. Recently, two modified MBE growth techniques known as Metal-modulated epitaxy (MME)[31] and Energetic nitrogen atom beam lithography and epitaxy (ENABLE)[32] were used to grow high quality InGaN films with no phase separation at very low temperatures <500^{o}C. We will study the structural properties of these InGaN films in detail in Chapter 4 and Chapter 5.

1.6. AlGaN for Deep Ultraviolet Laser

Deep ultraviolet (DUV) optoelectronic devices emitting below 280 nm are of great potential in the application of water purification, bio-agent detection, and medical sterilization.[33][34][35] GaN and AlN are wide gap semiconductors, having a direct bandgap ranging from 3.4 to 6.2 eV, respectively. Hence, UV emitters based on AlGaN alloys can successfully achieve wavelengths below 280nm.[36][37][38][39][40] However, the performance characteristics of typical AlGaN-based devices is limited by a low carrier concentration, a low injection efficiency, and a high concentration of crystalline defects. The performance is even worse for shorter wavelength emitters that require higher aluminum contents. This is also the case for DUV laser structures epitaxially grown on foreign substrates, which face the problem of a high density of defects. Lattice mismatch strain relaxation happens by the way of forming dislocations and cracks. These defects act as carrier traps that inhibit radiative recombination, thus lowering the output efficiency and increasing the power threshold for stimulated

emission.[41] These defects must be reduced or eliminated in high-aluminum-containing structures in order to achieve high-power operation and lasing in the DUV spectral range.

The availability of high quality AlN substrates provides a possible solution for this problem since they enable homoepitaxial growth of AlN buffer layers,[42] leading to a reduced threading dislocation density in the subsequent $Al_xGa_{1-x}N$ MQW active region. The elimination of thermal mismatch between the substrate and epitaxial layers also enhances epilayers' quality and performance of the device by eliminating cracks that form during the thermal cycle and cool-down. We will study the structural properties of AlGaN based DUV laser structures in Chapter 5.

1.7. Organization of this Dissertation

In this dissertation, the challenges encountered in the development of high quality high-indium-content InGaN film for solar cell application and high quality AlGaN-based DUV laser structure are addressed from a microscopic point of view.

In Chapter 2, fundamental concepts of lattice mismatch and misfit dislocation are introduced. The Matthews-Blakeslee's classical model and People's model of misfit dislocation mechanics are reviewed. Critical thickness calculations for InGaN /GaN heterostructures based on these models are suggested. Plastic relaxation via slip in cubic and hexagonal material systems is discussed.

In Chapter 3, experimental techniques for studying III-nitride materials are reviewed. Techniques including electron diffraction pattern, bright-field imaging, weak-beam dark field imaging, high-resolution imaging, Z-contrast imaging, energy dispersive X-ray, and sample preparation by wedge polishing are presented.

In Chapter 4, the microstructure of $In_xGa_{1-x}N$ (x = 0.22, 0.46, 0.60, and 0.67) films grown by metal-modulated epitaxy (MME) on GaN buffer on sapphire substrates is studied. The effect of indium composition on the structure of InGaN films and strain relaxation is carefully analyzed. High luminescence intensity, low defect density, and uniform full misfit strain relaxation are observed for x = 0.67. A critical thickness value of the order of a monolayer for efficient strain relaxation is proposed.

In Chapter 5, the microstructure of $In_xGa_{1-x}N$ (x = 0.48, 0.55, 0.60, 0.78, 0.84, and 1.00) grown by energetic nitrogen atom beam lithography and epitaxy (ENABLE) on an AlN buffer on sapphire substrates were studied. The effect of the AlN buffer layer on the misfit strain relaxation by misfit dislocation at interface is discussed.

In Chapter 6, the microstructure of AlGaN- based ultra-violet laser structures is studied. The effect of sapphire substrates and single crystal AlN substrates on the structural properties and optical properties are discussed. The effect of different trimethylgallium (TMG) sources during growth on the structure of MQWs is discussed.

In Chapter 7, the main findings of this dissertation are summarized and future work is suggested.

References

[1] F. A. Ponce and D. P. Bour, Nature (London) **386**, 351 (1997).

[2] D. Chandrasekhar, D. J. Smith, S. Strite, M. E. Lin, and H. Morkoc, J. Crystal Growth. **152**, 135 (1995).

[3] F. A. Ponce, in *Introduction to Nitride Semiconductor Blue Lasers and Light Emitting Diodes*, edited by S. Nakamura and S. F. Chichibu, Taylor and Francis Ltd, London, Chapter 4 (2000).

[4] L. Liu and J. H. Edgar, Materials Science and Engineering **R37**, 61 (2002).

[5] C. H. Hong, D. Pavlidis, S. W. Brown, and S. C. Rand, J. Appl. Phys. **77**, 1705 (1995).

[6] F. C. Frank, Acta Cryst. **18**, 862, 1965.

[7] I. Vurgaftman, J.R. Meyer, J. Appl. Phys. **94**, 3675 (2003).

[8] F. Bernardini, V. Fiorentini, D. Vanderbilt, Phys. Rev. B 56, R10024 (1997)

[9] A. M. Fischer, Ph.D. Dissertation, Arizona State University, 8-13 (2009).

[10] F. A. Ponce, D. P. Bour, W. T. Young, M. Saunders, and J. W. Steeds, Appl. Phys. Lett. **69**, 337 (1996).

[11] A. Kazimirov, G. Scherb, J. Zegenhagen, T. L. Lee, M. J. Bedzyk, M. K. Kelly, H. Angerer, and O. Ambacher, Appl. Phys. Lett. **84**, 1703 (1998).

[12] O. Ambacher, J. Phys. D: Appl. Phys. **31**, 2653 (1998).

[13] M. P. Maruska and J. J. Tietjen, Appl. Phys. Lett. **15**, 327 (1969).

[14] H. Amano, N. Sawaki, I. Akasaki, and Y. Toyoda, Appl. Phys. Lett. **48**, 353 (1986).

[15] O. Ambacher, M. S. Brandt, R. Dimitrov, T. Metzger, M. Stutzmann, R. A. Fischer, A. Miehr, A. Bergmaier, and G. Dollinger, J. Vac. Sci. Technol. B **14**, 3532 (1996).

[16] A. Y. Cho, Surf. Sci. **17**, 494 (1969).

[17] O. Jani, I. Ferguson, C. Honsberg, and S. Kurtz, Appl. Phys. Lett. **91**, 132117 (2007).

[18] C. J. Neufeld, N. G. Toledo, S. C. Cruz, M. Iza, S. P. DenBaars, and U. K. Mishra, Appl. Phys. Lett. **93**, 143502 (2008).

[19] R. Dahal, B. Pantha, J. Li, J. Y. Lin, and H. X. Jiang, Appl. Phys. Lett. **94**, 063505 (2009).

[20] V. Yu. Davydov, A. A. Klochikhin, R. P. Seisyan, V. V. Emtsev, S. V. Ivanov, F. Bechstedt, J. Furthmuller, H. Harima, A. V. Mudryi, J. Aderhold, O. Semchinova, and J. Garul, Phys. Status Solidi **B 229**, 1 (2002).

[21] J. Wu, W. Walukiewicz, K. M. Yu, J. W. Ager III, E. E. Haller, H. Lu, W. J. Schaff, Y. Saito, and Y. Nanishi, Appl. Phys. Lett. **80**, 3967 (2002).

[22] T. Matsuoka, H. Okamoto, M. Nakao, H. Harima, and E. Kurimoto, Appl. Phys. Lett. **81**, 1246 (2002).

[23] H. Hamzaoui, A. S. Bouazzi, and B. Rezig, Solar Energy Materials & Solar Cells **87**, 595 (2005).

[24] C. A. M. Fabien, M. Mosely, B. Gunning, W. A. Doolittle, A. M. Fischer, Y. O. Wei, and F. A. Ponce, IEEE Journal of Photovoltaics, **4**, 601 (2014).

[25] F. A. Ponce, S. Srinivasan, A. Bell, L. Geng, R. Liu, M. Stevens, J. Cai, H. Omiya, H. Marui, and S. Tanaka, Phys. Stat. Sol. A **240**, 273 (2003).

[26] S. Srinivasan, L. Geng, R. Liu, F.A. Ponce, Y. Narukawa, and S. Tanaka, Appl. Phys. Lett. **83**, 5187 (2003).

[27] R. Liu, J. Mei, S. Srinivasan, H. Omiya, F. A. Ponce, D. Cherns, Y. Narukawa, and T. Mukai, Jpn. J. Appl. Phys. **45**, L549 (2006).

[28] R. Liu, J. Mei, S. Srinivasan, H. Omiya, F. A. Ponce, D. Cherns, Y. Narukawa, and T. Mukai. Jpn. J. Appl. Phys. **45**, L549 (2006).

[29] Z. H. Wu, K. Nonaka, Y. Kawai, T. Asai, F. A. Ponce, C. Q. Chen, M. Iwaya, S. Kamiyama, H. Amano, and I. Akasaki, Appl. Phys. Express **3**, 111003 (2010).

[30] I. Ho and G. B. Stringfellow, Appl. Phys. Lett. **69**, 2701 (1996).

[31] M. Moseley, B. Gunning, J. Greenlee, J. Lowder, G. Namkoong, and W. A. Doolittle, J. Appl. Phys. **112**, 014909 (2012).

[32] T. L. Williamson, J. J. Williams, J. C. D. Hubbard, and M. A. Hoffbauer, J. Vac. Sci. Technol. B, **29**, 03C132 (2011).

[33] T. Cutler and J. Zimmerman, Anim. Health Res. Rev. **12**, 15 (2011).

[34] H. H. Chun, J. Y. Kim, and K. B. Song, Food Sci. Biotechnol. **19**, 547 (2010).

[35] K. Baxter, M. Castle, S. Barrington, P. Withers, V. Foot, A. Pickering, and N. Felton, Proc. Of SPIE **6739**, 67390Z (2007).

[36] J. R. Grandusky, S. R. Gibb, M. C. Mendrick, C. Moe, M. Wraback, and L. J. Schowalter, Appl. Phys. Express **4**, 082101 (2011).

[37] M. S. Shur and R. Gaska, IEEE Trans. Electron Devices **57**, 12 (2010).

[38] H. Hirayama, Y. Tsukada, T. Maeda, and N. Kamata, Appl. Phys. Express **3**, 031002 (2010).

[39] V. Adivarahan, A. Heidari, B. Zhang, Q. Fareed, S. Hwang, M. Islam, and A. Khan, Appl. Phys. Express **2**, 102101 (2009).

[40] A. Yasan, R. McClintock, K. Myes, D. Shiell, L. Gautero, S. Darvish, P. Kung, and M. Razeghi, Appl. Phys. Lett. **83**, 4701 (2003).

[41] J. Mickevičius, J. Jurkevičius, K. Kazlauskas, A. Žukauskas, G. Tamulaitis, M. S. Shur, M. Shatalov, J. Yang, and R. Gaska, Appl. Phys. Lett. **100**, 081902 (2012).

[42] A. Rice, R. Collazo, J. Tweedie, R. Dalmau, S. Mita, J. Xie, and Z. Sitar, J. Appl. Phys. **108**, 043510 (2010).

CHAPTER 2

LATTICE MISMATCH AND PLASTIC RELAXATION

Lattice mismatch and plastic relaxation play an important role in semiconductor heteroepitaxy. Strain resulting from the difference in lattice parameter can be beneficial as well as detrimental to the electronic properties. This chapter gives a brief introduction to the energetics of pseudomorphically strained thin films, critical thickness leading to plastic relaxation, and mechanisms of misfit dislocation generation and propagation.

2.1. Lattice Mismatch in Heteroepitaxial structures

III-nitride materials are usually heteroepitaxially grown on foreign substrate such as sapphire or SiC. Lattice mismatch is defined as the difference between the lattice constant of two crystals with different lattice planes. Lattice mismatch usually prevents growth of a defect-free epitaxial film. If a film grows coherently on a thick substrate, a uniform stress will build up due to lattice mismatch. The stress state of heteroepitaxial layers depends on whether the in-plane lattice space of the epitaxial film is larger or smaller than that of the substrate. Figure 2.1 illustrates two cases of strain: compressive ($a_f > a_s$) and tensile ($a_f < a_s$).

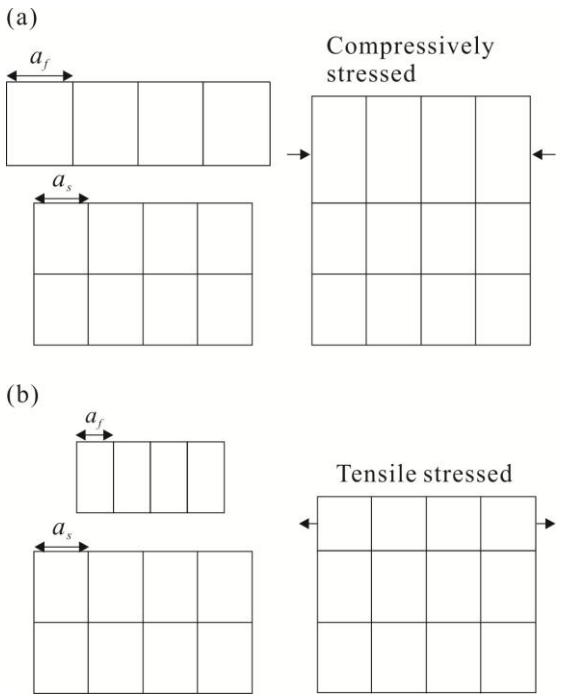

FIG. 2.1. Schematic diagrams showing (a) compressive strain state (when $a_s < a_f$) and (b) tensile strain (when $a_s > a_f$), where a_s and a_f are in-plane lattice constant for substrate and epitaxial film.

The stress in the epilayer for biaxial isotropic materials is given by: [1]

$$\sigma = 2G\frac{1+\nu}{1-\nu}\varepsilon \tag{2.1}$$

Where G is the shear modulus of the film, ν is the Poisson's ratio, ε is lattice mismatch strain, which equals $(a_f^o - a_s)/a_s$ with a_f^o and a_s the lattice parameters of the relaxed film and substrate. The stored energy per unit area of the film/substrate interface associated with the stress given by Eq. (2.1) is

$$E = 2G\frac{1+\nu}{1-\nu}\varepsilon^2 h \tag{2.2}$$

The strain energy is proportional to the film thickness. The stored energy increases as the epitaxial film thickness increases. It is believed that the film will be elastically strained on the substrate if thickness is less than a certain critical thickness (h_c). Such is called pseudomorphic film, which usually happens for a layer of single-crystal material on single-crystal substrate featuring slightly different chemical composition. When the film thickness is larger than the critical thickness, the stored energy is large enough to form dislocation and hence strain relaxation processes take place.[1]

2.2. Critical Thickness for the Formation of Misfit Dislocation

Generation of interfacial misfit dislocations (MD) with the help of slip system is a common way for plastic relaxation of misfit stress in heteroepitaxial structures.[2] The

slip system is constituted with a slip plane along with a slip direction. The slip plane is usually the plane with closest packing of atoms. The slip direction is usually the shortest lattice vector within the slip plane. The most common slip systems for FCC and hexagonal is {111} <011> and $\{0001\}< 11\bar{2}0 >$, respectively. For slip to occur, the shear stress resolved along a slip plane must exceed a particular value, which will be explained later by using critical thickness models. Figure 2.2 illustrates a geometric consideration when calculating resolved shear modulus τ_R:

$$\tau_R = \sigma cos\phi cos\lambda \tag{2.3}$$

Where ϕ is the angle between the stress direction and the normal to the slip plane, λ is the angle between the slip direction and stress direction. For stress parallel and perpendicular to the slip plane, $\tau_R = 0$.

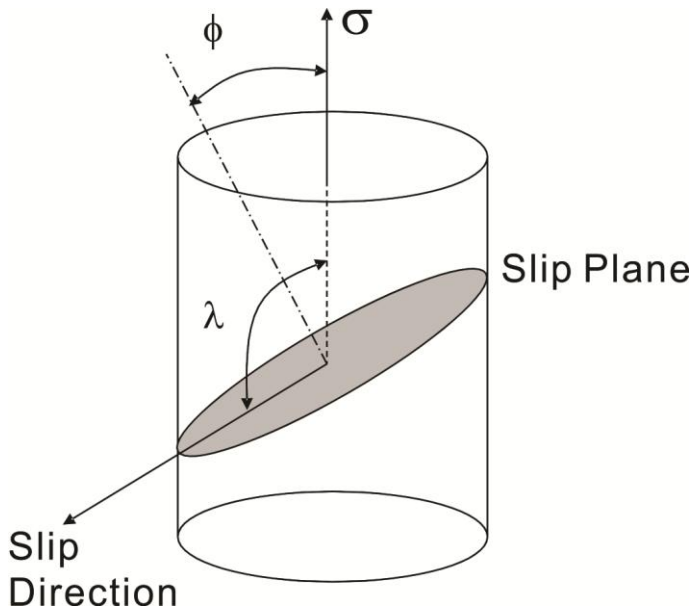

FIG. 2.2. Schematic diagram showing the geometry of the slip system in a heteropeitaxial structure.

Several models have been used to estimate the critical thickness in heteroepitaxial systems.[2,3] The force balance model by Matthews and Blakeslee has been applied extensively to lattice-mismatched systems.[2] This model considers two forces acting on an existing dislocation – the first is the force exerted by the misfit strain (applied force: F_a) and the second is the force due to the dislocation line tension F_l. The first one is given by:

$$F_a = 2Gbh\varepsilon\frac{1+v}{1-v}cos\lambda \tag{2.4}$$

where G is the shear modulus of the film, b is the magnitude of the Burgers vector of the dislocation, h is the film thickness, v is the Poisson's ratio, λ is the angle between the slip direction and the direction in the film plane which is perpendicular to the line $\boldsymbol{u}$ of intersection of the slip plane and the interface, ε is the lattice mismatch strain which equals $(a_f\text{-}a_s)/a_s$ where a_s and a_f are the lattice parameters of the substrate and the film, respectively. The geometry that we are considering is sketched in Fig. 2.3. The second force is the line tension (F_l), which resists the motion of the dislocation:

$$F_l = \frac{Gb^2}{4\pi}\frac{1-vcos^2\alpha}{1-v}\left[ln\left(\frac{h}{b}\right)+1\right] \tag{5}$$

where α is the angle between the misfit dislocation line and its Burgers vector.

The model assumes that there are pre-existing threading dislocations from the substrate which can elongate to form the misfit dislocations in the epilayer. The model then assumes that a critical thickness occurs when the force exerted by the misfit strain (which elongates the threading dislocation) matches the tension force (which opposes the elongation) of a pre-existing line dislocation. When a layer thickness is greater than the critical thickness, the force of the misfit strain exceeds that of the line tension, the

existing dislocation glides to the epilayer/substrate interface producing a segment that lies at the interface plane, *i.e.* a misfit dislocation that relieves the misfit strain. The Matthews-Blakeslee critical thickness thus obtained is:

$$h_c = \frac{b}{8\pi\varepsilon}\frac{(1-\nu cos^2\alpha)}{(1+\nu)cos\lambda}\left(ln\frac{h_c}{b}+1\right) \tag{2.6}$$

The Peierls' force (F_p) is a frictional component that resists dislocation motion and should be taken into consideration for the case of misfit dislocation generation. The following expression has been proposed:[4, 5]

$$F_p = 2Gbhsec\phi\,\frac{1-\nu cos^2\alpha}{1-\nu}\,\omega exp\left(\frac{-2\pi d(1-\nu cos^2\alpha)\omega}{(1-\nu)b}\right) \tag{2.7}$$

where ϕ is the angle between the film surface and the normal to the slip plane, d is the interplanar spacing corresponding to the slip plane. In addition, ω is a material constant given by $\omega = exp(4\pi^2 nkT/5GV)$, where n is the number of atoms per unit cell, V is the volume of the unit cell, and T is the growth temperature. At the critical thickness h_c, the three forces: F_a, F_l, and F_p should satisfy $F_a = F_l + F_p$. When the film thickness is larger than h_c, the force due to misfit strain is larger than the opposing forces and misfit dislocations are generated.

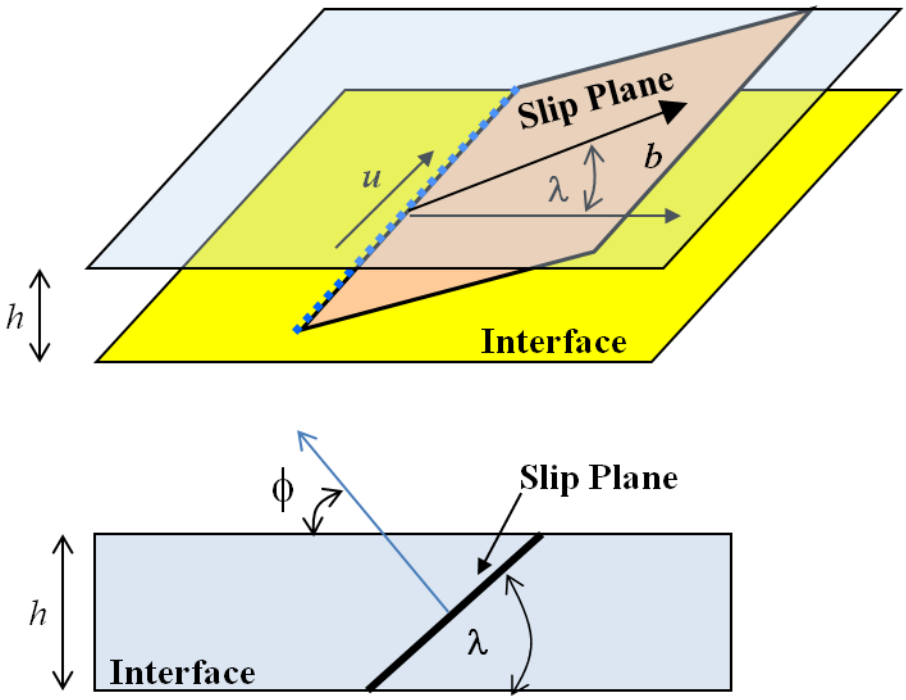

FIG. 2.3. Schematic diagram illustrating geometric consideration for strain relaxation via glide of dislocations along slip planes in heteroepitaxy.

People and Bean proposed another model based on energy balance,[3] taking into account the areal strain energy density E_h associated with a film with thickness h,

$$E_h = 2G\frac{1+v}{1-v}h\varepsilon^2 \tag{2.8}$$

The areal energy density associated with an isolated screw dislocation at a distance h from a free surface is approximately

$$E_d = \frac{Gb}{8\pi\sqrt{2}}ln\left(\frac{h}{b}\right) \tag{2.9}$$

In the model, the critical thickness due to lattice mistmatch is estimated for a film grown on a substrate that is initially free of dislocations. Screw dislocations were used instead of edge dislocation because of their lower strain energy. Misfit dislocations are generated

when E_h exceeds the energy density associated with the formation of a screw dislocation at a distance from the free surface equal to the film thickness *h*.

2.3. Plastic Relaxation in Cubic Material System

In cubic system, the slip system is <110>{111}. When a film thickness greater than a critical value, the plastice relaxation occurs via the <110>{111} slip system. There are two main sources for the generation of misfit dislocation in cuibic systems.[2] One is through gliding of pre-existing threading dislocaiton. For layer thickness greater than the critical thickness the existing dislocation bows and elongates under the influence of misfit stress resuting a misfit dislocation line at the interface. In this consideration, it assumes that substrate has high density of threading dislocation.

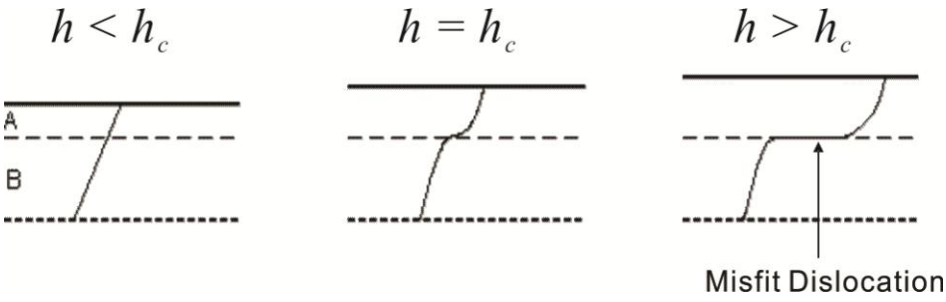

FIG. 2.4. A segement of misfit dislocation is generated with the help of pre-existing threading dislocaiton bending to the film/substrate interface when film thickness h > hc.[2]

The other one is considering of a substate of high quality and small threading dislocation densitiy. Generation of misfit dislocation is via nucleation of new dislocation half-loops at the growth surface. It involves dislocation epanding and gliding of grow-in

dislocation half loops. The generation of misfit dislocation will only happen until the film thickness if reach a critical thickness value so that it is energetically stable for the film to contain a half loop under the misfit strain.

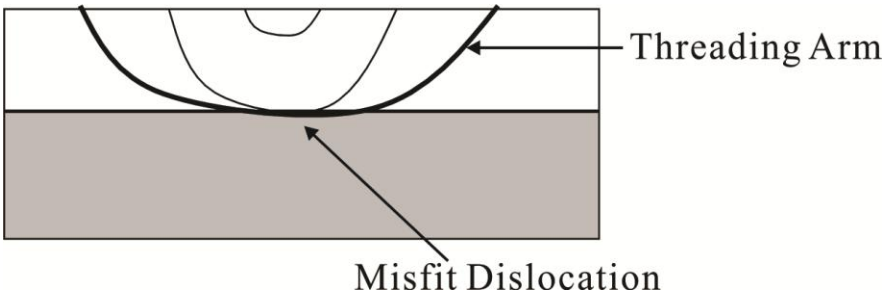

FIG. 2.5. A dislocation half loop nucleates at the growth surface and glides down along the {111} slip planes to form a segment of misfit dislocation along with two threading arm.[2]

2.4. Plastic Relaxation in Hexagonal Material System

As we mentioned before, the main slip system is the basal $\{0001\}<11\bar{2}0>$ system because {0001} are the close packed planes. The $<11\bar{2}0>$ slip direction corresponds to the shortest possible dislocation burgers vector $\frac{1}{3}<11\bar{2}0>$ for hexagonal lattice. However, the misfit dislocation generation via the main slip system $\{0001\}<11\bar{2}0>$ cannot happen, since resolved shear modulus on the basal plane is zero. In order to generate misfit dislocations at interface, a secondary slip system must be considered. Fig 2.4 shows all slip systems for wurtzite (hcp) structure. Misfit dislocation via prismatic slip secondary slips systems are reported for InGaN/GaN system. Srinivasan *et al*. did a complete study on the possible slip systems and reported that misfit dislocation

along the $< 1\bar{1}00 >$ are generated the $In_xGa_{1-x}N/GaN$ (x = 0.1) interface by the help of a secondary slip system$< 11\bar{2}3 >$ $\{11\bar{2}2\}$.[4] Rong *et al.* reported that misfit dislocations along $< 10\bar{1}0 >$ directions with a Burgers vector $\boldsymbol{b}$ = (2/3) $< 11\bar{2}0 >$ and he proposed that the dislocations were introduced by a punch-out mechanism involving slip on inclined prismatic planes.[6]

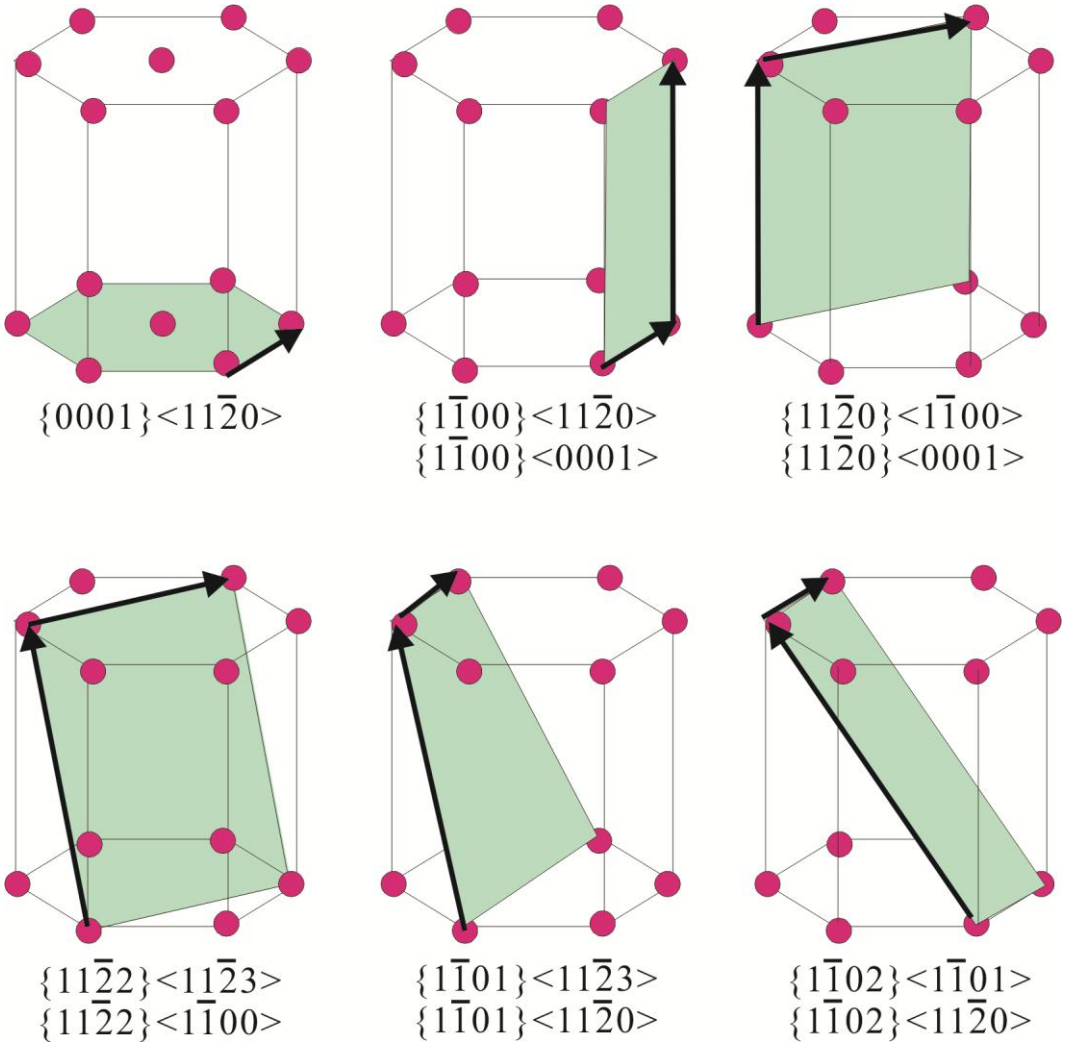

FIG. 2.6. Hexagonal slip systems. Slip plane and slip directions are indicated.[4]

It should be noted that generation of misfit dislocations at $In_xGa_{1-x}N$/GaN interface via secondary slip systems were reported for $x < 0.2$. Calculated critical thickness for generation of dislocation is relatively high when indium composition is low. The major contribution of the work present in this thesis is to study the misfit-strain relaxation process for $In_xGa_{1-x}N$ with high indium composition ($x > 0.2$). Fully lattice mismatch relaxation at interface by misfit dislocations has been observed for $x > 0.6$, and are discussed in some length in chapter 4 and 5.

References

[1] A. M. Andrews, J. S. Speck, A. E. Romanov, M. Bobeth, and W. Pompe, J. Appl. Phys **91**, 1933 (2002).

[2] J. W. Matthews and A. E. Blakeslee, J. Cryst. Growth **27**, 118 (1974).

[3] R. People and J. C. Bean, Appl. Phys. Lett. **47**, 322 (1985).

[4] S. Srinivasan, A. Bell, L. Geng, R. Liu, M. Stevens, J. Cai, H. Omiya, H. Marui, and S. Tanaka, Phys. Stat. Sol. A **240**, 273 (2003).

[5] D. Chidambarrao, G. R. Srinivasan, B. Cunningham, and C. S. Murthy, Appl. Phys. Lett. **57**, 1001 (1990).

[6] R. Liu, J. Mei, S. Srinivasan, H. Omiya, F. A. Ponce, D. Cherns, Y. Narukawa, and T. Mukai. Jpn. J. Appl. Phys. **45**, L549 (2006).

CHAPTER 3

EXPERIMENTAL TECHNIQUES

Transmission electron microscopy (TEM) is a very useful tool for analyzing microstructures of III-N thin films and nanostructures. This chapter presents an overview of several TEM techniques including electron diffraction, diffraction contrast images, high-resolution electron microscopy, and scanning transmission electron microscopy.

3.1. Electron Diffraction Pattern

Electron diffraction is heavily used to study the crystal structure of solids. In a transmission electron microscope, the scattered electrons produced after a parallel electron beam passes through a sample, are converged to single points at the back focal plane by the objective lens. Those points at the back focal plane form a diffraction pattern. In my research, diffraction pattern are mostly used for (a) phase identification, crystal orientation determination and structural analysis; (b) setup diffraction contrast imaging; and (c) to orient crystals for high-resolution electron imaging.

In the kinematical approximation for electron diffraction, the intensity of the diffracted beam is expressed as

$$I_g = |\psi_g|^2 \propto |F_g|^2 \tag{3.1}$$

where ψ_g is the wave function of the diffracted beam and F_g is the structure factor. The general form for structure factor is given by

$$F_g = \sum_i f_i e^{2\pi i \boldsymbol{g}\cdot\boldsymbol{r_i}} \tag{3.2}$$

Where f_i is the atomic factor of atom, $\boldsymbol{g}$ is the scattering vector for the diffracted beam, and $\boldsymbol{r_i}$ is the position of an atom in the unit cell. Let us take GaN as an example; the structure factor for a wurtzite GaN unit cell for a generalized *(hkml)* diffraction point can be expressed as:

$$F_{hkml} = \left(f_{Ga} + f_N e^{2\pi i u l}\right)\left(1 + e^{2\pi i\left(\frac{h+2k}{3}+\frac{l}{2}\right)}\right) \tag{3.3}$$

Where f_{Ga} and f_N are the atomic scattering factor of Ga and N, respectively. u is the internal parameter for a wurtzite structure and it equals to 3/8 = 0.375. Theoretically, if $h + 2k = 3n$ and l is odd, the corresponding diffraction spot is invisible in the diffraction

pattern for wurtzite III-nitride. Figure 3.1 is a diffraction pattern along the $[1\bar{1}00]$ zone axis. Based on Eq. (3.3), the (0001) diffraction spot is forbidden under kinematical conditions.

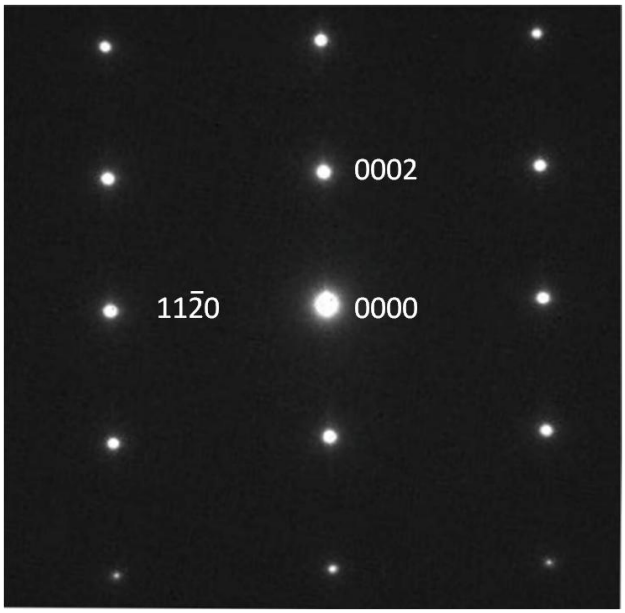

FIG. 3.1. Electron diffraction pattern of GaN along $[1\bar{1}00]$ zone axis. The (0001) diffraction spot is invisible.

However, if we tilt the sample along the (0001) plane, 30 degrees away from $[1\bar{1}00]$ zone axis, we get to the $[11\bar{2}0]$ zone axis, as shown in Fig. 3.2. In this case, the (0001) diffraction spot is dynamically excited due to double diffraction from allowed $(1\bar{1}00)$ and $(1\bar{1}00)$ planes and a weak spot is observed. We cannot see the (0001) diffraction spot under $[1\bar{1}00]$ zone axis because it cannot be acquired by superposition of the allowed diffraction at this zone.

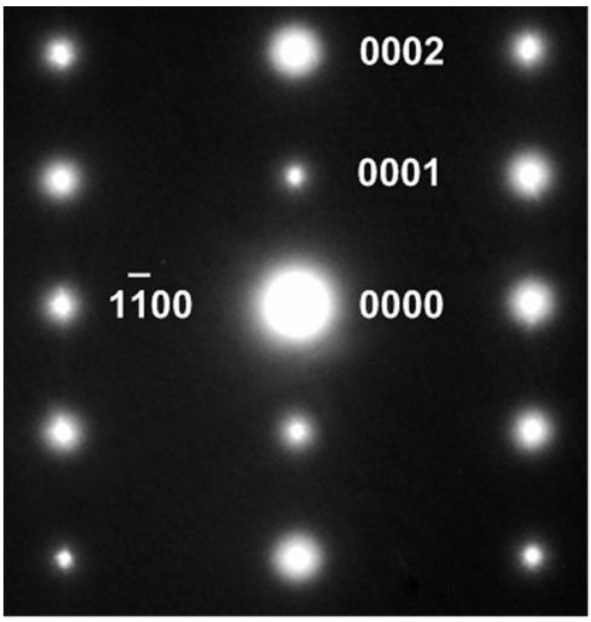

FIG. 3.2. Diffraction patterns of GaN along $[11\bar{2}0]$ zone axis. The (0001) diffraction spot is weaker than the (0002) diffraction spots. This can be understood as the result of double diffraction.

3.2. Diffraction-Contrast Imaging

Based on the diffraction conditions, diffraction-contrast imaging is extensively applied to study the properties of defects in the III-nitride materials. The density of the diffracted beam depends on the deviation parameter, *s*, and the displacement vector Δr . So, the diffraction contrast in the vicinity of defects will depend on the strain field caused by the defect. Generally, the amplitude of a diffracted wave can be expressed as:

$$\psi_g \propto \sum_r f(r) e^{2\pi i \Delta k r} = \sum_r f(r) e^{2\pi i (g-s)(R+\Delta r)} \approx \sum_r f(r) e^{2\pi i (g\Delta \mathrm{r} - \mathrm{sR})} \quad (3.4)$$

By comparing a region with the presence of a defect and a defect-free region, a phase difference of $g \cdot \Delta r$ can be found, whose difference determines the image contrast at the defect. The defect is out of contrast when $g \cdot \Delta r = 0$. Edge-type dislocation, screw-type

dislocations, mixed-type dislocations, basal plane stacking faults and grain boundaries are the most common crystal defects in III nitride thin films. Table 3.1 lists the displacement vectors for dislocations and stacking faults in GaN, and their visibility criteria:

Table 3.1. Typical defects in the III-Nitrides.

Defect type	Displacement vector (Burger's vector)	Visible under $g = 11\bar{2}0$	Visible under $g = 1\bar{1}00$	Visible under $g = 0002$
Edge dislocation	$\frac{1}{3}[11\bar{2}0]$	Yes	No	No
Screw dislocation	$[0001]$	No	No	Yes
Mixed dislocation	$\frac{1}{3}[11\bar{2}3]$	Yes	No	Yes
I_1 BSF	$\frac{1}{6}[2\bar{2}03]$	No	Yes	No
I_2 BSF	$\frac{1}{3}[1\bar{1}00]$	No	Yes	No
E BSF	$\frac{1}{2}[0001]$	No	No	No

In practice, we prepare thin TEM specimens in both $< 1\bar{1}00 >$ and $< 11\bar{2}0 >$ projections. For threading dislocation analysis, we use the former projection and we tilt the sample to excite the $g = 11\bar{2}0$ and $g = 0002$ beams. Then we take bright-field (BF) or weak-beam dark-field (WBDF) images. To study basal plane stacking faults (BSF), we use the $< 11\bar{2}0 >$ projection and excite the $g = 1\bar{1}00$ diffraction spot.

Bright-field imaging and weak-beam dark-field imaging were extensively used for defect analysis in my research. In order to get a good BF contrast of the dislocation, the specimen is tilted close to Bragg condition while keeping the deviation parameter *s* slightly positive. Those planes near the dislocation core are curved to $s = 0$ which result in strong Bragg reflection. We use a small objective aperture to select the desired transmitted (diffracted) beam. As a result, the BF image shows a dark line, representing the dislocation, on a bright background. The drawback of a BF image is that the contrast is not strong, causing the dislocations to look broad and diffused. The location of the core of the dislocation is clearly determined in this way. In order to get better contrast of dislocation, we can tilt the sample away from Bragg condition, so that only regions very near the dislocation core fulfill $s = 0$. This diffraction contrast technique is known as weak-beam dark-field (WBDF) contrast. Dislocations appear as sharp bright lines on a dark background. The line with the strongest Bragg reflection is very close to the position of dislocation core. Fig. 3.3 shows the comparison of BF and DF image. Dislocation lines appear diffuse and broad in the BF image, but narrow and sharp in the WBDF image.

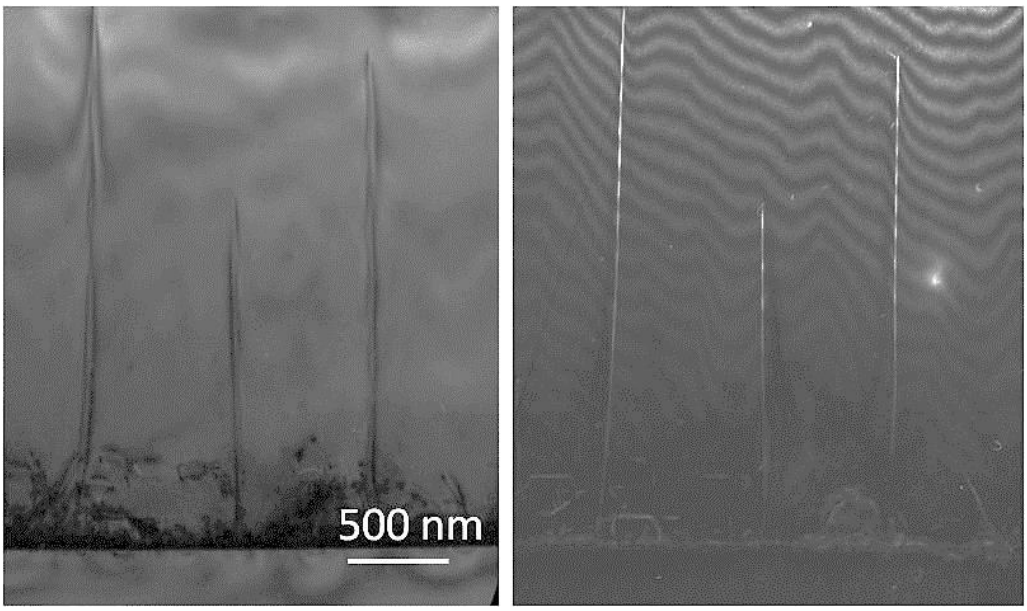

FIG. 3.3. Bright-field image (left) and dark-field image of GaN at the same region.

In the WBDF imaging case, we set a two-beam condition with *s* slightly greater than zero, as illustrated in Fig. 3.4. Beam deflection coils are used to tilt the beam to excite a strong ***g***, setting it on the optical axis. Under these conditions, the intensity of the *g* diffraction spot becomes weak whereas the 3*g* diffraction spot becomes strong. At last, insert the objective aperture and center it to choose the spot at optical axis. Now BF and *g*/3*g* WBDF are both well established. The Kikuchi band is fixed to the specimen so that it can be taken as a reference for checking *g*/3*g* condition.

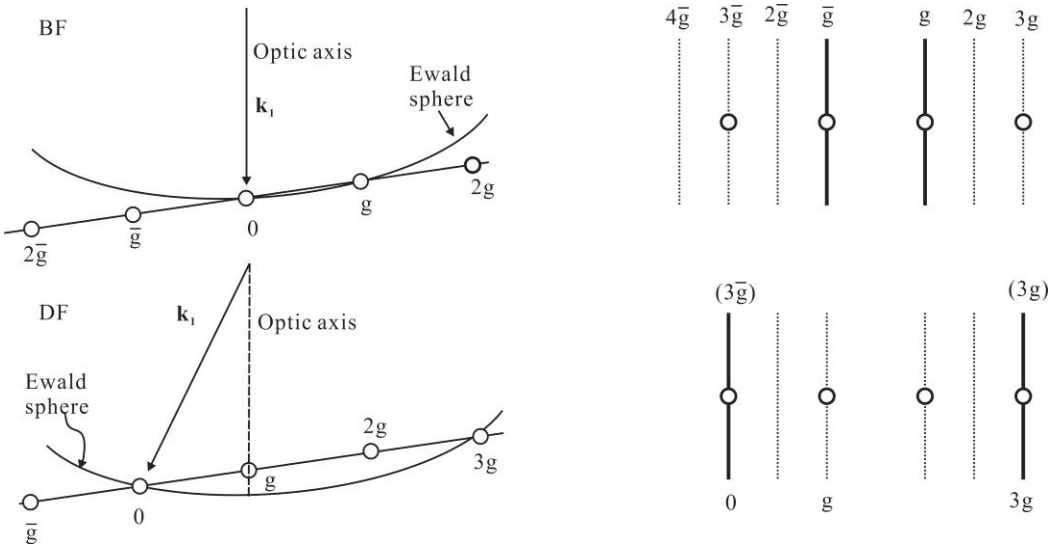

FIG. 3.4. Comparison of BF image and g/3g dark-field image.

3.3. High-Resolution TEM

High-resolution TEM offers visualization of the crystal structure at the atomic scale. Point resolution is considered to be one of the most important characteristics of a TEM. Resolution of a TEM is mostly limited by the characteristic of objective lens. When a virtually parallel planar electron wave passes through the thin specimen, the electron wave is scattered by the atomic potential. The wave at the exit surface of the specimen is considered to be the object wave in the microscope which carries the direct information of the object. The index of refraction of the specimen delays the electron wave with respect to a wave unperturbed in vacuum. This delay is represented by a phase change. The phase of the wave undergoes undesired shifts due to the spherical aberration and defocus of the object lens when it passes through the image path of the electron microscope. The image is recorded as the interference pattern of the image wave.

The image wave and object wave are nonlinear because of the imperfection of the objective lens. The interference pattern can be described by the contrast transfer function:

$$CTF(\boldsymbol{u}) = A(\boldsymbol{u})E(\boldsymbol{u})\sin(\chi(\boldsymbol{u})) \tag{2.3}$$

where $\boldsymbol{u}$ is the spatial frequency, $A(\boldsymbol{u})$ is the aperture function, $E(\boldsymbol{u})$ is the envelope function, $\chi(\boldsymbol{u})$ is a function related to the spherical aberration of the image system. In order to get the correct HRTEM image to describe the crystal structure, HRTEM images are usually recorded under various defocus values – since the contrast depends on the defocus value – and compared with computationally simulated images.

For wurtzite III-nitrides, the TEM specimen prepared for $[11\bar{2}0]$ zone axis imaging is better for high-resolution TEM images for two reasons. First, as shown in Fig. 3.5, the AB stacking sequence of the wurtzite structure is easily recognized. Second, the lateral lattice spacing is larger than the one under $[1\bar{1}00]$ zone axis. Figure 3.6 is a HRTEM taken along $[11\bar{2}0]$ zone axis on JEOL 4000EX. The AB stacking sequence matches the model in Fig. 3.5.

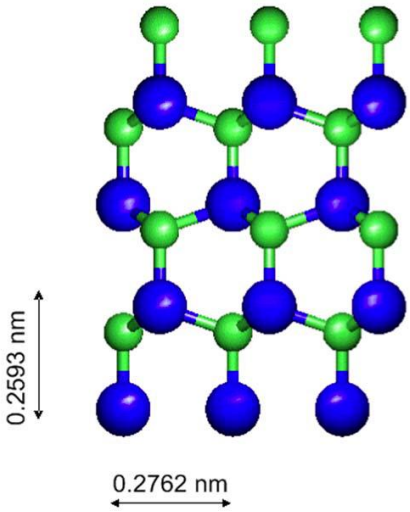

FIG. 3.5. Atomic configuration of GaN along $[11\bar{2}0]$ zone axis. Larger blue spheres represents Gallium and smaller green spheres represent N.

FIG. 3.6. High-resolution TEM images of GaN along $[11\bar{2}0]$ zone axis.

3.4. Scanning Transmission Electron Microscopy

Scanning transmission electron microscope (STEM) is a type of instrument that can be operated in a scanning mode. In this mode, the image-forming portion contains a

set of condenser lenses and an objective lens that focus the electron beam into a dimension of the order of an angstrom on the thin specimen. An objective aperture limits the maximum angle of illumination included in the incident probe, which is scanned across the sample by a set of scan coils. When the beam passes through the thin specimen, it is scattered in all directions, so a variety of detectors can be used to form images. The transmitted electrons with a small scattering angle (<10 mrad) with respect to the optical axis are collected to form STEM bright-field images which are comparable to TEM BF images. Electrons scattered at angles of the order of 10~50 mrad are detected by a annular dark-field (ADF) detector to form medium angular annular dark-field images (MAADF). One application of MAADF is to produce strain contrast in the image. Incoherent electrons scattered at high angles (>90 mrad) are used to form high angular annular dark-field images (HAADF). HADDF is also called z-contrast imaging, as first developed by Crewe and colleagues [1]. The integrated high-angle elastic signal depends strongly on the atomic number Z. The contrast from single atom goes as Z^n, where n is a number in between 1.6 and 1.9 depending on the inner and outer collected angle [2]. Z-contrast imaging is considered to be one of the most important techniques in STEM mode. Recently, more attention is being given to STEM BF images due to the availability of aberration-corrected STEM. The diffraction pattern shows higher density in the central region (0 ~ 11 mrad) for light elements and heavy elements shows higher density in the peripheral region (11~22 mrad). A line-up beam stopper is intentionally inserted to block the central region of transmitted beam, the contrast the light element is greatly enhanced in the annular bright-field images. Even hydrogen, the lightest element in the periodic

table, can be observed in annular bright-field (ABF) images.[3] Fig 3.7 shows a configuration of detectors for ADF and ABF imaging in a TEM (JEM-ARM200F).[4]

Energy-dispersive X-ray spectroscopy is an analytical technique, which uses the characteristic X-rays due to the electronic excitation in the sample. This technique can be used to provide chemical information and elemental distribution of the sample. Another useful analytical technique, which makes use of slightly deflected inelastically scattered electrons, is called electron energy loss spectroscopy (EELS). [5,6] This technique is used to extract further information about local variations of composition. Bandgap measurement is an advanced characterization option when using EELS. Bandgap values lie between the zero loss peak and the plasmon peak. This region can be resolved with the help of a monochromator-equipped STEM.

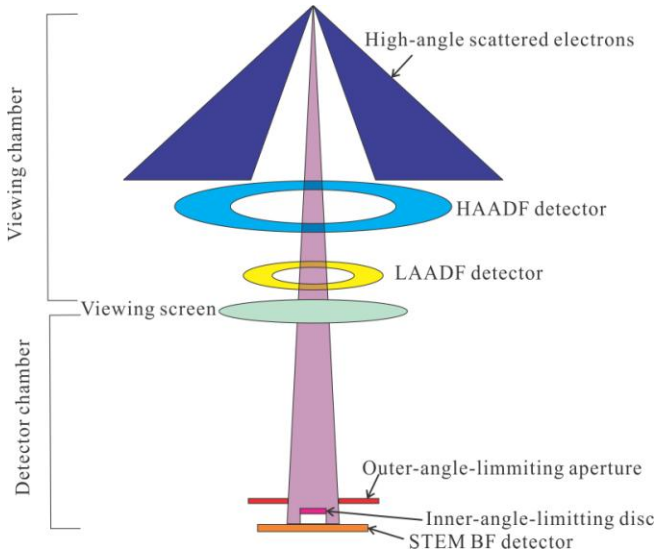

FIG. 3.7. Configuration of detectors for ADF and ABF imaging in a TEM (JEM-ARM200F).[4]

3.5. TEM Sample Preparation

A cross-sectional TEM specimen with a large thin clean area is the prerequisite for optimal TEM imaging of defects and interfaces in thin films. The standard procedure to polish sapphire substrate samples is shown in Fig. 2.8. Next, we will show how an InGaN/sapphire structure is typically prepared for cross-section TEM.

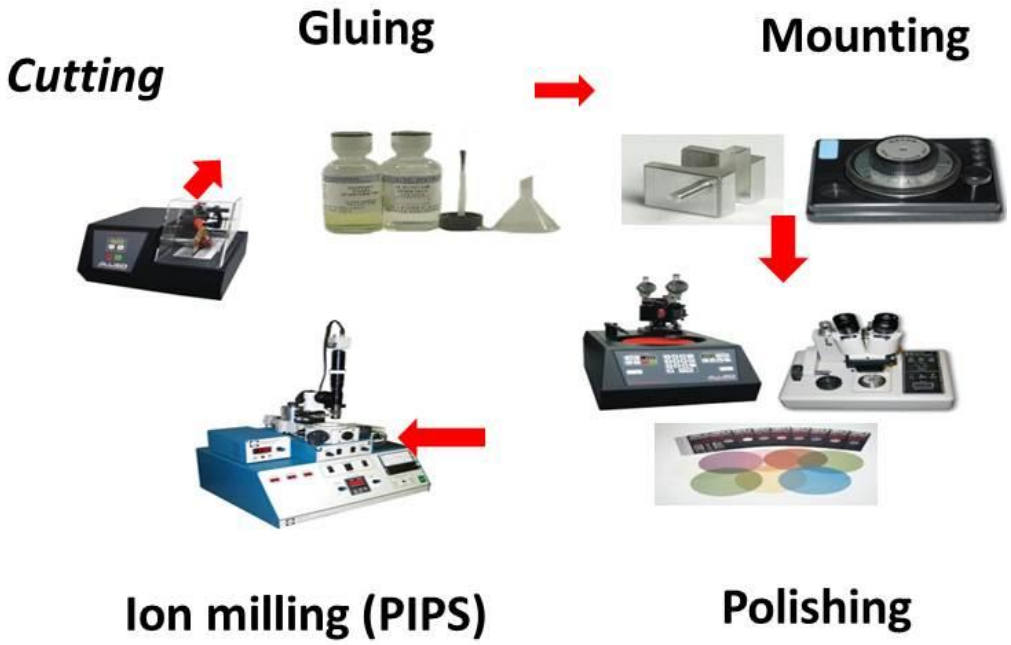

FIG. 3.8. TEM cross-section sample preparation procedures.

3.5.1. Sectioning

A piece of InGaN film grown on sapphire wafer is glued to a glass slide using crystal wax on a hot plate at 160 ℃. A diamond saw is used to cut the sample into 3mm x 1.5mm rectangular pieces. The samples are cleaved into 3mm-strips and then cut into small pieces with a width of ~ 1.5 mm. These samples are then heated in the hot plate and

removed, followed by an acetone bath for 5 min, and finally cleaned with ethanol for an extra 5 min.

Two identical pieces are glued together using M-bond with the film layer surface facing each other. The samples are gently pressed together using a special specimen clamp to remove the excess glue. Finally, the clamped samples are cured at a temperature of 90 ^{o}C for about one hour.

3.5.2. First Side Polishing

After curation, the glued samples are polished using an Allied Multiprep polishing system. First, the samples are mounted with the sides of the InGaN film and sapphire substrate on the glass stub using the CrystalBond wax. Diamond lapping films with different mesh are used to remove approximately 5 μm of material. Table 3.2 gives some polishing details. The first side polish is only finished when all visible scratches and gouges of glue are removed, as this side will be used for TEM viewing. If there are any scratches in or around the thin film region of interest after using 0.5 μm lapping film, the polishing steps with 1 to 0.5 μm lapping film should be repeated. After polishing, the sample is removed from the stub, both sample and glass stub are cleaned in acetone and ethanol. Then the sample is flipped over and thinned down to about 100 μm using 30 μm lapping film.

3.5.3. Second Side Polishing

A two-degree tilt is introduced in the subsequent polishing steps to polish a wedge-shaped specimen. The specimen is thinned down to a thickness less than 1 μm,

when fringes with multiple colors are observed in the thinnest portion of the sample. The specimen is then glued on a copper grid and cured at 90 ^{o}C for about one hour. Then, the sample is placed on a beaker with acetone to dissolve the wax until the sample detaches form the glass stub. The sample is finally argon-ion-milled in a Gatan Model 691 PIPS system. The sample is mounted in a 'duopost' stage and milled using a 3.5 kV ion beam at an angle of ~ 7 deg at liquid nitrogen temperatures. Low energy ion milling at 2.0 keV are used for minimizing the formation of interfacial layers or any amorphous surface. A 20-min plasma cleaning is always helpful to remove amorphous layers on the film surface due to oxidation or backsputtered material during ion milling.

Table 3.2. Detail setup of Allied MultiPrep polishing system at each thickness of diamond lapping film for polishing the first side of InGaN/GaN/ sapphire samples.

Polish grade (μm)	Platen speed (rpm)	Material removed (≈ μm)
30	100	350
9	90	100
6	80	50
3	70	20
1	60	5
0.5	50	2

Table 3.3. Detail setup of Allied MultiPrep polishing system at each thickness of diamond lapping film for polishing the second side of InGaN/GaN/ sapphire samples.

Polish grade (μm)	Platen speed (rpm)	Thickness of the sample after polishing (μm)
30	100	90~120
9	90	50
6	80	15~20
3	70	5
1	60	~1
0.5	50	<1

References

[1] A. V. Crewe, and J. Wall, J. Mol. Biol. **48**, 375 (1970).

[2] P. Hartel, H. Rose, and C. Dinges, Ultramicroscopy **63**, 93 (1996).

[3] R. Ishikawa, E. Okunishi, H. Sawada, Y. Kondo, F. Hosokawa, and E. Abe, Nature Matierials **10**, 278 (2011).

[4] E. Okunishi, H. Sawada, and Y. Kondo, Micron **43**, 538-544 (2012).

[5] D. B. Williams, and C. B. Carter, Transmission Electron Microscopy, (Springer, 1996), chapter 38, p. 655-663.

[6] P. D. Nellist, Scanning Transmission Electron Microscopy: Imaging and Analysis, (Chapter 2, Springer, 2011), chapter 2, p. 91-116.

CHAPTER 4

MICROSTRUCTURE OF $In_xGa_{1-x}N$ (x = 0.22 - 0.67) FILMS GROWN BY METAL-MODULATED EPITAXY

This chapter presents the microstructure evolution of $In_xGa_{1-x}N$ films with indium composition x in the range from 0.22 to 0.67. The films were grown by metal-modulated epitaxy at low temperatures (~ 400 ℃) to facilitate indium incorporation, and with precursor modulation to enhance surface morphology and metal adlayer diffusion. A high density of crystalline defects consisting mainly of stacking faults associated with island growth is observed in the lower composition range x = 0.22. The microstructure evolves into fine columnar domains devoid of stacking faults in the middle range (x = 0.46). A significant improvement in the crystalline quality and optical properties is observed for $x \geq 0.60$, with strain relaxation at the interface evidenced by the presence of moiré fringes. High luminescence intensity, low defect density, and near-complete uniform misfit strain relaxation are observed for x = 0.67. The strain relaxation can be explained by a critical thickness value of the order of a monolayer. This behavior is reproducible in variations of the growth technique, and provides an approach for growth under high lattice mismatch conditions.*

(*) Portions of his chapter have been published as:

A. M. Fischer, Y. O. Wei, F. A. Ponce, M. Moseley, B. Gunning, and W. A. Doolittle. *Highly luminescent, high-indium-content InGaN film with uniform composition and full lattice mismatch relaxation.* Appl. Phys. Lett. **103**, 131101 (2013).

4.1. Introduction

InGaN alloys are important for optoelectronic devices primarily due to their direct energy band gap ranging from the near IR to the ultraviolet, covering most of the solar spectrum.[1] InGaN films have been extensively investigated for applications in high efficiency emitters, high temperature electronics, and high frequency devices. InGaN alloys with high indium content, low dislocation densities, and spatially uniform composition are desirable for applications such as light emitting devices operating in the green and longer wavelength regime, and for high efficiency photovoltaic solar cells.[2][3][4] However, it is challenging to grow high quality InGaN films with high indium composition. The challenges encountered in the realization of high quality InGaN are discussed in Chapter 1.

Moseley *et al.* recently reported high quality single-phase $In_xGa_{1-x}N$ films for a wide range of indium compositions grown using a layer-by-layer approach at low temperatures by the metal modulated epitaxy (MME) technique.[6] Fischer *et al.* found that the high indium content epilayers (x = 0.67) exhibit misfit strain relaxation at the InGaN/GaN interface, and a significant improvement of structural and optical properties.[7]

We report here on the evolution of the microstructure for $In_xGa_{1-x}N$ epilayers grown by the MME growth technique, for x values of 0.22, 0.46, 0.60, and 0.67. $In_xGa_{1-x}N$ epilayers show high density of defects for x = 0.22 and 0.46. A surprising improvement of the microstructure is observed for x ~ 0.60 and above. High luminescence, uniform indium composition, and near-complete misfit-strain relaxation is observed in $In_xGa_{1-x}N$ films with x = 0.67.

4.2. Experimental Techniques

4.2.1. Growth

The $In_xGa_{1-x}N$ films with indium composition in the range [0.2, 0.7] were grown by the MME technique,[8] on GaN epilayers on *c*-sapphire substrates, at temperatures ranging from 400 to 450 ℃ in a Riber 32 MBE system, with metal rich fluxes, and a group-III, Z-number ponderated (Ga-flux/31 + In-flux/49) beam equivalent pressure between 0.24 and 0.30×10^{-7} Torr. Due to the low substrate temperature and resulting reduction of desorption, the final In composition is simply the ratio of the Z-number normalized In flux to the total metal fluxes. During growth, the open and close times of the indium and gallium shutters were carefully monitored, while keeping the nitrogen shutter continuously open. The indium composition in the InGaN alloys was changed by varying the In to Ga ratio. To prevent thermal decomposition during cooling, a 10-nm thick GaN layer was used to cap the $In_xGa_{1-x}N$ films. More details of the growth conditions can be found elsewhere.[9]

4.2.2. Determination of Alloy Composition

X-ray diffraction (XRD) and Rutherford backscattered spectroscopy (RBS) were used to measure the indium composition of the $In_xGa_{1-x}N$ epilayers. Bragg diffraction in XRD measures the crystalline interplanar separation and can have high accuracy in the determination of the indium composition in free-standing InGaN films, when there is no strain and the crystal defect density is low. However that is not the case in our films, which are subjected to large misfit strain and possible composition inhomogeneities. Our films were excited by Cu-K_α radiation and the XRD intensity was collected by a triple-

axis detector using a (220) Ge monochromator, in a *PANalytical X'Pert Pro* x-ray diffractometer.

Alpha particle scattering in RBS is highly sensitive to the atomic mass and provides a composition depth profile that is independent of the atom position in the lattice and of the strain resulting from elastic stress and crystal defects. The RBS spectra were obtained from a General Ionex 1.7 MV high current tandem accelerator (Tandetron) using a 2-MeV He^{++} ion beam. The detector was fixed at 170^{o} with respect to incident ion beam direction to receive the backscattered alpha particles. A standard RBS analysis package was used for simulation to determine alloy compositions.[10] We find that chemical composition analysis by RBS is more reliable than by XRD because it is not affected by strain and by the presence of defects.

4.2.3. Structural Characterization

Transmission electron microscopy (TEM) has been used to determine the microstructure of the InGaN films. TEM measurements were performed using a JEOL JEM 4000-EX high-resolution electron microscope operated at 400 kV and equipped with a double-tilt, top-entry specimen holder. The defect structure was determined using diffraction contrast techniques, and details about the atomic arrangement were found using high-resolution lattice imaging. Specimens for cross-sectional TEM were first thinned down to ~1 μm using standard mechanical wedge polishing techniques. Further thinning was done by argon-ion milling with the sample held at liquid nitrogen temperature to avoid indium diffusion. The TEM foils were prepared along $< 1\bar{1}00 >$

and $< 11\bar{2}0 >$ projections for diffraction contrast and high-resolution lattice imaging. For detailed sample preparation, refer to Chapter 3, Section 5.

4.2.4. Optical Characterization by Photoluminescence

Photoluminescence spectroscopy at 10 K was used to study the optical properties of the films. A 5-mW double-frequency Nd:YAG laser with a wavelength of 532 nm was used for excitation. Spectra were obtained using a 600 lines/mm grating, and the light intensity was measured with a liquid nitrogen cooled Ge photodiode with an integration time of one second.

4.3. Results

4.3.1. InGaN Epilayers with [In] ~ 22%

Figure 4.1 shows cross-section TEM bright-field images of an $In_{0.22}Ga_{0.78}N$ film viewed along the $< 11\bar{2}0>$ projection under diffraction conditions (a) $\boldsymbol{g}$ = 0002 and (b) $\boldsymbol{g} = 1\bar{1}00$. Basal plane stacking faults (BSF) are identified using diffracton contrast ($\boldsymbol{g.b}$ analysis) that gives defect visibility under $\boldsymbol{g} = 1\bar{1}00$ conditions in Fig. 4.1(b).[11] The BSFs appear as short segments ~10 nm long, and should terminate in partial dislocations. They are randomly distributed and exhibit a high density throughout the InGaN film. The BSFs density is observed to decrease in the GaN capping layer, where the BSFs dimensions become larger with a tendency towards a periodical separation along the growth direction.

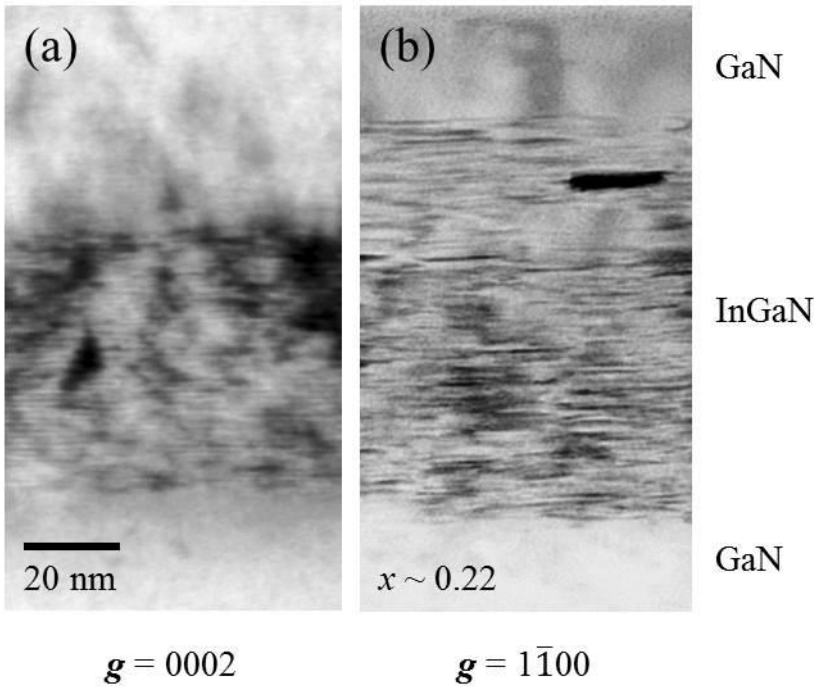

FIG. 4.1. Cross-section TEM bright-field images of the $In_{0.22}Ga_{0.78}N$ epilayer, taken along the $< 11\bar{2}0 >$ projection with diffraction contrast set at (a) $\boldsymbol{g} = 0002$, and (b) $\boldsymbol{g} = 1\bar{1}00$.

The presence and nature of the BSFs is confirmed in the selected-area diffraction (SAD) pattern in Fig. 4.2, taken along the $< 11\bar{2}0>$ projection of the $In_{0.22}Ga_{0.78}N$ film. The SAD pattern corresponds to an area that includes the GaN capping layer, the $In_{0.22}Ga_{0.78}N$ film, and part of the GaN underlayer. We observe elongation of the InGaN diffraction spots in the form of streaks along the ***c*** direction, which is due to reduced periodicity along the *c*-axis, and spots at 1/3 distance between main spots due to the BSFs. The separation of the GaN and $In_{0.22}Ga_{0.78}N$ diffraction spots are visible at higher order diffraction spots, e.g. for $\boldsymbol{g} = 1\bar{1}05$ in the lower right enlargement in the figure.

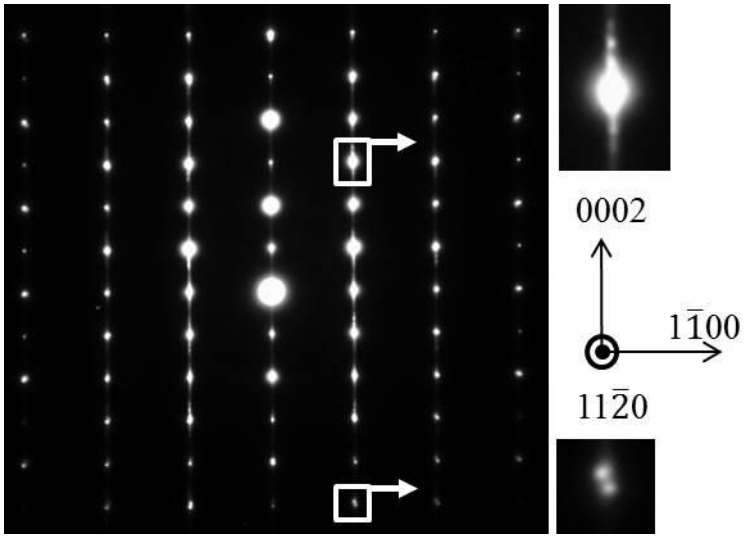

FIG. 4.2. Selected-area electron diffraction pattern of the $In_{0.22}Ga_{0.78}N$ film, viewed along the $\langle 11\bar{2}0 \rangle$ projection. Enlargement in the upper right shows a streak of satellite peaks, indicating presence of stacking faults along the growth direction. Enlargement in the lower right corresponds to a higher-order diffraction spot showing separation of GaN and InGaN diffraction spots.

The nature of the planar defects in the InGaN film was analyzed by high-resolution TEM (HRTEM). Figure 4.3 shows HRTEM images of the $In_{0.22}Ga_{0.78}N$ epilayer. The enlargements on the right correspond to the regions with high and low density of stacking faults. A competition between cubic and hexagonal structures is observed in the upper region, with a periodicity of about 4 nm. The region between stacking faults have a cubic "*ABCABC*" stacking sequence.

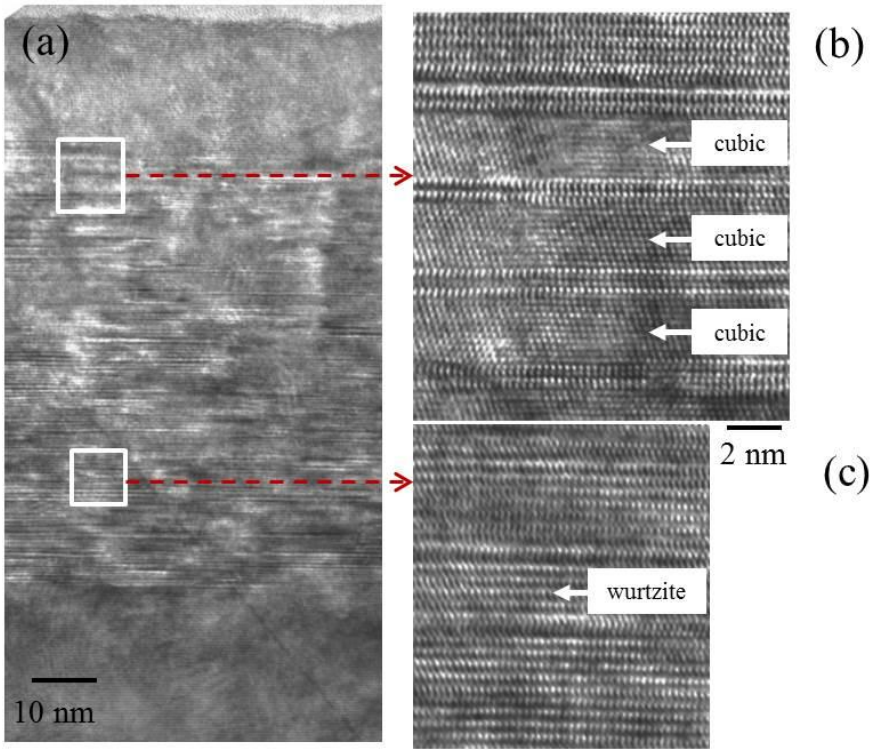

FIG. 4.3. High-resolution electron micrographs showing the atomic stacking sequence in the $In_{0.22}Ga_{0.78}N$ epilayer. (a) Overall structure of the $In_{0.22}Ga_{0.78}N$ film. (b) Cubic regions in the GaN capping layer. (c) Region near the GaN underlayer with high density of BSFs.

Figure 4.4 is a high-resolution electron micrograph of the $In_{0.22}Ga_{0.78}N$/GaN interface region. The phase contrast image shows lower-indium-content islands growing pseudomorphically in the shape of half-spheres, free of defects, with an average width of ~13 nm and average height of ~ 5 nm. Further growth appears to nucleate in between the islands and to grow laterally in the form of arches, as shown schematically in the lower portion of Fig. 4.4. Stacking faults nucleate at the edge of the islands and prevail in the two-dimensional lateral growth of the InGaN epilayer.

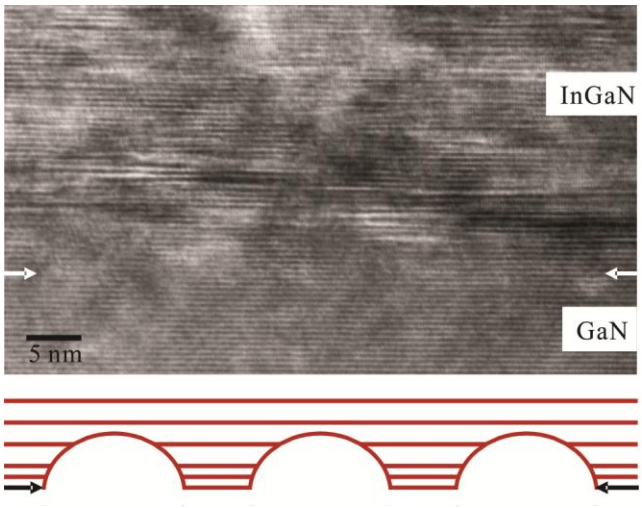

FIG. 4.4. High-resolution electron micrographs showing the $In_{0.22}Ga_{0.78}N$/GaN interface. A schematic representation below shows the initial growth of the $In_{0.22}Ga_{0.78}N$ layer. The horizontal lines represent stacking faults formed during growth.

4.3.2. InGaN Epilayers with [In] ~ 46%

Increasing the indium content leads to fine columnar domains. This is observed in the cross-section HRTEM image of the $In_{0.46}Ga_{0.54}N$ layer in Fig. 4.5, along the $\langle 11\bar{2}0 \rangle$ projection. As in the previous case (x ~ 0.22), the nucleation of InGaN is governed by lateral growth of islands with ~13 nm in width and ~5 nm in height. SAD patterns (not shown here) do not exhibit streaks along the *c*-axis that were associated with BSFs in Fig. 4.2. The InGaN epilayer exhibits fine columnar growth with lateral dimensions of ~ 10 nm (indicated by arrows). This results in an undulating rough top surface with an average crest separation of ~15 nm.

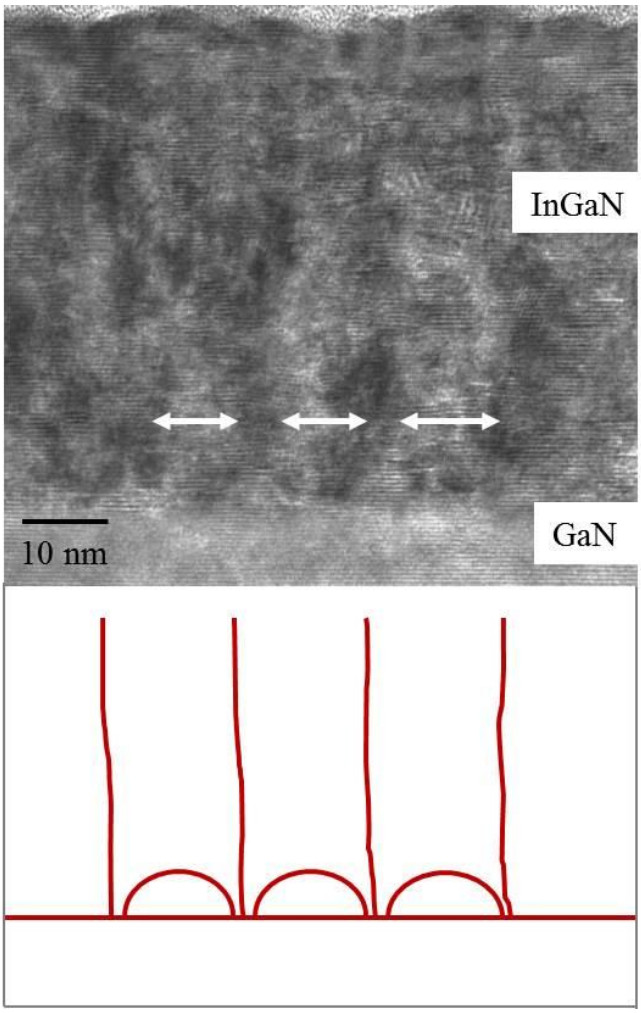

FIG. 4.5. High-resolution cross-section TEM image taken along $\langle 11\bar{2}0 \rangle$ projection. The vertical lines in the schematic representation below are domain boundaries. Notice that the patterns at the interface are also observed at the top surface.

4.3.3. InGaN Epilayers with [In] ~ 60%

A surprising transition in the microstructure is observed at x ~ 0.60, which requires a careful analysis of the relationship between structure and chemical composition. We first present the information obtained from XRD. Figure 4.6(a) is an

ω-2θ scan showing the (002) GaN and (002) $In_{0.60}Ga_{0.40}N$ diffraction peaks, located at 17.284° and 16.296°, respectively. Using Bragg's equation,

$$2d_{hkl}sin\theta = n\lambda, \tag{1}$$

where n = 1, λ = 1.5406 Å is the wavelength of Cu-$K_{\alpha 1}$ radiation, and d_{hkl} is the lattice spacing for a hexagonal crystal system given by

$$d_{hkl} = \frac{1}{\sqrt{\frac{4}{3a^2}(h^2+hk+k^2)+\frac{l^2}{c^2}}} \tag{2}$$

We obtain the InGaN lattice parameter c = 0.5490 nm. Applying a linear interpolation (Vegard's law) for GaN (c = 0.5185 nm) and InN (c = 0.57 nm), the indium composition of the epilayer is found to be $x \sim 0.60$. Figure 4.6(b) shows the RBS spectrum. The expected scattering energies for Ga and In atoms by 2 MeV He^{++} ions are 1.592 and 1.742 MeV, respectively. The experimental results are fitted with a simulation software, which shows that indium content in the $In_xGa_{1-x}N$ epilayer is x = 0.60. The good agreement between XRD and RBS measurements is attributed to the unstrained nature of the InGaN layer, as discussed in the next two paragraphs.

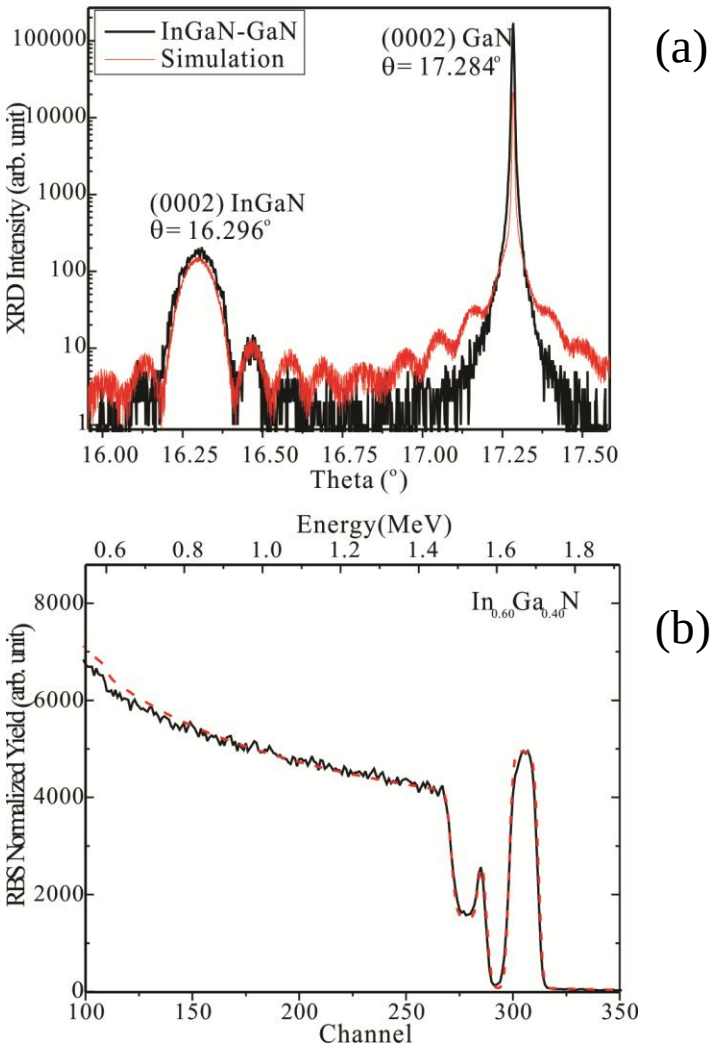

FIG. 4.6. Composition determination for the InxGa1-xN film with x ~ 0.60 using: (a) XRD ω–2θ scan and (b) RBS spectrum. Red lines represent corresponding simulations.

XRD rocking curves give information about the epitaxial nature of the InGaN films. Figure 4.7 shows XRD rocking curves of the (002) diffraction peaks for GaN and $In_{0.60}Ga_{0.40}N$. The rocking curve for GaN in Fig. 4.7(a) has been fitted with two Gaussian curves, which based on relative intensities we assign to the GaN underlayer and to the GaN capping layer. The full-width-at half-maximum (FWHM) of the GaN underlayer is

~ 5.8 arcmin whereas of the GaN capping layer is ~ 9.4 arcmin. The latter has a larger FWHM than the GaN underlayer because it was grown over the (rougher) InGaN surface, which has a FWHM of ~ 8.1 arcmin in Fig. 4.7(b).

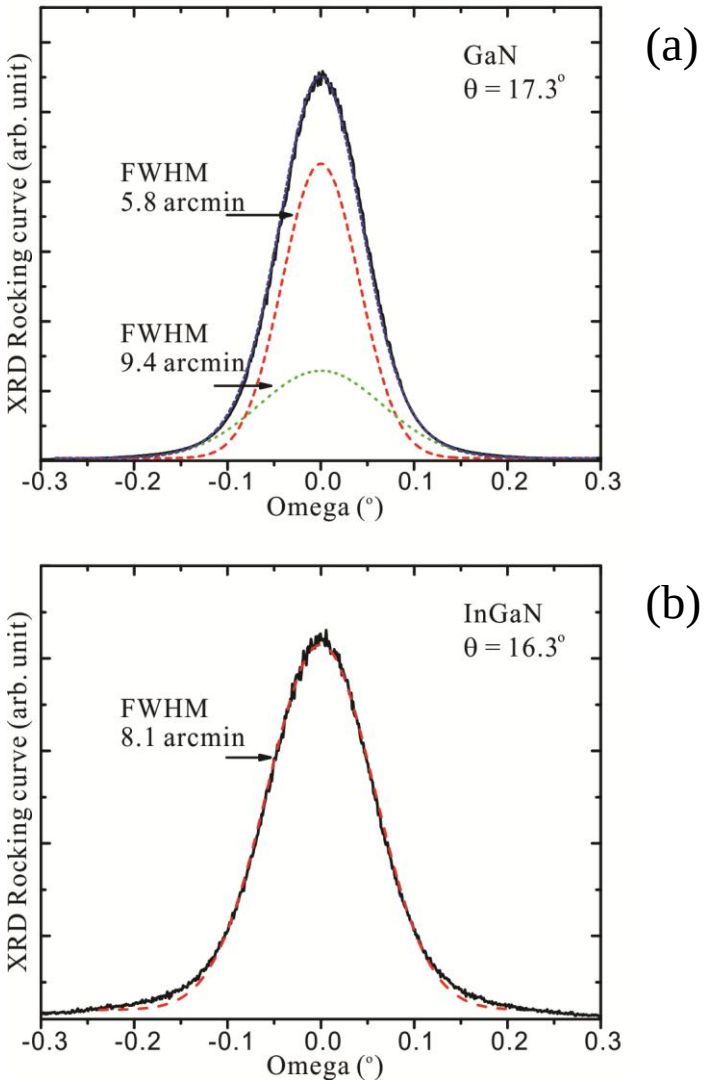

FIG. 4.7. (a) X-ray rocking curve for the (002) GaN peak. The green and red Gaussian curves with a FWHM of 6.15 and 13.07 arcmin correspond to the GaN underlayer and the GaN capping layer. (b) X-ray rocking curve for (002) $In_{0.60}Ga_{0.40}N$ layer with a FWHM of 8.09 arcmin.

Cross-sectional two-beam bright-field images were taken along $\langle 11\bar{2}0 \rangle$ projection with (a) $\boldsymbol{g} = 0002$ and (b) $\boldsymbol{g} = 1\bar{1}00$. In Fig. 4.8(a) the $In_{0.60}Ga_{0.40}N$/GaN lower interface is flat. However, the top interface is slightly rough. Evidence of moiré fringes are observed in the periodic fluctuations in contrast at the bottom $In_{0.60}Ga_{0.40}N$/GaN interface in Fig. 4.8(b), indicating an abrupt change in lattice parameter. The average fringe separation *D* between dark fringes is 5.6 nm. The degree of relaxation of the $In_{0.60}Ga_{0.40}N$ layer can be estimated by taking the ratio of the experimental and expected moiré fringes separation *D* which is given by:

$$D = \frac{d_{InGaN} \times d_{GaN}}{d_{InGaN} - d_{GaN}} \quad (3)$$

where d_{InGaN} and d_{GaN} are the $\{1\bar{1}00\}$ interplanar separations for $In_xGa_{1-x}N$ and GaN. Using the interplanar separations obtained from XRD and TEM in Eq. (3), a value *D* = 4.5 nm is obtained, which is smaller than the experimental fringe separation of 5.6 nm. The difference in D values indicates that the $In_{0.60}Ga_{0.40}N$ layer is only partially relaxed at the interface with a degree of relaxation of ~ 80%. In addition, alternating bright and dark domains in Fig. 4.8(b) indicate columnar domain rotation about the *c*-axis.[12] This is confirmed by the SAD pattern in Fig. 4.8(c), where we observe elongation of the diffraction spots along the horizontal $[1\bar{1}00]$ direction. A straight line drawn from the $(\bar{1}102)$ to $(1\bar{1}0\bar{2})$ GaN diffraction spots passing through the origin shows that the equivalent InGaN diffraction spots fall on the same straight line, consistent with the view that the $In_{0.60}Ga_{0.40}N$ epilayer is significantly relaxed.

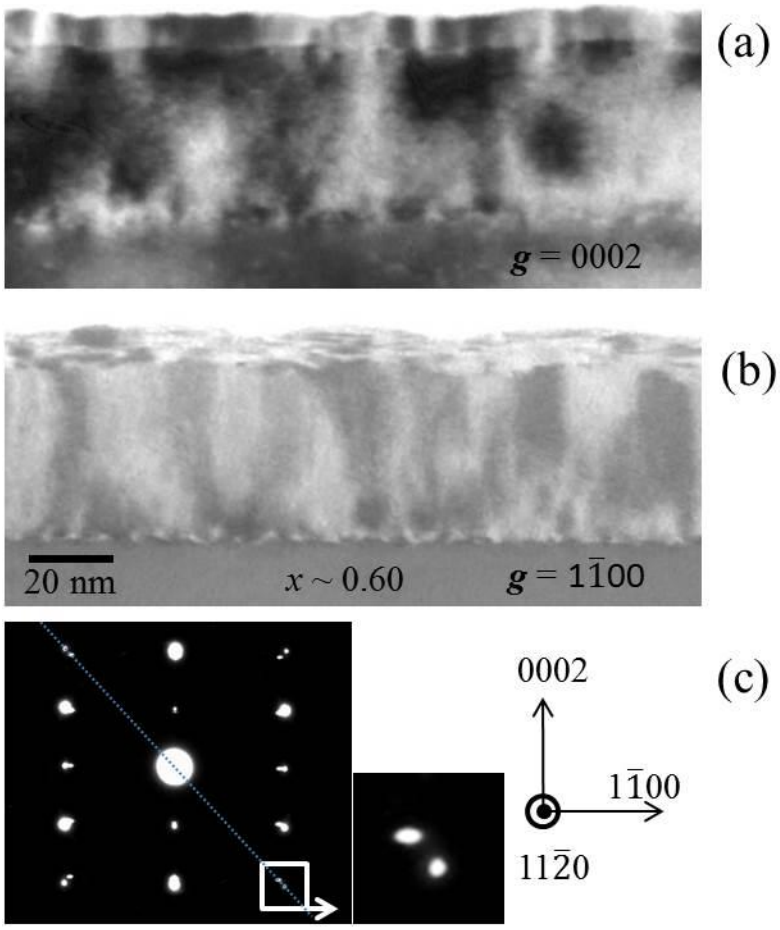

FIG. 4.8. Cross-section bright-field TEM image of $In_{0.60}Ga_{0.40}N$ film. Bright-field images taken at (a) $\boldsymbol{g} = 0002$ and (b) $\boldsymbol{g} = 1\bar{1}00$. (c) Selective area diffraction pattern taken from an area across the $In_{0.60}Ga_{0.40}$/GaN interface along the $< 11\bar{2}0 >$ projection. A dotted straight line is drawn across the $(\bar{1}102)$, (000), and $(1\bar{1}0\bar{2})$ spots.

The appearance of luminescence has been observed at x = 0.60. Figure 4.9 is a photoluminescence (PL) spectrum of the $In_{0.60}Ga_{0.40}N$ film taken at 10 K, with a peak maximum centered at ~ 935 nm and a FWHM of 216 nm (305 meV). This is particularly interesting since the samples with x = 0.22 and 0.46 did not show any significant luminescence.

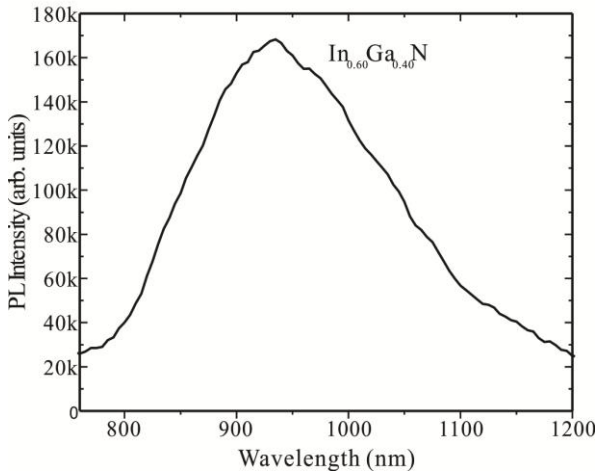

FIG. 4.9. Photoluminescence spectrum at 10 K for the $In_{0.60}Ga_{0.40}N$ film.

4.3.4. InGaN Epilayers with [In] ~ 67%

Increasing the indium content to 67% leads to further improvements in the optical and structural properties. Figure 4.10 shows XRD spectra with a (002) InGaN peak at θ = 16.168^{o}, corresponding to 67% indium content, consistent with RBS measurements (not shown here).

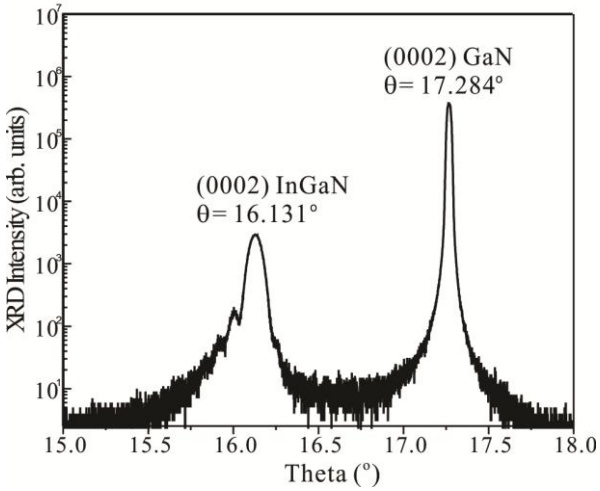

FIG. 4.10. Indium composition determination for the $In_{0.67}Ga_{0.33}N$ film by XRD ω–2θ scan.

Figure 4.11 shows XRD rocking curves of the (002) GaN and (002) $In_{0.67}Ga_{0.33}N$ diffraction peaks. The GaN rocking curve in Fig. 4.11(a) is fitted with two Gaussian fits for the GaN underlayer and GaN capping layer. The GaN underlayer has a FWHM of ~5.8 arcmin whereas the GaN capping layer has a FWHM of 11.5 arcmin. The InGaN layer has a FWHM of 8.5 arc min.

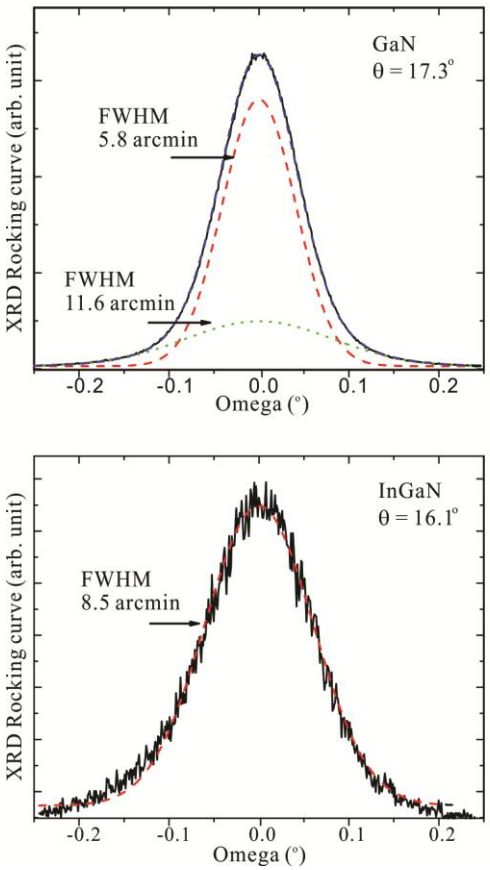

FIG. 4.11. Crystal structure characteristics of the In0.67Ga0.33N film. (a) X-ray rocking curve for GaN: The GaN underlayer has a FWHM of 5.8 arcmin (dashed Gaussian curve), while the GaN capping layer has a FWHM of 11.6 arcmin (dotted curve). (b) X-ray rocking curve corresponding to the $In_{0.67}Ga_{0.33}N$ film, with a FWHM of 8.5 arcmin.

Figure 4.12(a) shows a cross-section bright-field TEM image of the $In_{0.67}Ga_{0.33}N$ film, taken along the $\langle 11\bar{2}0\rangle$ projection with $\boldsymbol{g} = 0002$. The bottom InGaN/GaN interface is sharp and flat, while the upper interface is undulated with period and amplitude of ~ 45 and 5 nm, respectively. Figure 4.12(b) corresponds to an image of the same region taken with $g = 1\bar{1}00$. Uniform periodic moiré fringes are observed at the bottom interface due to the overlap of the lattice planes of $In_{0.67}Ga_{0.33}N$ and GaN. Using the average moiré fringe separation of ~ 4.06 ± 0.04 nm in Eqn. (2), we find a value of *x* = 0.66 and a degree of relaxation of ~ 97%. Figure 4.12(c) is a SAD pattern taken along the $\langle 11\bar{2}0\rangle$ projection of the InGaN/GaN interface region. The InGaN and GaN diffraction spots at $(\bar{1}102)$ and $(1\bar{1}0\bar{2})$ line up along a straight line of the origin, consistent with full relaxation of the $In_{0.67}Ga_{0.33}N$ epilayer.

We next explore the microstructure of these films along a different crystal projection. Cross-section TEM images of the $In_{0.67}Ga_{0.33}N$ film taken along the $\langle 1\bar{1}00\rangle$ projection are shown in Fig. 4.13. The surface undulations are consistent with those in Fig. 4.12(a), implying the presence of a cross-hatch surface morphology, with hillocks separated by ~ 45 nm along the $\langle 11\bar{2}0\rangle$ direction. We attribute these surface undulations to low-angle domain boundaries. In Fig. 4.13(b), taken with $g = 11\bar{2}0$, the $In_{0.67}Ga_{0.33}N$ layer exhibits alternating bright and dark regions that indicate a columnar structure with low-angle columnar domain boundaries associated with slight crystal rotations about the *c*-axis.[18] The columnar domain width and the layer thickness are of the order of 50 nm. The moiré fringes at the $In_{0.67}Ga_{0.33}N$/GaN interface have a fringe separation of ~ 2.36 nm, which corresponds to the $\{11\bar{2}0\}$ planes and is about $1/\sqrt{3}$ the value of 4.06 nm

for the $\{1\bar{1}00\}$ planes in Fig. 4.12(b), showing that misfit relaxation occurs along the full interface plane.

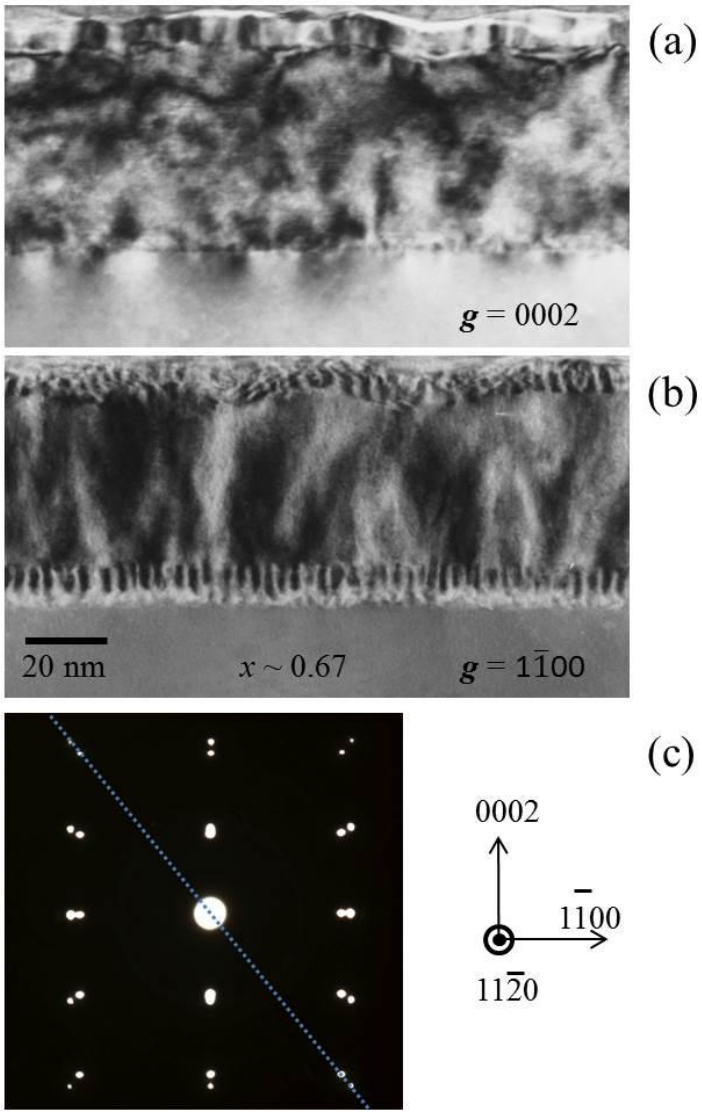

FIG. 4.12. Cross-section bright-field TEM image of $In_{0.67}Ga_{0.33}N$ film with (a) $\boldsymbol{g} = 0002$ and (b) $\boldsymbol{g} = 1\bar{1}00$. (c) Selected-area electron diffraction pattern along the $\langle 11\bar{2}0 \rangle$ projection, from an area across the interface between the GaN underlayer and the

$In_{0.67}Ga_{0.33}N$ film. A dotted straight line is drawn across the $(\bar{1}102)$, (0000), and $(1\bar{1}0\bar{2})$ spots, indicating full misfit strain relaxation.

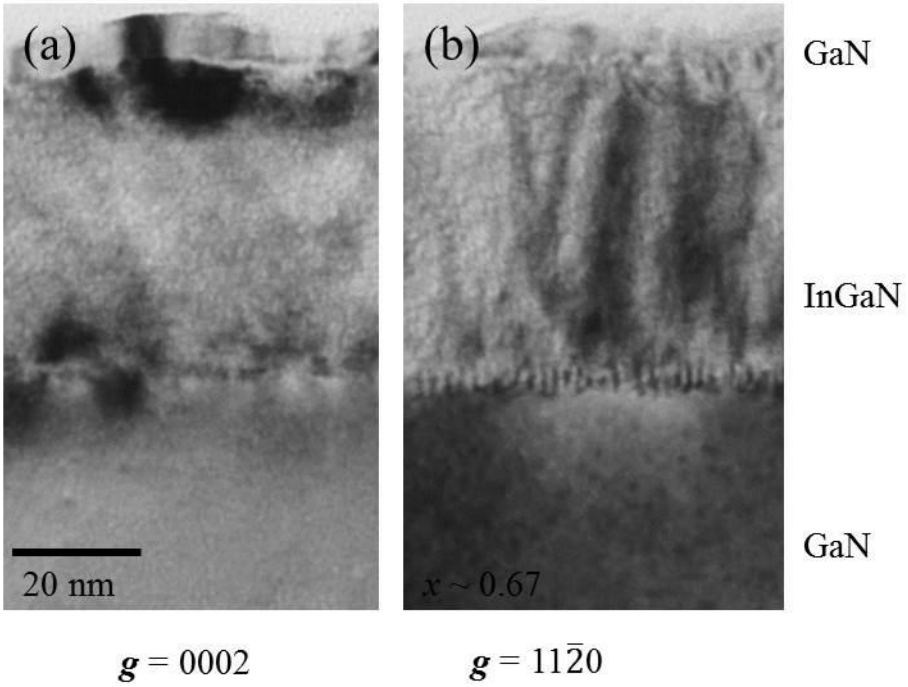

FIG. 4.13. Cross-section bright-field TEM images of the $In_{0.67}Ga_{0.33}N$ film along the $\langle 1\bar{1}00\rangle$ projection with (a) $\boldsymbol{g} = 0002$ and (b) $\boldsymbol{g} = 11\bar{2}0$.

The moiré fringes at the base of the InGaN columnar structure are consistent with misfit dislocations on the basal plane of the 60-degree type, at intervals of 4.06 nm, over domains with diameter of ~ 50 nm. Slight misalignment of the columns about the *c*-axis results in the formation of rotated crystal domains, as shown in Fig. 4.13(b). Incongruity in misfit dislocation arrays at the base of the columns leads to bending of unpaired dislocations that thread along the growth direction, resulting in the formation of low-angle twist domain boundaries, as depicted in Fig. 4.14.

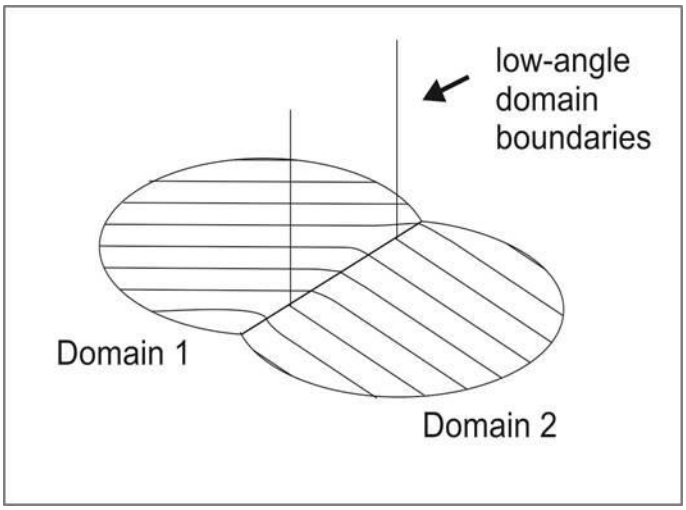

FIG. 4.14 Schematic of misfit dislocation mismatch between two adjacent domains with a slight twist.

While a weak PL emission was observed for the case of 60% In composition, a significantly stronger emission is observed at 67%. The PL spectrum of the $In_xGa_{1-x}N$ film with $x \sim 0.67$ indium content, taken at 10 K is shown in Fig. 4.15. After removing the Fabry-Pérot interference due to the 4-μm thick GaN underlayer, the $In_{0.67}Ga_{0.33}N$ peak emission wavelength is found to be 1300 nm with a FWHM 236 nm (175 meV).

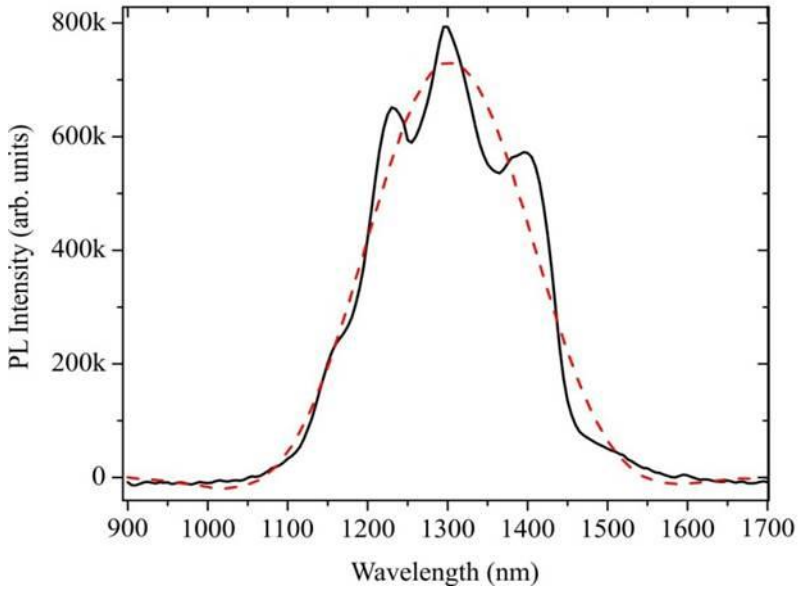

FIG. 4.15. Photoluminescence spectra at 10 K for the $In_{0.67}Ga_{0.33}N$ film. The dashed line has been obtained by removing the thickness interference produced by the 4-μm-thick GaN underlayer.

4.4. Discussion

The evolution of the microstructure follows a clear pattern that we next show is related to the critical thickness for misfit dislocation generation. We will use critical thickness models described in chapter 2.

4.4.1. Critical Thickness for Misfit Strain Relaxation in Thin Film Epitaxy

The critical thickness for the $In_xGa_{1-x}N$/GaN system as a function of indium content is shown in Fig. 4.16, for theoretical models used in the literature.[5][13][14] The calculations involve solving transcendental equations numerically, which are only feasible up to $x \approx 0.43$. The critical thickness values for $x > 0.43$ are obtained by

extrapolation, as shown in the figure. The parameters for the binary compounds are a_{AlN} = 0.3112 nm; a_{GaN} = 0.3189 nm; a_{InN} = 0.354 nm; c_{GaN} = 0.5185 nm; c_{InN} = 0.57 nm; G_{InN} = 45 GPa; G_{GaN} = 200 GPa.[5][7][15] The critical thickness of one lattice period c (~ 0.52 nm) happens at x ~ 0.55. The critical thickness for different indium compositions based on Srinivasan's model is summarized in Table 4.1. It should be noted that several assumptions and approximations are made in critical thickness calculations, not only in the mathematical methods used but also in the values of the materials parameters. The latter, such as the Poisson's ratio, are not well known.

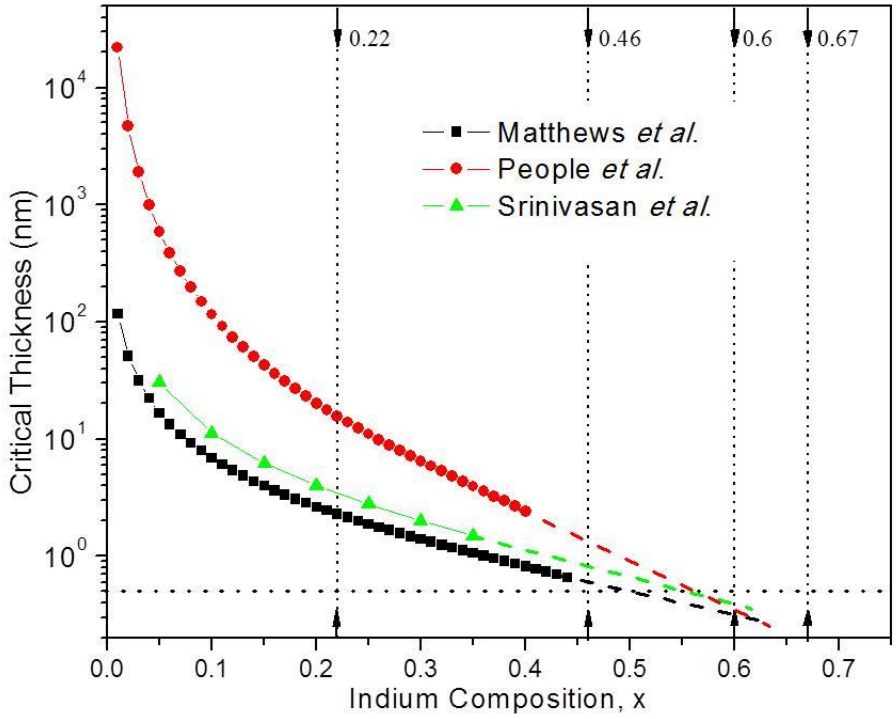

FIG. 4.16. Critical thickness vs. indium content x for the $In_xGa_{1-x}N$/GaN system using three different models. The critical thickness of one lattice period c (horizontal dotted line) happens at x = 0.55.

Table 4.1. Critical thickness for plastic deformation in $In_xGa_{1-x}N$ epilayers on GaN, using Srinivasan's critical thickness approach.[5]

	Indium composition *x*			
	0.22	0.46	0.60	0.67
Critical thickness (nm)	3.32	0.81	0.37	0.26

4.4.2. $In_xGa_{1-x}N$ Thin Film Microstructure Evolution with Indium Composition

The main point of this paper is that the microstructure evolution of $In_xGa_{1-x}N$/GaN grown by MME can be explained by taking into consideration the critical thickness dependence on indium composition.

$In_xGa_{1-x}N$ films with x = 0.22 on GaN substrates follow the Stranski-Krastanov growth mode. They initially grow pseudomorphically with an estimated compressive strain of 2.4% along the *a*-axis, and after a few monolayers, growth become three-dimensional with the formation of islands, as observed in Fig. 4.4. The critical thickness for plastic relaxation is 3.32 nm, i.e. more than twelve basal plane monolayers. Island formation leads to another mechanism of strain relaxation by additional free surface area. Lateral strain relaxation in between the islands lead to generation of dislocations that dissociate and produce stacking faults. Subsequent growth suggests columnar domains with a diameter of ~20 nm in Fig. 4.1(a). The disparity in columnar domain orientation and dimension generates a high density of stacking faults due to stacking order mismatch, as observed in Fig. 4.1(b). The stacking fault formation is associated with a rough growth

surface that continues into the GaN layer. The position of the GaN/InGaN interface in Fig. 4.1(b) was confirmed with energy dispersive x-ray spectroscopy. These observations are consistent with reports in the literature. It has been reported that thin film growth under compressive and pseudomorphic conditions lead to Stranski-Krastanov growth mode.[16]This growth mode alone has been shown to lead to competing island growth that results in high densities of stacking faults in GaN growth by MOCVD,[17] with a competition between cubic and hexagonal regions as observed in Fig. 4.3. Rearrangement of the stacking sequence leading to stacking faults has been reported for InGaN films with $x = 0.33$ grown by MOCVD.[18]

For $In_xGa_{1-x}N$ films with $x = 0.46$, the expected critical thickness from Table 4.1 is 0.81 nm, which is about three basal plane monolayers. The microstructure is similar to the $x = 0.20$ case, with initial island formation followed by columnar domains with diameter ~ 15 nm (Fig. 4.5). Threading dislocations and stacking faults are observed in between the columns, suggesting that the center of the columns grow first, and the defects occur at the coalescence of the columns. Fewer stacking faults are evident in TEM images, with reduced dimensions. A few misfit dislocations are observed at the InGaN/GaN interface, with a separation of ~ 11.5 nm (not shown). A completely relaxed $In_{0.46}Ga_{0.54}N$ film on GaN should exhibit misfit dislocation separated by 5.7 nm (Fig. 4.17 and Table 4.2). Therefore, the presence of dislocations indicates that the InGaN film is partially relaxed; the residual strain giving rise to the columnar growth. An early strain relaxation in the InGaN epilayers via the accommodation of dislocations at the InGaN/GaN interface may reduce the domain size, and thus shorten the length of the stacking faults.

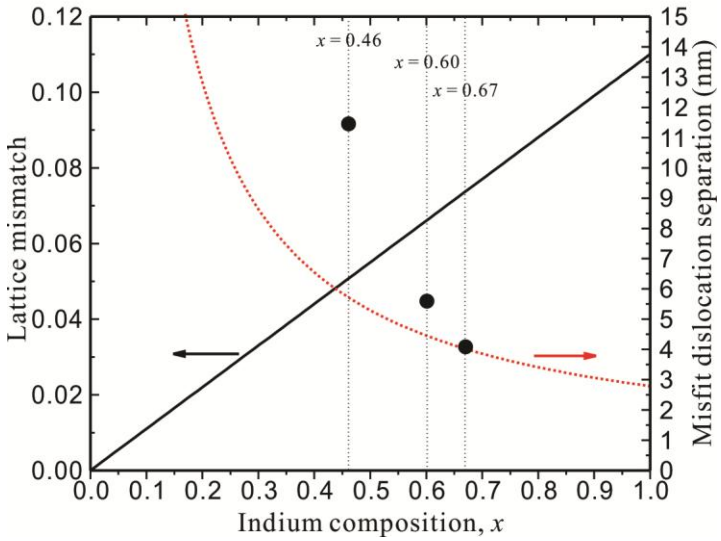

FIG. 4.17. Calculated lattice mismatch and misfit dislocation separation vs. indium composition for the $In_xGa_{1-x}N/GaN$ system with x = 0.22, 0.46, 0.60, and 0.67. Black dots are experimental data.

Table 4.2. Theoretical and experimental values of misfit dislocation separation at the $In_xGa_{1-x}N/GaN$ interface for various indium contents.

Indium content x	0.22	0.46	0.60	0.67
Misfit separation (nm)				
Expected	11.68	5.73	4.46	4.02
Experimental	- -	11.45	5.62	4.06

For $In_xGa_{1-x}N$ films with x = 0.60, the expected critical thickness is 0.37 nm, which is about 1.4 basal plane monolayers. We observe a significant improvement in the InGaN film quality; no stacking faults are observed suggesting two-dimensional epitaxial growth (Fig. 4.8). Periodic arrays of moiré fringes are observed at the InGaN/GaN

interface, with a separation of 5.62 nm, close to the expected 4.46 nm separation between misfit relaxation in a fully relaxed condition, indicative of about 79% relaxation. The incomplete relaxation may give rise to a slight rotational asymmetry in a columnar domain structure, observed in the diffraction contrast images (Fig. 4.8). The improved structural quality also results in improved optical properties reflected in the PL spectra (Fig. 4.9)

For $In_xGa_{1-x}N$ films with x = 0.67, the expected critical thickness is 0.26 nm, which is about 0.94 basal plane monolayers. Uniform arrays of moiré fringes indicate full plastic relaxation occurs, with periodic arrays of misfit dislocations at the InGaN/GaN interface (Fig. 4.12). This is consistent with the concept that below a monolayer the atomic arrangement is unstable until a sufficient number of atoms are available for the material to acquire its own identity, at which point it crystallizes with its own lattice parameter, misfit dislocations appearing spontaneously, without the need of nucleating at a surface and then traveling through slip planes.

4.4.3. Misfit Strain Relaxation and High Luminescence Characteristics

A significant increase in the PL intensity of the InGaN films has been observed as the critical thickness approached the monolayer level. The nature of the PL spectrum in Fig. 4.15 can be explained from the alloy properties. In the absence of elemental ordering via the formation of superlattices or clusters, a random compositional distribution results in potential fluctuations.[19] Such random distribution is a result of diffusion, contrary to chemical segregation that leads to phase separation. From the luminescence point of view, we expect that the linewidth of an emission peak becomes

broader with alloy disordering, following a binomial distribution variance of $\sigma^2 \propto x(1-x)$. Thus a random distribution of anions in the material leads to the largest broadening at an alloy composition of x = 0.5. The full-width-at-half-maximum (i.e. linewidth) of the photoluminescence (PL) emission peak of InGaN alloys have been reported to increase up to four times with respect to their binary case[20] The luminescence linewidth for $In_xGa_{1-x}N$ films with x = 0.60 and 0.67 was found to decrease from 305 meV (Fig. 4.9) to 175 meV (Fig. 4.15), respectively. The latter value agrees well with other published values.[20] We then conclude that for this composition InGaN films grown by MME experience no phase separation but only random alloying effects.

4.5. Conclusions

The evolution the microstructure of InGaN alloys grown by metal-modulated epitaxy has been studied for the range in composition from x = 0.22 to 0.67. A significant improvement in the structural quality was observed at x = 0.60. We explain the defect structure in terms of Stranski-Krastanov early stages of growth and in terms of the critical thickness required for misfit dislocation generation. We show that when the critical thickness is of the order of a basal-plane monolayer, regular arrays of misfit dislocations provide full lattice mismatch strain relaxation. We also show that under such conditions the optical quality of the material improves significantly. The 2_D nucleation of misfit dislocations is attributed to the layer-by-layer growth method used.

References

[1] F. A. Ponce and D. P. Bour, Nature **386**, 351 (1997).

[2] D. Queren, A. Avramescu, G. Brüderl, A. Breidenassel, M. Schillgalies, S. Lutgen, and U. Strauss. Appl. Phys. Lett. **94**, 081119 (2009).

[3] T. Miyoshi, S. Masui, T. Okada, T. Yanamoto, T. Kozaki, S. Nagahama, and T. Mukai. Appl. Phys. Express **2**, 062201 (2009).

[4] J. Wu, W. Walukiewicz, K. M. Yu, W. Shan, J. W. Ager III, E. E. Haller, H. Lu, W. J. Schaff, W. K. Metzger, and S. Kurtz. J. Appl. Phys. **94**, 6477 (2003).

[5] S. Srinivasan, L. Geng, R. Liu, F.A. Ponce, Y. Narukawa, and S. Tanaka, Appl. Phys. Lett. **83**, 5187 (2003).

[6] M. Moseley, J. Lowder, and D. Billingsley, Appl. Phys. Lett. 97, 191902 (2010).

[7] A. M. Fischer, Y. O. Wei, F. A. Ponce, M. Moseley, B. Gunning, and W. A. Doolittle, Appl. Phys. Lett. **103,** 131101 (2013).

[8] S. D. Burnham, G. Namkoong, K.-K. Lee, and W. A. Doolittle, J. Vac. Sci. Technol. B **25**, 1009 (2007).

[9] M. Moseley, B. Gunning, J. Greenlee, J. Lowder, G. Namkoong, and W. A. Doolittle, J. Appl. Phys. **112**, 014909 (2012).

[10] RUMP, Program for the simulation and analysis of RBS data. See: W.K. Chu, J. W. Mayer, and M.-A. Nicolet, *Backscattering Spectrometry* (Academic Press, NY, 1978); and L. R. Doolittle, Nucl. Inst. Meth. B **9**, 344 (1985).

[11] R. Liu, A. Bell, F. A. Ponce, C. Q. Chen, J. W. Yang, and M. A. Khan, Appl. Phys. Lett. **86**, 021908 (2005).

[12] F. A. Ponce, MRS Bull. **22**, 51 (1997).

[13] J. W. Matthews and A. E. Blakeslee, J. Cryst. Growth **27**, 118 (1974).

[14] R. People and J. C. Bean, Appl. Phys. Lett. **47**, 322 (1985).

[15] K. Kim, W. R. L. Lambrecht, and B. Segall, Phys. Rev. B **53**, 16310 (1996).

[16] D. J. Eaglesham and M. Cerullo, Phys. Rev. Lett. **64**, 1943 (1990).

[17] X. H. Wu, D. Kapolnek, E. J. Tarsa, B. Heying, S. Keller, B. P. Keller, U. K. Mishra, S. P. DenBaars, and J. S. Speck, Appl. Phys. Lett. **68**, 1371 (196).

[18] H. K. Cho and G. M. Yang, J. Cryst. Growth **27**, **11**8 (2002).

[19] E. F. Schubert, E. O. Göbel, Y. Horikoshi, K. Ploog, and H. J. Queisser, Phys. Rev. B **30**, 813 (1984).

[20] T. Suski, G. Frassen, A. Kamińska, A. Khachapuridze, H. Teisseyre, J. A. Plesiewicz, L. H. Dmowski, H. Lu, W. J. Schaff, M. Kurouchi, and Y. Nanishi, Proc. SPIE **6473**, 647311 (2007).

CHAPTER 5

MICROSTRUCTURE OF HIGH-QUALITY HIGH-INDIUM-CONTENT InGaN LAYERS GROWN BY MODIFIED MOLECULAR BEAM EPITAXY WITH AlN BUFFER

In this chapter, high-indium-content thick InGaN films were grown by ENABLE-MBE using a well aligned AlN buffer to grow InGaN on sapphire substrates. The microstructure evolution of the InGaN films with indium composition in the range from 0.48 to 1.0 was investigated by transmission electron microscopy (TEM). At x = 0.48, $In_xGa_{1-x}N$ films are partially relaxed by misfit dislocations at InGaN/AlN interface. Fully lattice mismatch strain relaxation by misfit dislocations at the interface was observed for $In_xGa_{1-x}N$ films with x = 0.54, 0.60, 0.78, and 1.0. The novel ENABLE technique, contributes to growth of high quality AlN buffer layers and high quality thick InGaN films.*

(*) Part of his chapter have been published as:

J. J. Williams, T. L. Williamson, M. A. Hoffbauer, **Y. Wei**, N. N. Faleev, and C. Honsberg. *Growth of high crystal quality InN by ENABLE-MBE*. Physica Status Solidi (c), **11**, 577 (2014).

5.1. Introduction

The InGaN alloy system has attracted attention for solar cell applications [1,2,3] due to its energy band gap ranging from 0.7 (for InN) to 3.4 eV (for GaN), covering most of the solar spectrum.[4,5,6]. The wide range of energy band gaps provides design flexibility for device performance optimization. Difficulties in growth of high quality InGaN films have been discussed in Chapter 1. In Chapter 4, we studied the microstructure evolution of InGaN films on GaN buffer on sapphire substrates using the MME growth technique. High quality InGaN films was successfully realized under high lattice mismatch conditions by MME. In this chapter, we study microstructure evolution of $In_xGa_{1-x}N$/AlN heterostructures grown by ENABLE growth technique for x values of 0.48, 0.54, 0.60, 0.78, 0.84, and 1.0. Full misfit strain relaxation occurs for indium compositions higher than 0.54. It has been shown that AlN buffers on sapphire substrates have extremely low degree of crystal tilt, low dislocation densities and flat surfaces. The large lattice mismatch between InGaN and AlN enables full misfit strain relaxation of the InGaN film at a lower indium composition than InGaN on GaN buffer layer. The following sections will report on the growth of $In_xGa_{1-x}N$ films on AlN buffer layers grown at low temperatures (~500^oC) by energetic nitrogen atom beam lithography and epitaxy (ENABLE).

5.2. Experimental Techniques

III-nitride films are grown using a modified form of molecular beam epitaxy (MBE). The modification comes in the form of a custom-built nitrogen source known as ENABLE. This source uses a continuous wavelength (CW) laser (λ = 10.6 μm) to sustain

a sub-1-mm^3 plasma in a chamber filled with argon and N_2. The plasma enhances pressure behind a narrow (sub millimeter) aperture, and the effective pressure of the plasma generates a beam on the vacuum side of the aperture. Several layers of apertures and differential pumping ultimately create a collimated beam of energetic neutral nitrogen atoms and argon. The energy of the nitrogen atoms can be tuned from 0.5 to 2.0 eV. These energies are measured using a time-of-flight setup with a known distance between a chopper wheel and a mass spectrometer.

The rest of the MBE chamber is a combination of custom built hardware with commercial available metal sources and diagnostic equipment. Wafers are heated radiatively from a nearby pyrolitic boron-nitride heater plate. Group III metals are thermally evaporated from Knudsen effusion cells. A reflection high-energy electron diffraction (RHEED) setup is used to monitor the structure of the growth front. A residual gas analyzer (RGA) is used to track background gases and nitrogen consumption. The latter is qualitatively determined by following the nitrogen transient before and after shuttering of different sources.

InGaN films were grown on *c*-axis oriented wafers of α - Al_2O_3 substrates. The wafers were outgassed at 900^{o}C for 20 minutes, and subsequently nitridized at 350^{o}C for 25 minutes. An AlN buffer layer was grown at 800^{o}C for 5 minutes at growth rate of ~20 nm/min yielding a thickness of 100 nm. Subsequently, $In_xGa_{1-x}N$ films with x ~ 0.48, 0.54, 0.60, 0.78, and 0.84 were grown at 500^{o}C (400^{o}C for x = 1.0). Growth was initiated under N-rich conditions for the InGaN and AlN layers. After nucleation (*i.e.* one minute of growth), the nitrogen flux was brought to near stoichiometry by monitoring the nitrogen transient in the residual gas analyzer.

TEM was performed on a JEOL 4000EX with an acceleration voltage of 400 kV. Scanning transmission electron microscopy (STEM) was performed on a JEOL ARM 200F with a spherical aberration corrector for the probe. Photoluminescence spectroscopy at 10 K was performed at 10 K using a 5-mW double-frequency Nd:YAG laser with a wavelength of 532 nm for excitation.

5.3. Microstructure of InGaN Epilayer with [In] ~ 100%

Figure 5.1 shows cross-section TEM bright-field images of an InN film viewed along the $< 11\bar{2}0 >$ projection under (a) $\boldsymbol{g}$ = 0002 and (b) $\boldsymbol{g}$ = $11\bar{2}0$ diffraction conditions. The film thickness is 117 and 350 nm for the AlN and the InN layers. A sharp interface between the AlN buffer layer and the InN film is observed in Fig. 5.1(a). The surface of the InN film is slightly rough. The two imaging conditions highlight the different types of dislocations present in the material. Both AlN and InN films depict a low number of screw type dislocations (Fig. 5.1(a)). The density of edge dislocations is at least an order of magnitude higher in AlN layer than in InN layer (Fig. 5.1(b)). Alternative bright and dark contrast is observed in Fig. 5.1(b), indicating the InN epilayer consists of columnar domains with a relative rotation along the growth direction.

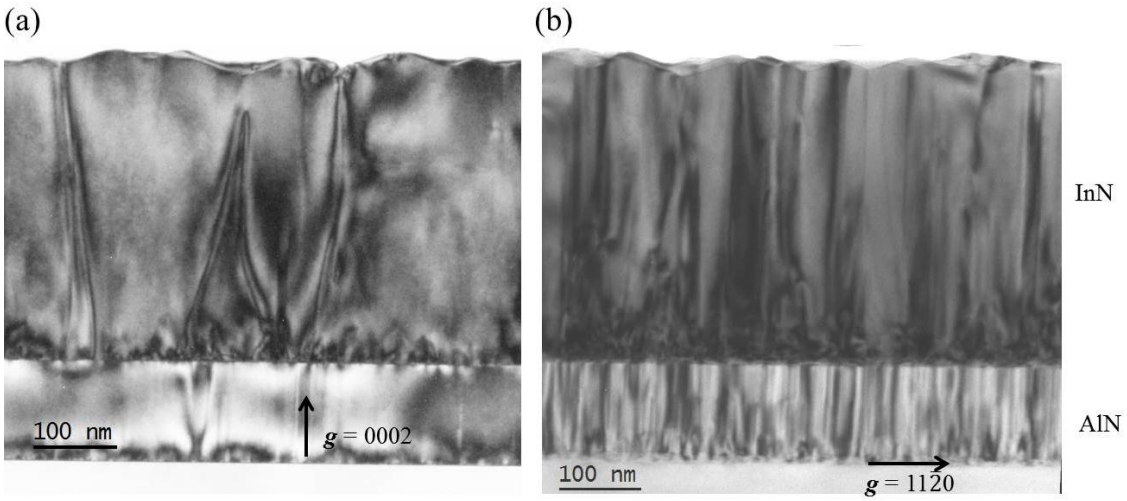

FIG. 5.1. Cross-section TEM images depict the different dislocation types based on diffraction condition. The image on the left, Fig. 5.1(a), ($\boldsymbol{g}$ = 0002) highlights screw-type dislocations. The image on the right, Fig 5.1(b), ($\boldsymbol{g}$ = $11\bar{2}0$) highlights edge-type dislocations.

Evidence of moiré fringes are observed as periodic contrast fluctuations at the InN/AlN interface shown in Fig 5.2(b), indicating an abrupt change in the in-plane lattice parameter. The average separation of moiré fringe is 1.30 ± 0.02 nm, which is close to expected moiré fringe separation 1.29 nm for a complete misfit strain relaxation.

Corresponding selected-area electron diffraction (SAED) pattern, in Fig 5.2(a), are taken along $< 1\bar{1}00 >$ projection. The InN diffraction spots and GaN diffraction spots at $(\bar{1}\bar{1}21)$ and $(11\bar{2}\bar{1})$ line up along a straight line of the origin, consistent with near-complete relaxation of the InN layer.

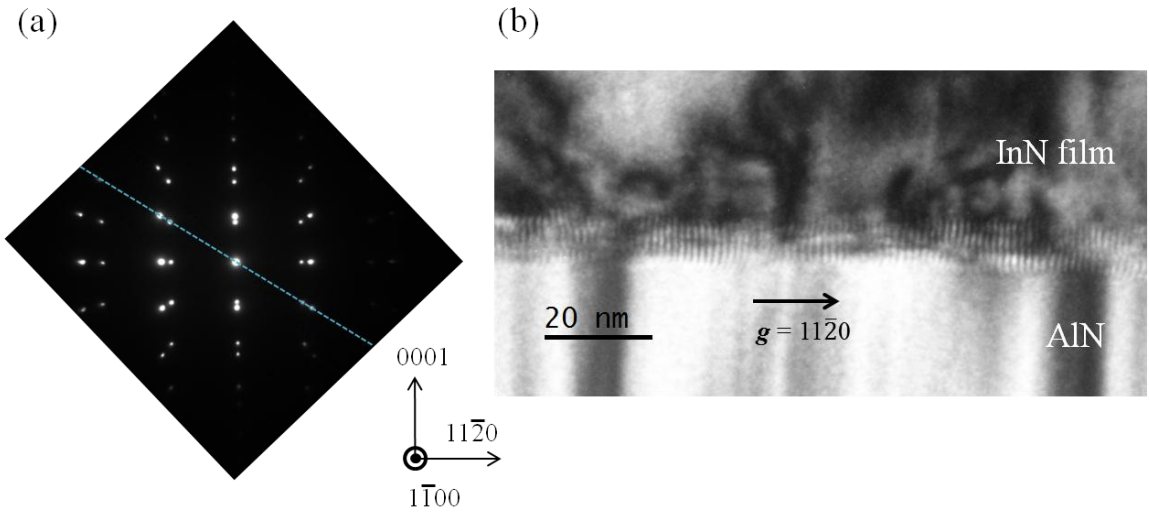

FIG. 5.2. (a) Selected-area electron diffraction (SAED) pattern along the $< \mathbf{1\bar{1}00} >$ projection, from an area across the interface between the AlN underlayer and the InN film. (b) Cross-section bright-field TEM image of InN film with $\boldsymbol{g} = \mathbf{11\bar{2}0}$.

5.4. Microstructure of InGaN Epilayer with [In] ~ 84%

Figure 5.3 shows cross-section TEM bright-field images of an $In_{0.84}Ga_{0.16}N$ film viewed along the $< 11\bar{2}0 >$ projection under (a) $\boldsymbol{g}$ = 0002 and (b) $\boldsymbol{g} = 1\bar{1}00$ diffraction conditions. The dislocation behavior in the epilayer is similar to the InN epilayer as discussed in section 5.3. Most of the dislocations are of the edge-type. In Fig. 5.3(b), taken with $\boldsymbol{g} = 1\bar{1}00$, the InGaN layer exhibits alternating bright and dark regions indicating a columnar structure with low-angle domain boundaries associated with slight crystal rotations about the *c*-axis. In addition, an amorphous layer with a thickness of ~50 nm and a dark contrast at the interface is observed at the InGaN/AlN interface. High-angle annular dark-field (HAADF) imaging and energy-dispersive X-ray spectroscopy (EDS) line scans were performed to analyze the composition of the amorphous layer.

Figure 5.4(a) is an HAADF image of the InGaN epilayer, showing an extra bright ~50 nm thick layer deposited at the InGaN/AlN interface. A line profile across the amorphous layer indicates a drop of gallium signal and increase of indium signal as shown in Fig. 5.4(b). This indicates that indium accumulated at the interface when growing InGaN film with [In] ~ 84%.

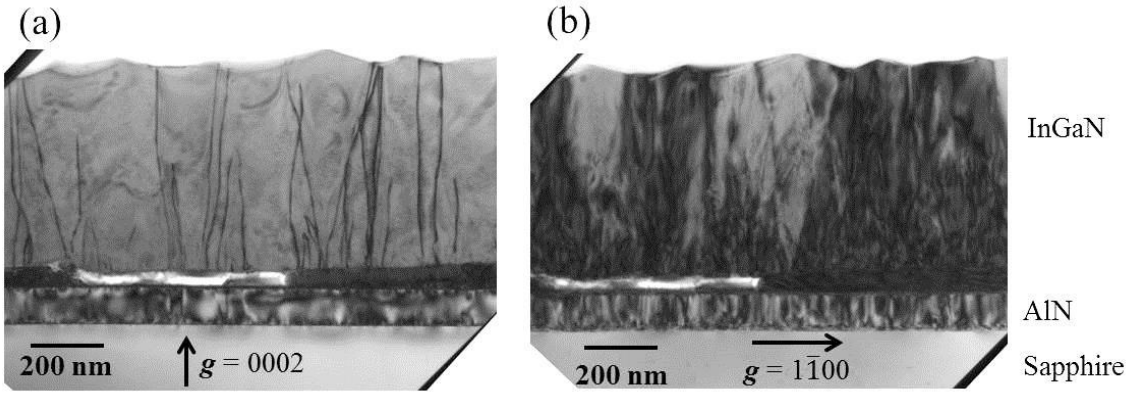

FIG. 5.3. Cross-section TEM bright-field image of $In_{0.84}Ga_{0.16}N$ epilayers with (a) $\boldsymbol{g}$ = 0002, (b) $\boldsymbol{g} = 1\bar{1}00$. A ~100 nm thick amorphous layer is observed at InGaN/AlN interface.

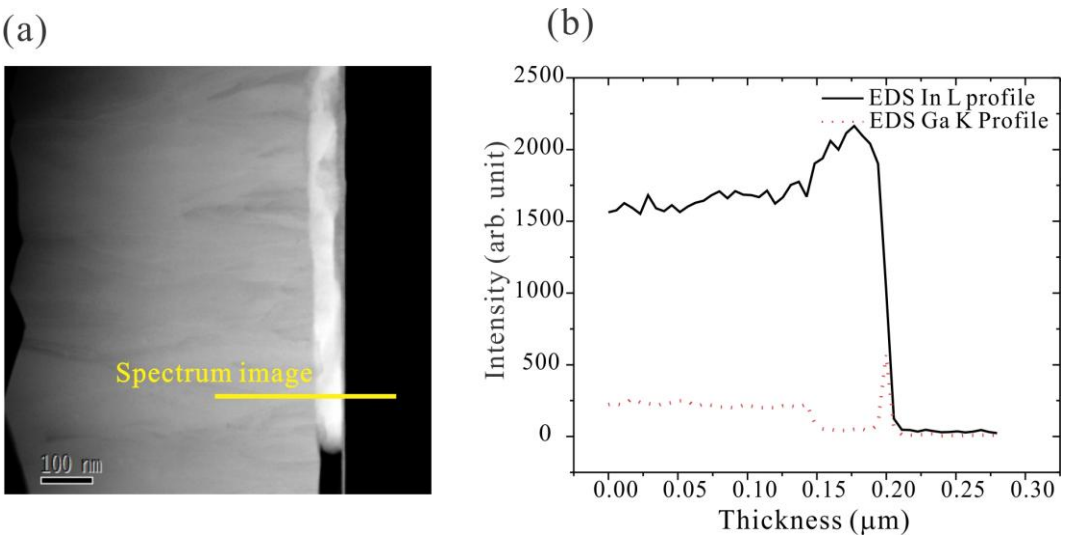

FIG. 5.4. Cross-section TEM of $In_{0.84}Ga_{0.16}N$ epilayers (a) HAADF image, (b) EDS profile taken from segment shown in (b).

5.5. Microstructure of InGaN Epilayer with [In] ~ 78%

Figure 5.5 shows cross-section TEM bright-field images of an $In_{0.78}Ga_{0.22}N$ film viewed along the $< 11\bar{2}0 >$ projection under $\boldsymbol{g}$ = 0002 diffraction condition. Bright-field images show a sharp interface of AlN and InGaN epilayer. We do not observe In accumulation at $In_xGa_{1-x}N$/AlN interface at x = 0.78. AlN buffer layer is 100 nm thick and InGaN epilayer is 630 nm thick. Very few screw-type threading dislocations are observed in cross-section TEM image in Fig. 5.5. Evidence of moiré fringes are observed as periodic contrast fluctuations at the InGaN/AlN interface shown in Fig 5.6, indicating an abrupt change in the in-plane lattice parameter. The average separation of moiré fringes is 2.74 $\pm$ 0.02 nm, which corresponds to an indium composition of x = 0.75 $\pm$ 0.01, indicating misfit strain is near complete relaxed by introducing of misfit dislocations at InGaN/AlN interface.

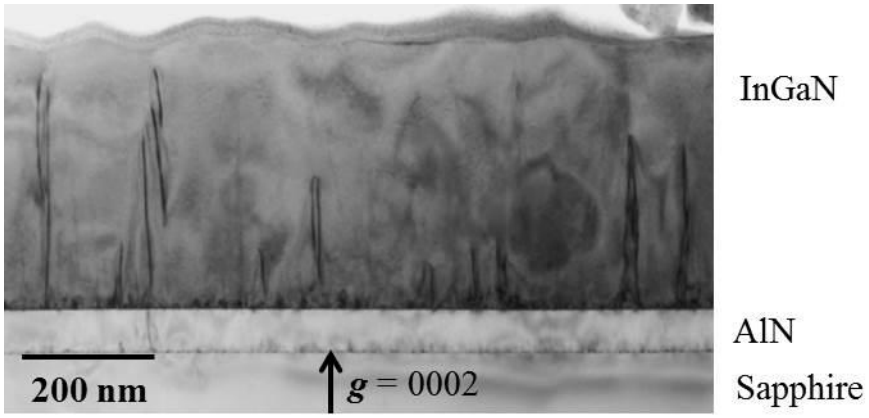

FIG. 5.5. Cross-section TEM bright-field image of $In_{0.78}Ga_{0.22}N$ epilayer.

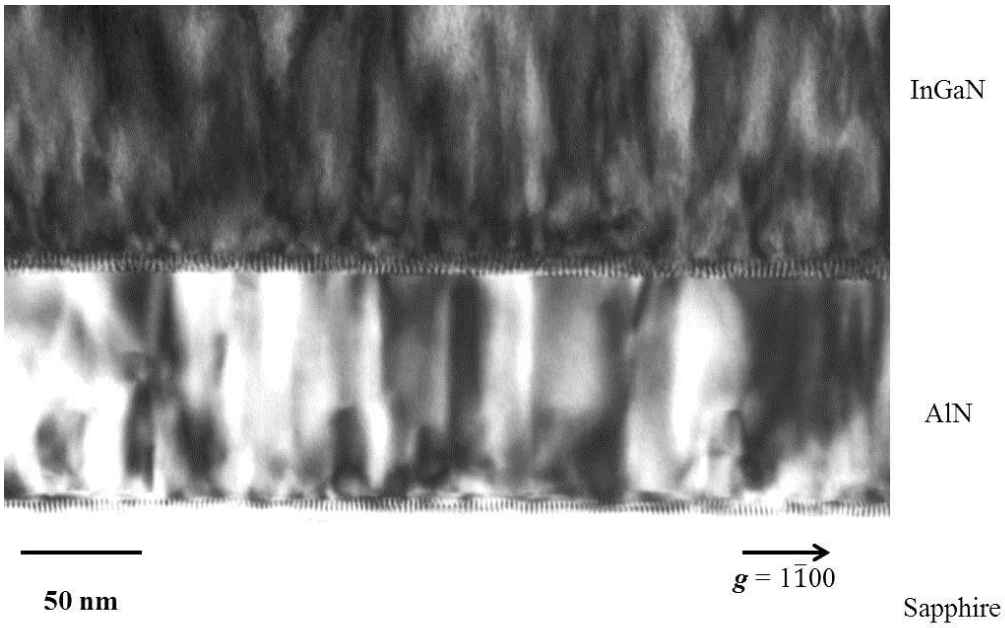

FIG. 5.6. Cross-section bright-field TEM image of InN film with $g = 1\bar{1}00$. Periodic moiré fringes is observed at InGaN/AlN interface.

The polarity of InGaN epilayer with x = 0.78 are studied by using annular bright-field (ABF) image and convergent beam electron diffraction (CBED). ABF image and

CBED was operated at a region near the surface. ABF image shows that nitrogen column is on top of gallium column at each bilayer, indicating the InGaN epilayer near surface are N-polairty. Figure 5.7(b) shows the experimental CBED pattern. The simulated CBED pattern with a film thickness about 40 nm in Fig. 5.7(c) agrees well with the experimental CBED pattern, indicating the InGaN epilayer is N-polarity. Both ABF and CBED indicates InGaN is N-polarity at a near surface region.

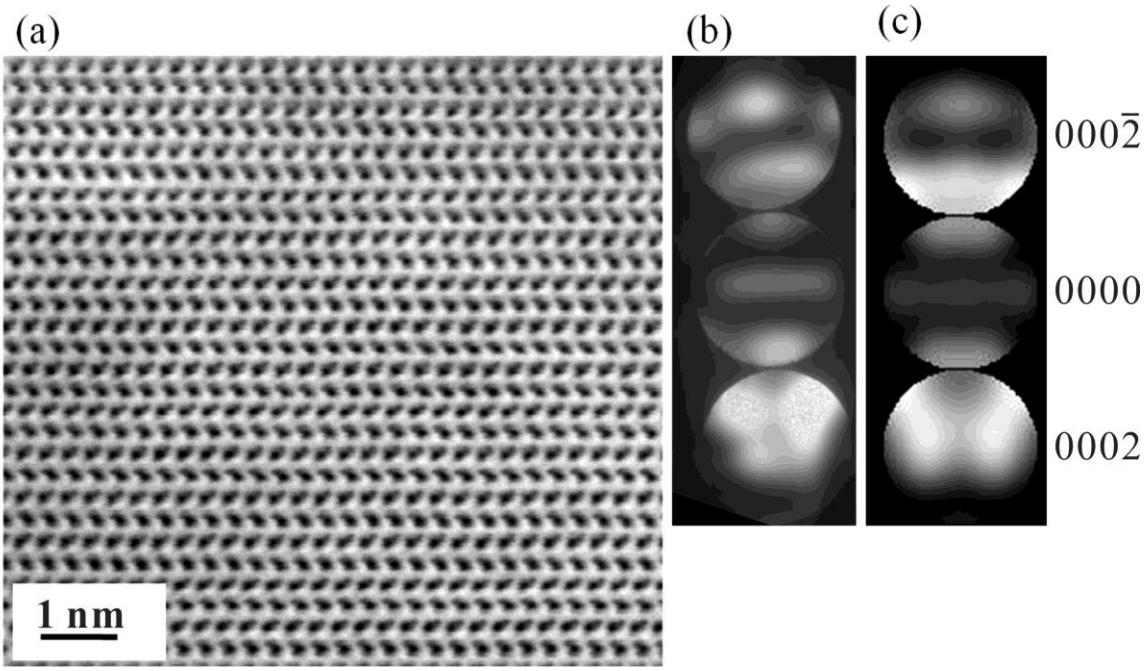

FIG. 5.7. (a) Annular bright-field image of InGaN epilayer near surface. CBED were taken near the surface region. (b) Experimental CBED disks. (c) Simulated CBED disks with 40 nm thickness.

5.6. Microstructure of InGaN Epilayer with [In] ~ 60%

The structural properties of InGaN epilayer with [In] ~ 60% are analyzed in detail in this section since it represents a general case of high-indium-content InGaN structure

grown by ENABLE. The bright-field images of a cross-sectional TEM sample recorded for two-beam conditions with different ***g*** vectors are shown in Fig. 5.8. Figure 5.8(a) is an image with the ***g***-vector 0002 close to the $< 1\bar{1}00 >$ projection. On the other hand, figure 5.8(b) is an image with the ***g***-vector $11\bar{2}0$ close to the $< 1\bar{1}00 >$ projection. Screw-type threading dislocations with Burgers vector ***a*** are only visible in Fig. 5.8(a) based on ***g.b*** analysis. They originate from the interface of the AlN buffer layer and InGaN epitaxial film. Most of the screw-type dislocations bend or terminate by forming dislocation loops during growth. We do not observe any screw-type threading dislocations in the AlN buffer, indicating that the AlN buffer only has twist behavior. It is interesting to notice that those dislocations threading through the epitaxial layer will form a V-shape opening at the InGaN surface. The angle between the V-shape facets and the (0001) growth plane are about 16^{o}, which correspond to the projection of $\{1\bar{1}03\}$ planes. The undulated surface crests are separated by ~120 nm.

Dislocations with an edge-component are visible in Fig. 5.8(b). It is clear that edge-type threading dislocations are dominant in both the InGaN epilayer and AlN buffer layer. The epilayer shows alternating dark and bright contrast. The contrast will change from dark to bright and bright to dark when applying a slight sample tilt along the ***c*** axis. It indicates that there exist crystal domains with slight rotation along the ***c***-axis. Edge-type dislocations are formed at those grain boundaries.

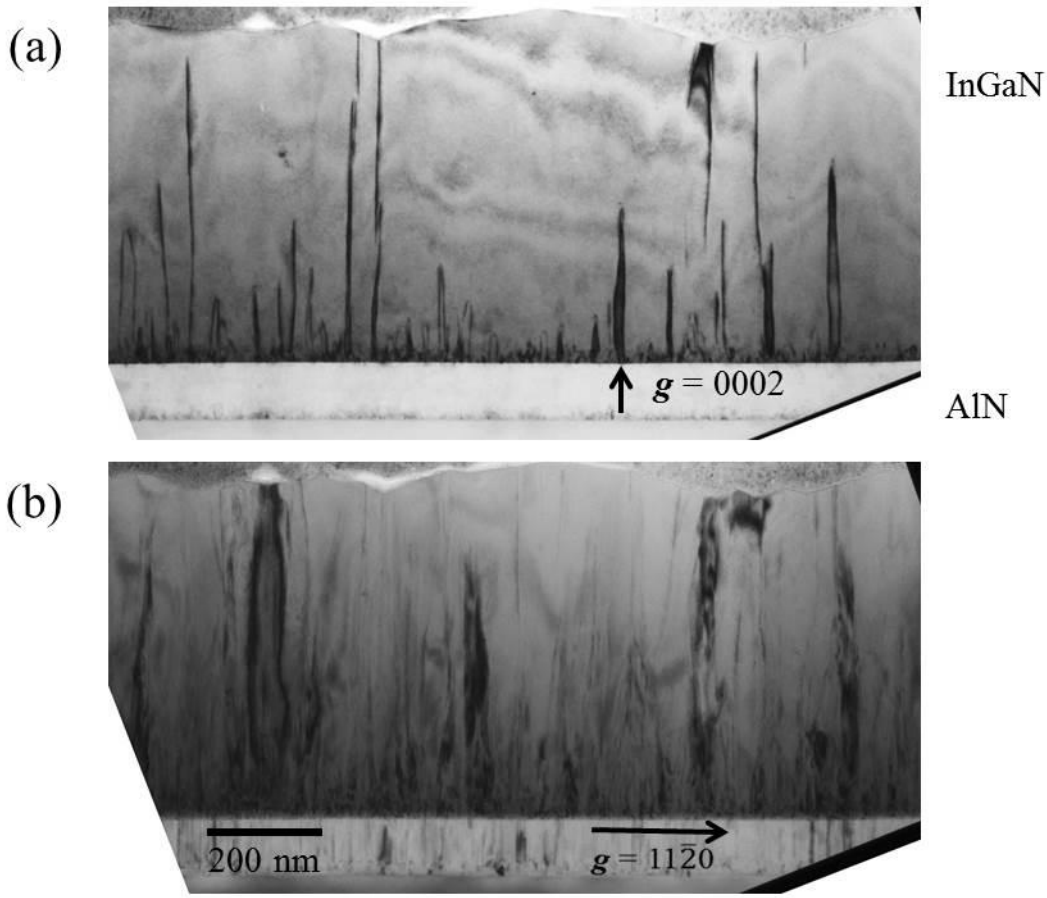

FIG. 5.8. Cross-section bright-field TEM image of $In_{0.6}Ga_{0.4}N$ epilayers with (a) $\boldsymbol{g}$ = 0002, (b) $\boldsymbol{g} = 11\bar{2}0$.

Figure 5.9(a) is a SAED pattern and cross-section TEM image taken at the InGaN/AlN interface along the $< 11\bar{2}0 >$ projection. Two sets of diffraction patterns for InGaN (inner set) and AlN (outer set) are clearly observed. A blue dotted line in Fig. 5.9(a) drawn from the $(1\bar{1}04)$ to $(\bar{1}104)$ AlN spots passing through the origin shows that the equivalent InGaN diffracton spots fall on the same straight line, indicating that the InGaN epilayer is significantly relaxed. In order to study the strain relaxation mechanism at the interface, cross-section TEM image are tilted along the $(1\bar{1}00)$ direction about 5 degrees, producing an overlap between the InGaN and AlN planes. Due to the difference

in InGaN and AlN interplanar spacing, periodic moiré fringes with a separation of 3.18 ± 0.02 nm are generated at the InGaN and AlN heterointerface. The moiré fringe separation corresponds to an indium composition of x = 0.60 ± 0.01. Similarly, strain relaxation by introduction of misfit dislocations at the interface is also evidenced by SAED and cross-section TEM image along $< 1\bar{1}00 >$ projection in Fig. 5.9(b). The cross-section image are tilted about 7 degrees along $(11\bar{2}0)$ direction. Moiré fringe separation is 1.84 ± 0.01 nm, corresponding to x = 0.60 ± 0.01. The moiré fringes corresponding to $\{11\bar{2}0\}$ planes and $\{1\bar{1}00\}$ are consistent with each other, indicating misfit relaxation occurs along the full 2-dimenisonal interfaces.

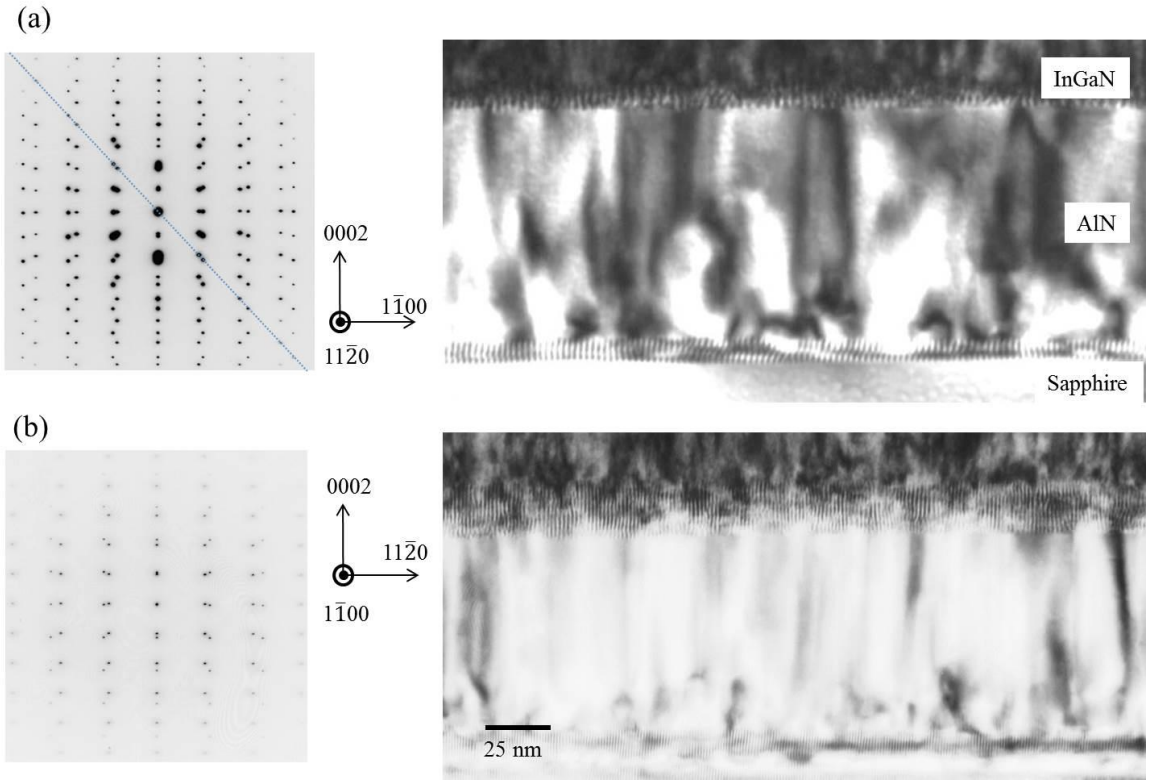

FIG. 5.9. Selected-area diffraction patterns and cross-section dark-field TEM images of the $In_{0.6}Ga_{0.4}N$/AlN/sapphire region, taken along the (a) $< 11\bar{2}0 >$ and (b) $< 1\bar{1}00 >$

projections. Misfit strain relaxation is evidenced by the diffraction patterns and the periodic moiré fringes at the interface.

Figure 5.10 shows a high-resolution HAADF image at the InGaN/AlN interface. The AlN buffer layer appears much darker than the $In_{0.6}Ga_{0.4}N$ epilayer due to its smaller atomic number. The interface is smooth with only about one atomic layer roughness. A smooth AlN surface could help to a subsequent high quality InGaN film growth.

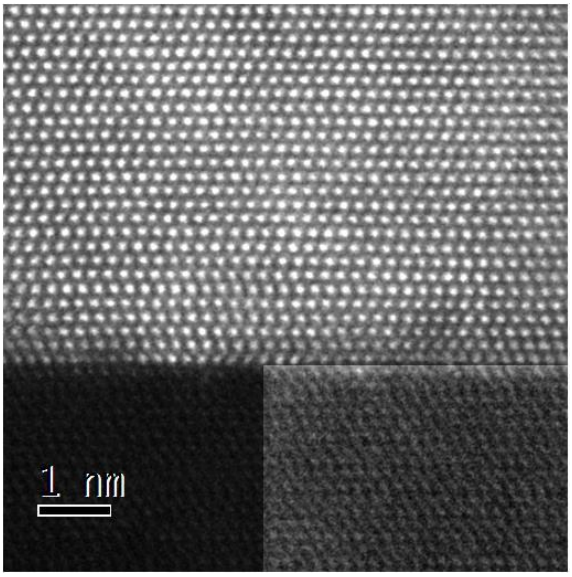

FIG. 5.10. High-resolution HAADF image of $In_{0.6}Ga_{0.4}N$/AlN interface at $< 11\bar{2}0 >$ projection with the intensity of bottom right AlN underlayer enhanced. The interface is smooth with about one atomic layer roughness.

Some research efforts have confirmed that InGaN alloys with high indium content tends to phase separate with compositional fluctuations ($\Delta x \sim 0.1$). [7] Local chemical composition fluctuation can be distinguished by HAADF images in the form of contrast

variations. Figure 5.11(b) is a high-resolution HAADF images from the box region of Fig. 5.11(a). The overall contrast is uniform with no clear evidence of periodic contrast variations of the InGaN epilayer, indicating absence of phase separation. The contrast variation at a lower magnification in Fig 5. 11(a) could due to different crystal domains with a slight rotation along *c* direction.

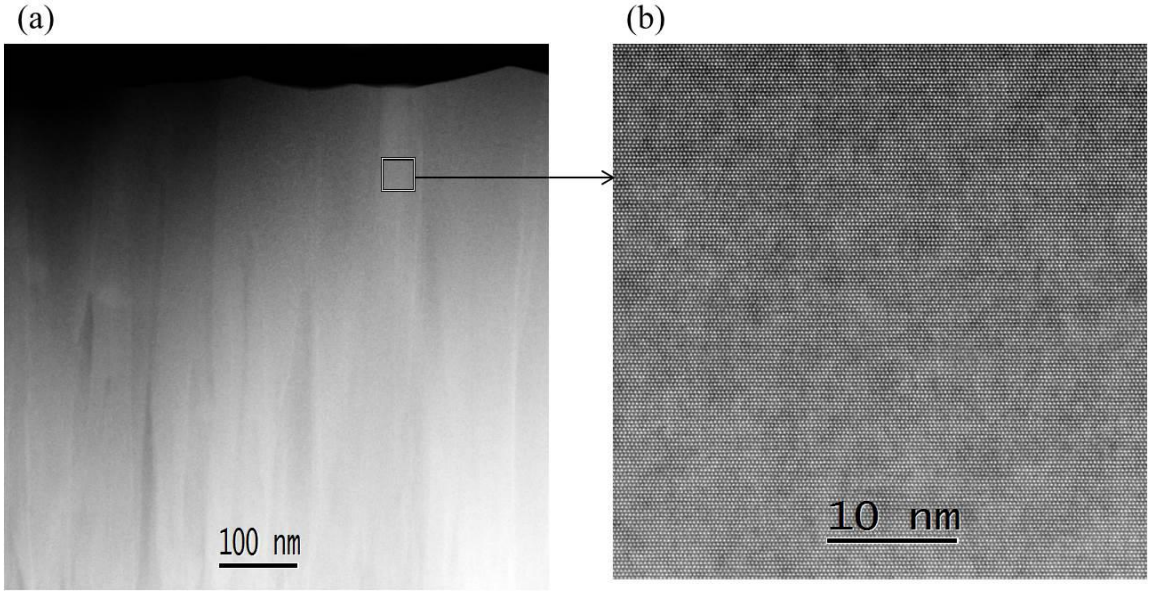

FIG. 5.11. HAADF image of thick InGaN layer at (a) lower magnification and at (b) higher magnification of the selected squared region.

5.7. Microstructure of InGaN Epilayer with [In] ~ 54%

As we observed in chapter 4, InGaN films are partially relaxed on GaN buffer when indium composition is below 60%. We next try to analyze the transition point at which InGaN films is partially relaxed.

Figure 5.12 shows (a) the SAED pattern and (b) BF image taken at the $In_{0.54}Ga_{0.46}N$/AlN interface. Evidence of moiré fringes is observed in Fig 5.2(b) as periodic

contrast at the InN/AlN interface, indicating an abrupt change in the in-plane lattice parameter. The moiré fringe separation is 3.52 $\pm$ 0.04 nm which corresponds to x = 0.52 $\pm$ 0.02. For x = 0.54, misfit strain is almost completely relaxed by misfit dislocations at interface. The overall structure of InGaN epilayer is shown in Fig. 5.13, Very few screw-type threading dislocations are observed in cross-section TEM image. A few horizontal lines are observed in the InGaN epilayer. They could be related to indium accumulation at the growth front.

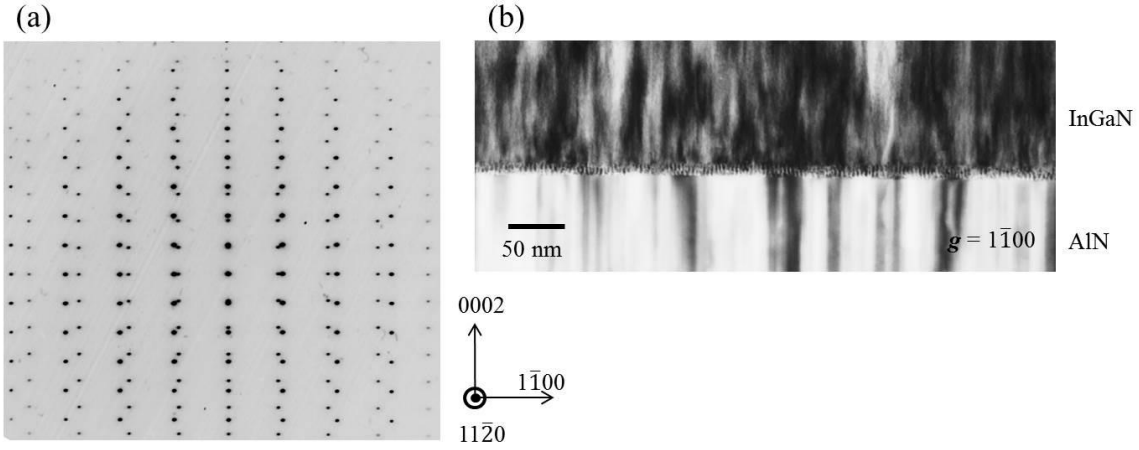

FIG. 5.12. (a) Selected-area electron diffraction pattern along the $< 11\bar{2}0 >$ projection, from an area across the interface between the AlN underlayer and the InGaN film. (b) Cross-section bright-field TEM image of InGaN film with $g = 1\bar{1}00$.

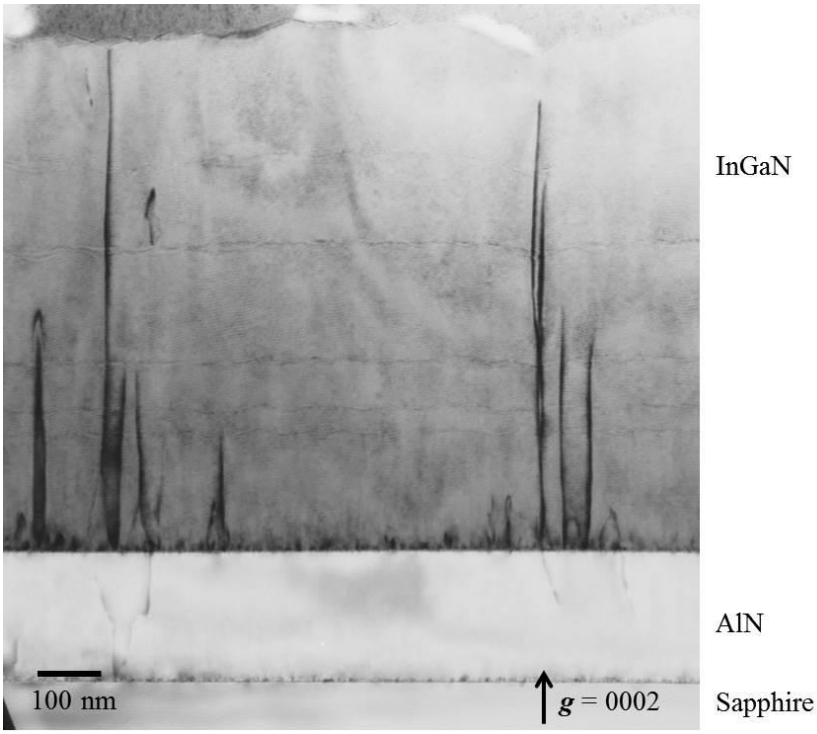

FIG. 5.13. Cross-section bright-field TEM image of InGaN film with $\boldsymbol{g} = 1\bar{1}00$ shows overall structure of InGaN film. Horizontal striations may be due to indium segregated layers.

5.8. Microstructure of InGaN Epilayer with [In] ~ 48%

When the indium composition comes to 48%, moiré fringes are still observable at the InGaN/AlN interface as shown in Fig. 5.14. The average moiré fringe separation is about 5.0 ± 0.2 nm. However, the expected misfit dislocation separation is 3.69 nm for a fully relaxed state, so 74% of misfit strain is relaxed at InGaN/AlN interface. Cross-section bright-field TEM image in Fig. 5.15 shows that the InGaN epilayer is highly defected.

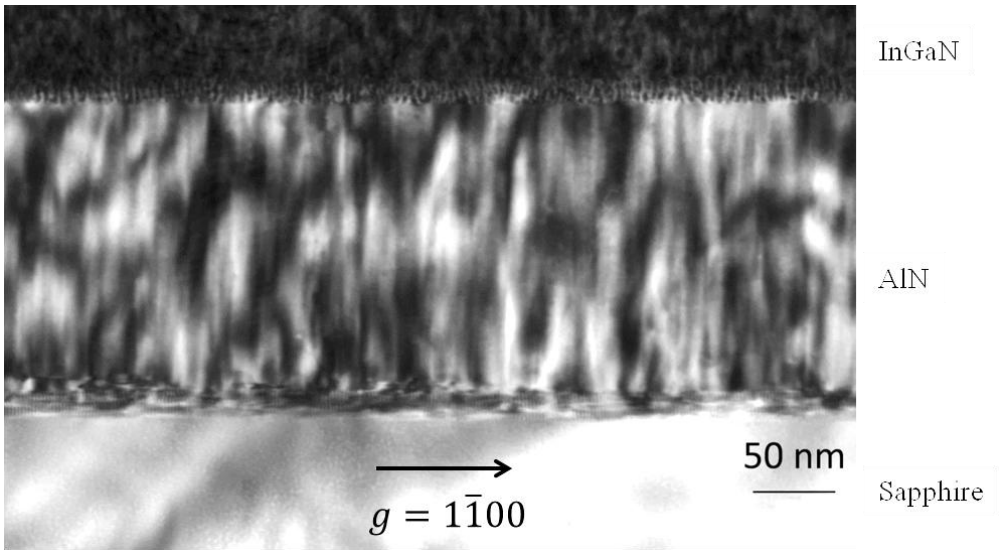

FIG. 5.14. Cross-section bright-field TEM image of InGaN film with $\boldsymbol{g} = 1\bar{1}00$.

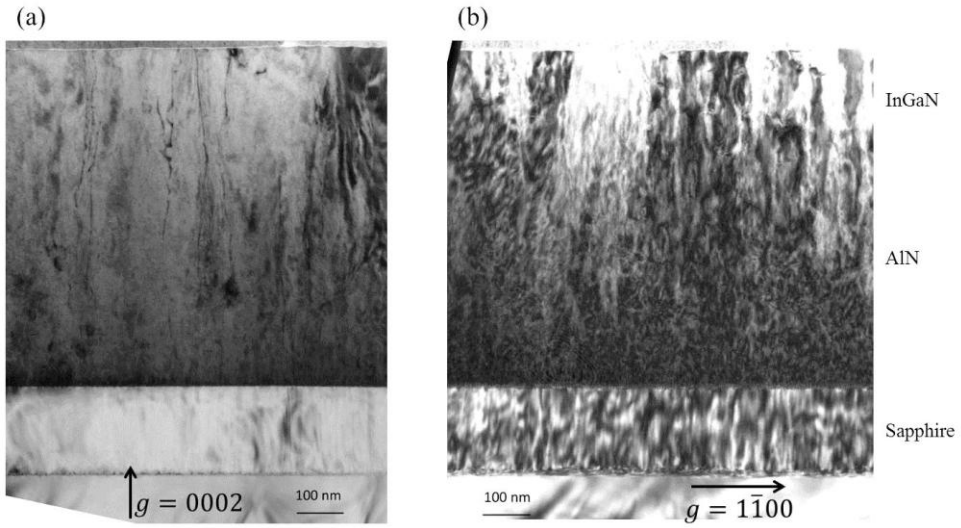

FIG. 5.15. Cross-section TEM bright-field image of InGaN epilayers with (a) $\boldsymbol{g}$ = 0002, (b) $\boldsymbol{g}$ = $1\bar{1}00$. High density of defects is observed in the epilayer.

5.9. Discussion

In Chapter 4, we have shown that the InGaN quality can be improved by lattice-mismatch strain relaxation at the InGaN/GaN interface via the generation of misfit dislocations after a critical thickness is achieved.[11] We have proposed that the epilayer spontaneously nucleates in a fully relaxed state with a periodic network of misfit dislocations when the critical thickness is close to a monolayer. For the $In_xGa_{1-x}N$/GaN system, partial and full misfit strain relaxation was observed for x = 0.60 and x = 0.67, respectively. The same relaxation mechanism was observed in the InGaN/AlN systems. Table 5.1 summarizes theoretical and experimental values of misfit dislocation separation at the $In_xGa_{1-x}N$/AlN interface for x = 0.48, 0.54, 0.60, 0.78, 0.84, and 1.0. We observed a full misfit strain relaxation at the In_xGa_{1-x} N/AlN interfaces for x = 0.54, 0.60, 0.78, and 1.0. For x = 0.84, indium accumulates at InGaN/AlN interface. Partial strain relaxation was observed for x = 0.48. Figure 5.16 shows critical thickness for the InGaN/AlN system based on different models. Critical thickness curves are extrapolated by straight dotted lines for high indium composition. Lattice mismatch between InGaN/AlN is larger than the InGaN/GaN system for the same indium composition. This larger lattice mismatch will result in a smaller critical thickness for the same indium composition and hence full misfit strain relaxation could happen at a lower indium composition. This explains why we observed near-complete misfit strain relaxation happening at lower indium compositions ($x \sim 0.54$) in the InGaN/AlN system. The critical thickness of about one lattice parameter c happens when $x \sim 0.45$. The near-complete misfit strain relaxation happens at $x \sim 0.50$. The concept of critical thickness about one lattice parameter c is approximately consistent with experimental observations.

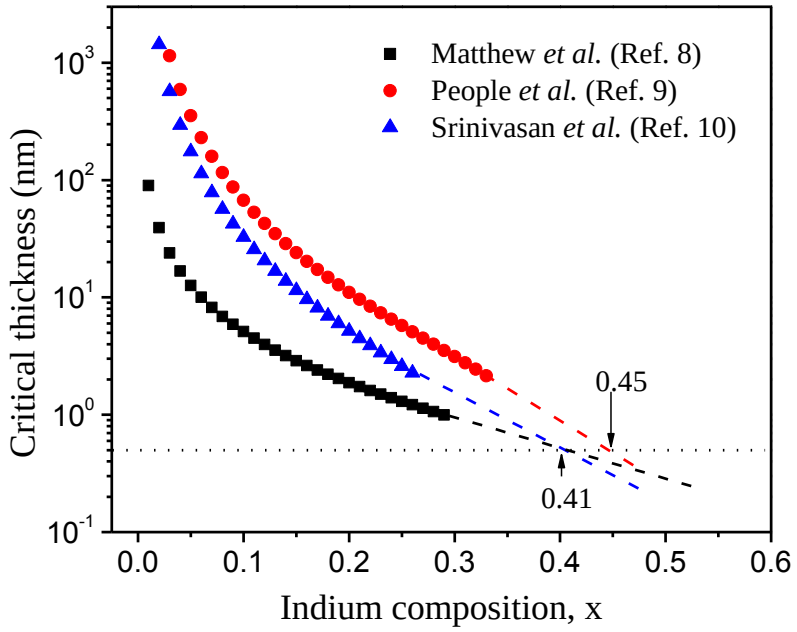

FIG. 5.16. Critical thickness vs. indium content *x* for the $In_xGa_{1-x}N$/AlN system using three different models. The critical thickness of one lattice period *c* (horizontal dotted line) happens at $x = 0.45$.

Table 5.1. Theoretical and experimental values of misfit dislocation separation at the $In_xGa_{1-x}N$/AlN interface for various indium contents.

Indium composition (x)	$D_{experimental}$ (nm)	$D_{expected}$ (nm)	% of relaxation
1.0	1.30 ± 0.02	1.29	99%
0.84	NA	2.53	NA
0.78	2.74 ± 0.02	2.66	97%

0.60	3.18 ± 0.02	3.18	100%
0.54	3.52 ± 0.04	3.42	97%
0.48	5.00 ± 0.20	3.7	75%

Note: Misfit dislocation separations for x = 1.0 are based on $\{11\bar{2}0\}$ lattice planes. All other misfit dislocation separations are based on $\{1\bar{1}00\}$ lattice planes.

Photoluminescence measurements were performed at 10 K. The luminescence peak of the $In_xGa_{1-x}N$ films for x = 0.60, 0.78, 0.84, and 1.0 is centered at 930, 1160, 1320, and 1835 nm. No extra peaks are observed per film, indicating absence of phase separation.

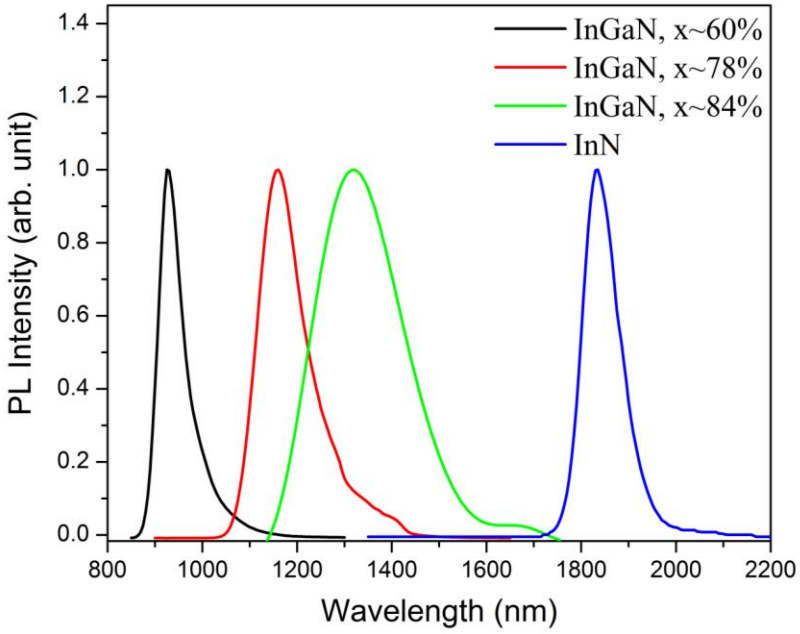

FIG. 5.17. Photoluminescene of InGaN with x = 0..60, 0.78, 0.84, and 0.10 at T = 10K.

5.10. Conclusions

The ENABLE technique was used to grow InGaN films with high indium content with indium composition ranging from 0.48 t0 1.0. This chapter reveals that ENABLE growth of InGaN films on a AlN buffer can enable a full misfit strain relaxation at lower indium compositions than InGaN films grown on GaN buffer. Near complete misfit strain relaxation happens at x = 0.54, 06.0, 0.78, and 1.0. We propose that the innovative growth method with low growth temperatures (500^{o}C), the high quality AlN buffer with flat surface, and critical thickness of epilayer less than one monolayer contribute to high quality InGaN film growth.

References

[1] O. Jani, I. Ferguson, C. Honsberg, and S. Kurtz, Appl. Phys. Lett. **91**, 132117 (2007).

[2] C. J. Neufeld, N. G. Toledo, S. C. Cruz, M. Iza, Steven P. DenBaars, and U. K.Mishra, Appl. Phys. Lett. **93**, 143502 (2008).

[3] R. Dahal, B. Pantha, J. Li, J. Y. Lin, and H. X. Jiang, Appl. Phys. Lett. **94**, 063505 (2009).

[4] V. Y. Davydov, A. A. Klochikhin, R. P. Seisyan, V. V. Emtsev, S. V. Ivanov, F. Bechstedt, J. Furthmuller, H. Harima, A. V. Mudryi, J. Aderhold, O. Semchinova, and J. Garul, Phys. Status Solidi **B 229**, 1 (2002).

[5] J. Wu, W. Walukiewicz, K. M. Yu, J. W. Ager III, E. E. Haller, H. Lu, W. J. Schaff, Y. Saito, and Y. Nanishi, Appl. Phys. Lett. **80**, 3967 (2002).

[6] T. Matsuoka, H. Okamoto, M. Nakao, H. Harima, and E. Kurimoto, Appl. Phys. Lett. **81**, 1246 (2002).

[7] Z. Liliental-Weber, D. N. Zakharov, K. M. Yu, J. W. Ager, W. Walukiewicz, E. E. Haller, H. Lu, W. J. Schaff, Journal of Electron Microscopy **54(3)**, 243 (2005).

[8] J. W. Matthews and A. E. Blakeslee, J. Cryst. Growth **27**, 118 (1974).

[9] R. People and J. C. Bean, Appl. Phys. Lett. **47**, 322 (1985).

[10] S. Srinivasan, L. Geng, R. Liu, F.A. Ponce, Y. Narukawa, and S. Tanaka, Appl. Phys. Lett. **83**, 5187 (2003).

[11] A. M. Fischer, Y. O. Wei, F. A. Ponce, M. Moseley, B. Gunning, and W. A. Doolittle, Appl. Phys. Lett. **103,** 131101 (2013).

CHAPTER 6

MICROSTRUCTURE OF DEEP UV AlGaN-BASED HETEROSTRUCTURES

This chapter presents the structural properties of AlGaN-based deep ultraviolet laser structures. It is found that defects in epitaxial layer are greatly reduced when the structure is deposited on a single crystal AlN substrate. Two trimethylgallium (TMG) sources in the growth of multiple quantum wells active region are of great help in improving the quality of quantum well and quantum barrier structures. These efforts contribute to realize lasing in the sub-300nm regime.*

(*) Parts of this chapter were published as:

1) Z. Locher, X. H. Li, T. T. Kao, M. M. Satter, H. J. Kim, S. C. Chen, P. D. Yoder, J. H. Ryou, R. D. Dupuis, K. Sun, Y. Wei, T. Li, A. M. Fischer, and F. A. Ponce, *Stimulated emission at 257 nm from optically-pumped AlGaN/AlN heterostructure on AlN sbustrate.* Physica. Status Solidi A **210**, 1768 (2013).

2) Z. Lochner, T. T. Kao, Y. S. Liu, X. H. Li, M. M. Satter, S. C. Shen, P. D. Yoder, J. H. Ryou, R. D. Dupuis, Y. Wei, H. Xie, A. M. Fischer, and F. A. Ponce, *Deep-ultraviolet lasing at 243 nm from photo-pumped AlGaN/AlN heterostructure on AlN substrate.* Applied Physics Letters **102**, 101110 (2013).

3) T. T. Kao, Y. S. Liu, M. M. Satter, X. H. Li, Z. Lochner, P. D. Yoder, T. Detchprohm, R. D. Dupuis, S. C. Shen, J. J. Ryou, A. M. Fischer, Y. Wei, H. Xie, and F. Ponce, *Sub-250 nm low-threshold deep-ultraviolet AlGaN-based heterostrucutre laser employing HfO_2/SiO_2 dielectric mirrors.* Applied Physics Letters **103**, 211103 (2013).

6.1. Introduction

As mentioned in previous chapters, the III-N materials have a wide energy band gap from 0.7 to 6.2 eV, which covers the full spectrum of photon emission wavelengths from the near-infrared to deep-ultraviolet (DUV). Today, III-nitride solid-state lighting is the viable technology for the future energy-efficient light sources. DUV optoelectronic devices emitting below 280 nm are of great potential in the application of water purification, bio-agent detection, and medical sterilization.[1,2,3] High-pressure mercury lamps, excimer laser sources, or a frequency-tripled infrared laser source are conventionally applied to achieve sub 280 nm wavelength. However, these sources have disadvantages such as low portability and presence of toxic materials. Thus, a portable and efficient semiconductor-based ultraviolet emitter is a desirable alternative. The UV emitter using a AlGaN alloy system can successfully achieve wavelength below 280nm.[4,5,6,7,8] However, low carrier concentrations, low injection efficiently, and high density of defects limit the performance characteristics of typical AlGaN-based optical devices. DUV laser structure epitaxially grown on foreign substrate generally faces the problem of high density of defects. These high density of defects working as carrier traps inhibits radiative recombination, thus lowering the output efficiency and increasing the power threshold for stimulated emission.[9]

Most III-nitride based devices are typically grown on non-native substrates such as sapphire or SiC. However, electrical injection UV-Laser Diodes (LD) are thus far limited to an emission wavelength of 336 nm due to limitations in effectively doping AlGaN with high aluminum content.[10] Optically pumped AlGaN multi-quantum well (MQW) structures have been reported for wavelengths as short as 241.5 nm on SiC,

however the threshold power density was relatively high.[11] This is due to lattice mismatch and thermal expansion coefficient difference between the AlGaN heteroepitaxially grown materials on SiC that results in strain relaxation, cracking, and defect formation.[12]

AlN has similar lattice constant with AlGaN, thus AlN substrates provide a possible solution for the problem of high density of defects. AlN substrates enable homoepitaxial growth of AlN buffer layers,[13] leading to a reduced threading dislocation density in the subsequent $Al_xGa_{1-x}N$ based MQW active region. The elimination of thermal mismatch between the substrate and epitaxial layers also enhances the growth and performance of the device by eliminating cracks that form during the thermal cycle and cool-down.

In this work, we perform a comprehensive study on the microstructure of AlGaN-based DUV heterostructure on different substrates including foreign substrates sapphire and single-crystal AlN substrates. We studied the effect of the use of AlN and sapphire substrates on the microstructure of heteroepitaxial films and optical properties. We also found that the quality of active region of DUV laser can be greatly improved by using two trimethylgallium (TMG) sources.

6.2. Microstructure of AlGaN/AlN Heterostructure on AlN Substrate with a Stimulated Emission at 257 nm

In this section, AlGaN/AlN based Laser Diodes (LD) structure grown on foreign sapphire substrate and single crystal AlN substrate are compared in order to investigate the effect of this factor on the microstructure and hence the LD performance. The LD

structures were grown by the group of Prof. Russell Dupuis at Georgia Institute of Technology by metal-organic chemical vapor deposition (MOCVD) at a temperature of 1155 ^{o}C on (1) sapphire and (2) AlN substrates. Figure 6.1(a) shows the schematic of the DUV laser structure. The device structure began with a 200-nm-thick AlN buffer layer, followed by 25 periods of AlN/$Al_{0.66}Ga_{0.34}N$ (2 nm/2 nm) superlattice buffer and 25 periods of $Al_{0.66}Ga_{0.34}N/Al_{0.55}Ga_{0.45}N$ (2 nm/2 nm) superlattice buffer. Then, a Si-doped *n*-type region, a three-period $Al_{0.66}Ga_{0.34}N/Al_{0.53}Ga_{0.47}N$ (5 nm/2.8 nm) MQW region, and finally a Mg doped *p*-type region were grown to complete the laser structure. A detailed layer structure is described in Fig. 6.2 and the function of each layer can be found somewhere else.[14]

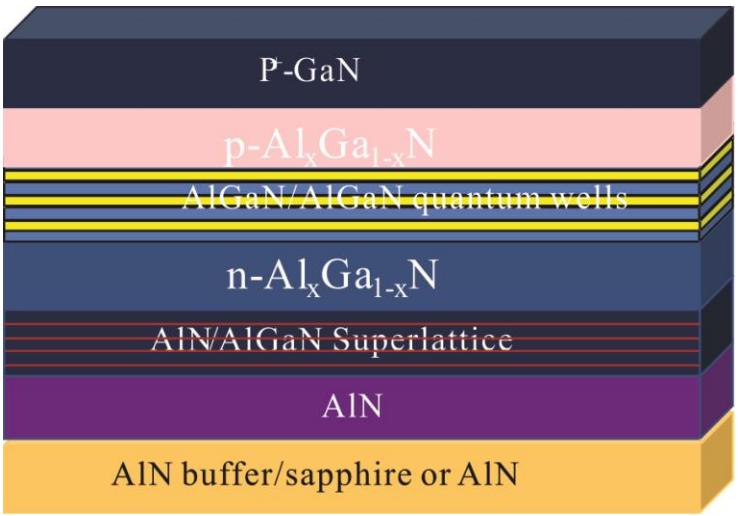

FIG. 6.1. Schematic diagram of DUV laser structure including *p*-barrier, MQWS active region, *n*-barrier, and AlN buffer layer on sapphire or AlN substrate.

Full DUV laser structure

125nm 0.65 -> 0.55 $Al_xGa_{1-x}N$:Mg graded layer
120nm 0.55 $A_xlGa_{1-x}N$:Mg current spreading layer
35nm 0.68 -> 0.66 $Al_xGa_{1-x}N$:Mg EBL
12nm 0.66 $Al_xGa_{1-x}N$:Mg Spacer layer
25nm $Al_{0.66}Ga_{0.34}N/Al_{0.53}Ga_{0.47}N$ MQW (5/2.8 nm*3)
430nm 0.66->0.80 $Al_xGa_{1-x}N$:Si graded layer
330nm 0.80->0.55 $Al_xGa_{1-x}N$:Si graded layer
30nm 0.55 $Al_xGa_{1-x}N$:Si buffer layer
600nm 0.55 $Al_xGa_{1-x}N$ Si+ contact layer
100nm $Al_{0.66}Ga_{0.34}N/Al_{0.55}Ga0_{.45}N$ superlattice buffer (2/2nm *25)
100nm $AlN/Al_{0.66}Ga_{0.34}N$ superlattice buffer (2/2nm *25)
200nm AlN regrowth

900nm AlN template/Sapphire OR HT 319

FIG. 6.2. DUV laser structure showing layer thickness, composition, and doping type.

6.2.1. Microstructure Characterization of UV Laser Devices

TEM sample was prepared by standard mechanical wedge polishing and argon ion milling techniques. TEM was carried out on a JEOL 4000EX microscope with a 400 kV accelerating voltage. Figure 6.3 shows cross-section bright-field (BF) TEM images taken at $\boldsymbol{g}$ = 0002 for UV laser on (a) single crystal AlN substrate and (b) AlN buffer/Sapphire substrate. The heteroepitaxial layers on single crystal AlN are almost free of threading dislocations. On the contrary, the structure on sapphire substrates exhibits high density of threading dislocations. Even though a thick AlN template (~900 nm), a AlN buffer (~ 200nm), and superlattice buffer are applied to reduce threading dislocation density in the following layers and threading dislocation densities are greatly reduced by AlN buffer layer and superlattice, as shown in Fig. 6.3(b), threading dislocation with a density ~2 × 10^9 cm^{-2} can still threading through the whole epitaxial layer. X-ray

diffraction (XRD) asymmetric (105) reciprocal space mapping (RSM), shown in Fig. 6.4, was taken by high-resolution triple-axis X-ray diffractometer of the structure on AlN substrate. The axes Q_x and Q_y in Fig. 6.4 represent the reciprocal lattice constant *a* and *c*. RSM shows that the AlN substrate, supperlattice, graded layer, and contact layer have the same Q_x value, indicating that these layers are pseudomorphically grown on AlN substrate. The crystal similarities between the epilayers and the AlN substrate is reflected in the reduced crystal defect densities. This reduced dislocation density due to the single crystal AlN substrate is crucial to enabling $\lambda < 300$nm stimulated emission.[14]

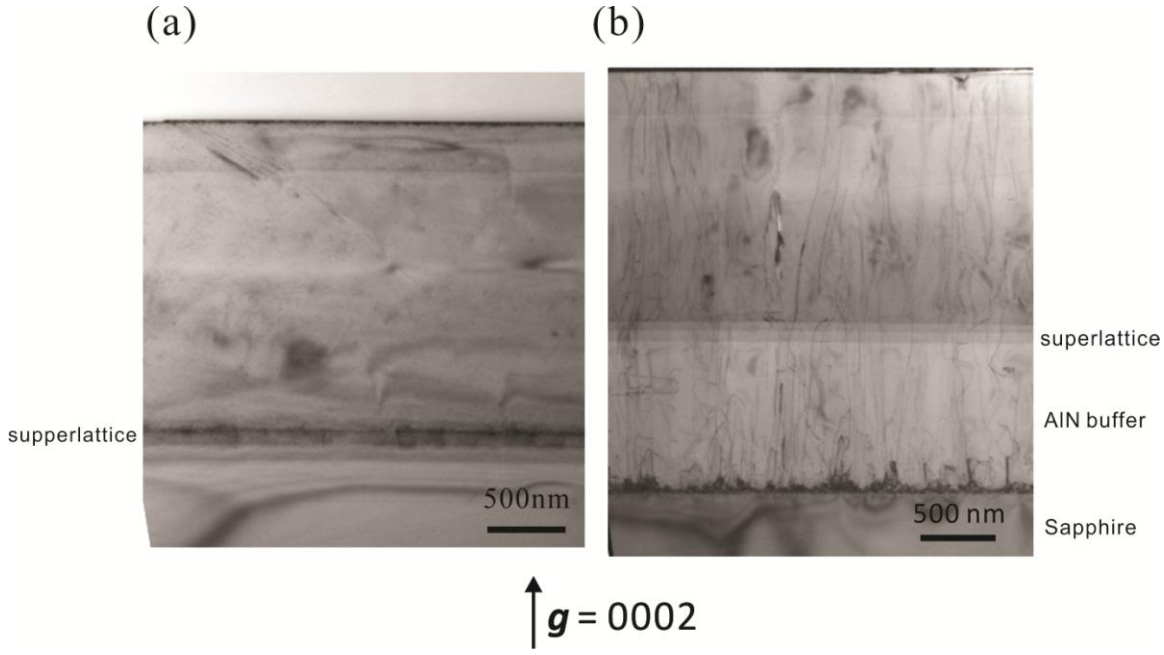

FIG. 6.3. Cross-section TEM BF image of identical device structures on (a) a single crystal AlN substrate and (b) AlN buffer/sapphire substrate.

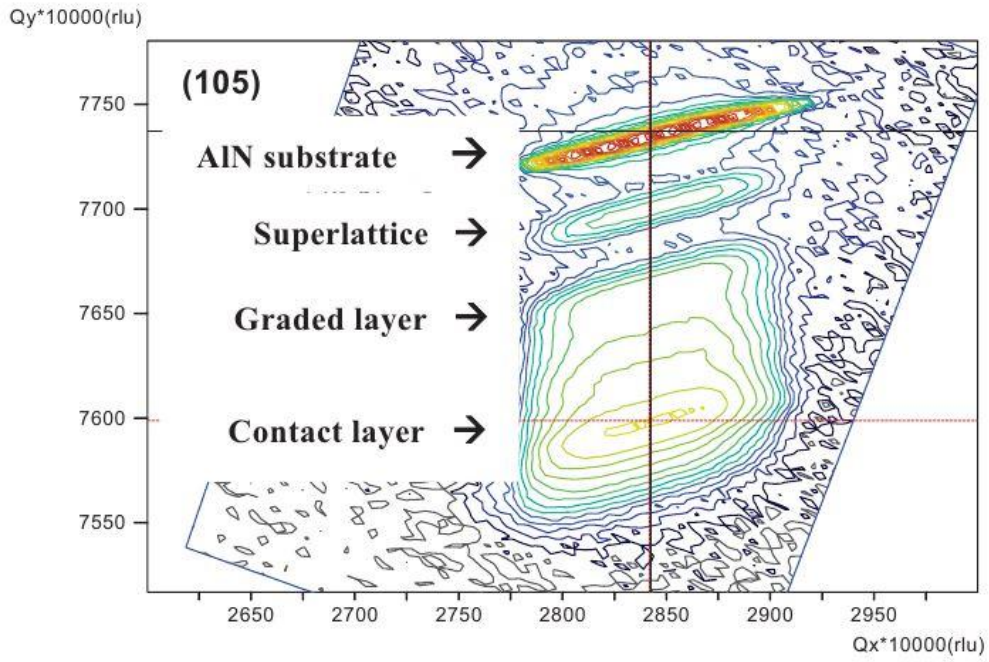

FIG. 6.4. X-ray diffraction RSM of the epitaxial structure grown on single crystal AlN substrate. [14]

Monochromatic cathodoluminescence (CL) images (acquired at the peak emission wavelength) were taken by Dr. Reid Juday at room temperatures in a scanning electron microscope to study the effect of different substrates on optical properties. The spatial variation of light emission was probed by CL imaging in a scanning electron microscope. The DUV laser device on single crystal AlN (Fig. 6.5(a)) exhibits uniform spatial luminescence over all of the film. A dark band in the image represents an artificial scratch on the film surface used as reference. On the contrary, the emission of laser grown on conventional sapphire (Fig. 6.5(b)) exhibits inhomogeneous spatial distribution, due to the high density of threading dislocations acting as non-radiative recombination centers.

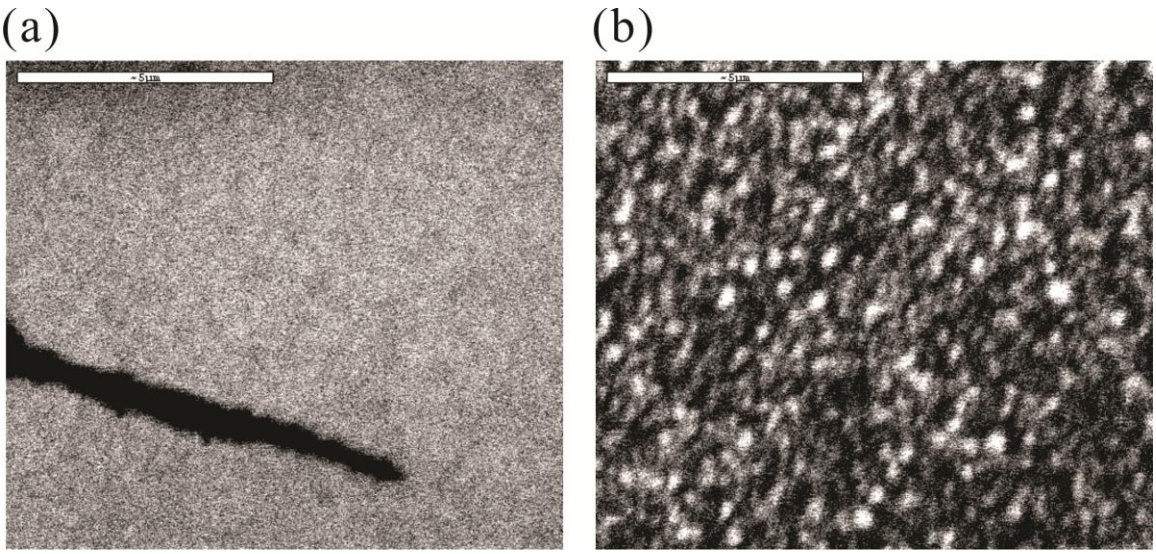

FIG. 6.5. Monochromatic CL images for DUV laser on (a) AlN substrate and (b) sapphire substrate. Uniform light emission was observed for DUV laser on single crystal AlN substrate.

6.3. The Effect of Different Number of TMG Sources on the Active Region of Sub 300 nm DUV Lasers

Quantum wells are used to confine the electron-hole pairs and thus increase the quantum efficiency. However, growth of MQWs with good quality is challenging. In this section, we have compared sub-300-nm UV lasers with MQWs grown using one and two TMG sources. Figure 6.6 is a schematic diagram showing the configuration of the use of one-TMG and two-TMG sources during growth. In the one-TMG configuration in Fig 6.6(a), the quantum wells (QW) and the quantum barriers (QB) are grown using the same TMG source. The switch between QW and QB growth conditions requires a change of the TMG flow rate, which involves a pause of ~ 10 s in the growth. In the two-TMG

configuration, one of the TMG sources is set for growth of the QWs and the other is set to for the QBs, as shown in Fig 6.6(b). The growth switch between QW and QB is instantaneous. The lasers were grown by MOCVD at 1155^{o}C by Prof. Russell Dupuis at Georgia Institute of Technology. The chemical composition of the quantum wells and the quantum barriers are designed to be $Al_{0.6}Ga_{0.4}N$ and $Al_{0.75}Ga_{0.25}N$. Their structures were studied by scanning transmission electron microscope (STEM) and their optical properties by CL in the SEM.

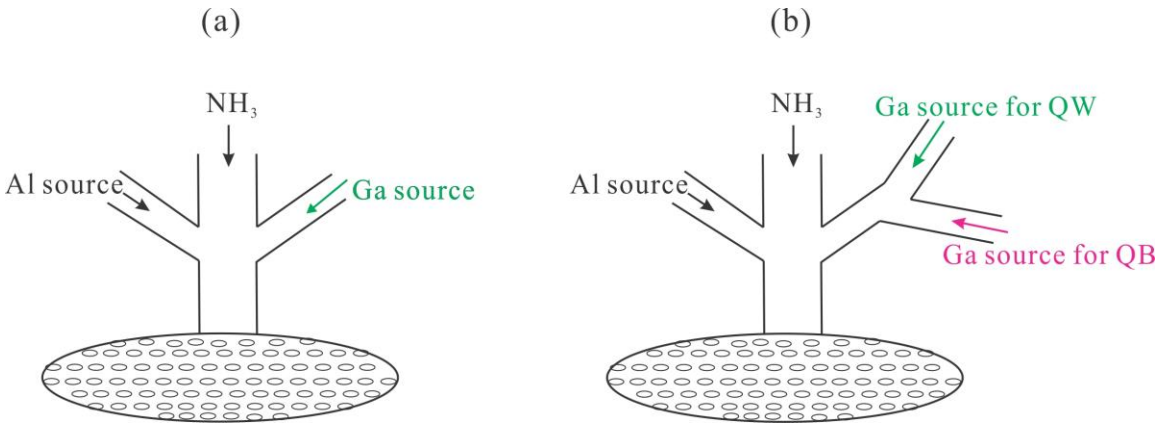

FIG. 6.6. Sechmatic diagram showing the configuration of (a) the one-TMG growth method and (b) the two-TMG growth method.

6.3.1. Microstructure on the Active Region of DUV Lasers Grown by One and Two TMG Sources

STEM is used to study the structure of the MQWS. The contrast in the high-angle annular dark-field (HAADF) mode is proportional to Z^n, where n=1.7-2. [15] For example, a Ga-rich quantum well looks brighter than Al-rich quantum barriers in HAADF images, which enables us to clearly visualize the MQW structure. Figure 6.7(a) shows a HAADF image of MQWs on an AlN substrate using one-TMG growth method.

Nine periods of QWs are observed. Dark layers are observed at each interface between a QW and a QB. QWs have similar brightness as QBs. Figure 6.7(b) shows the structure at a higher magnification. We can observe 3 atomic layers for each dark layer which corresponds to a thickness ~0.75 nm. The QW and QB have a thickness of 2.3 and 4 nm, respectively.

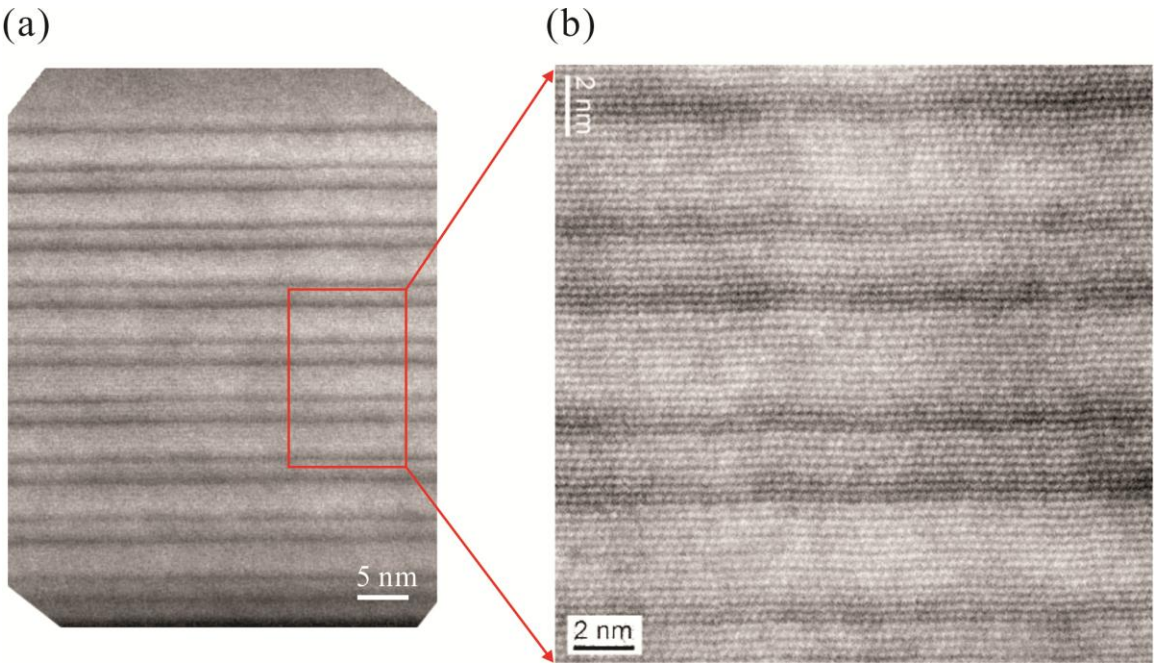

FIG. 6.7. (a) HAADF image of MQWs grown by one TMG source. (b) Higher magnification of rectangular region in (a) shows the atomic arrangement of QWs.

Figure 6.8 shows a HAADF image of MQWs on single crystal AlN substrate grown using two-TMG growth method. There are no dark layers at the interfaces and the contrast between QW and QB is much more clearly compared with the MQWS grown by one TMG source. Figure 6.9 shows a intensity profile of QWs. The QW and QB have a thickness of 3 and 5 nm, respectively.

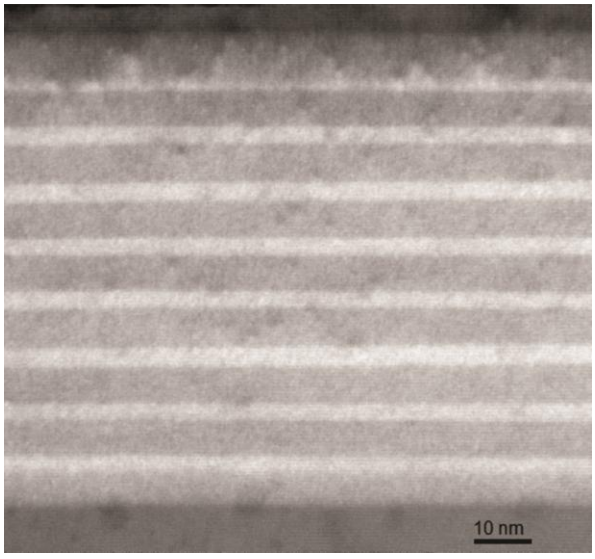

FIG. 6.8. HAADF image of MQWS grown by two TMG sources.

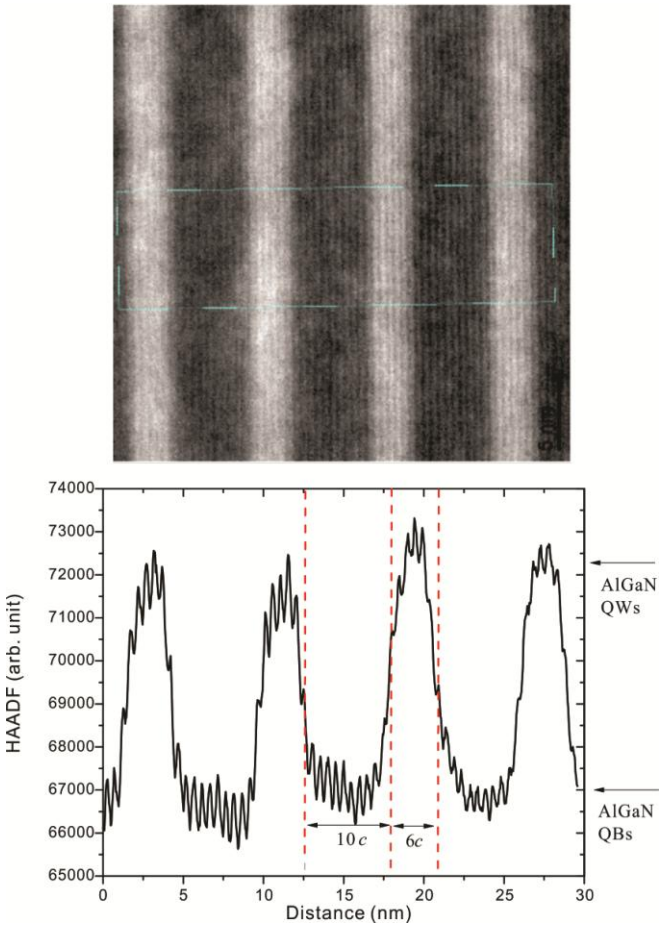

FIG. 6.9. Intensity profile of across four QWs. Contrast for each QW and QB is uniform.

In MOCVD at high temperature (>1100C), both growth and desorption processes coexist. In the one-TMG configuration, the growth switch between QW and QB requires a change in the TMG flow rate. During the change/ramp (of about 10 seconds), there is no Ga injected onto the wafer surface. Thus, the desorption process dominates and takes away some Ga in the AlGaN layer, leaving an Al-rich layer, as shown in Fig 6.10. Al is more resistant to thermal desorption because of the stronger Al-N covalent bond. In the two-TMG configuration, the growth switch from QW to QB is instantaneous, leaving no chance for the Ga desorption and the appearance of an Al-rich layer.

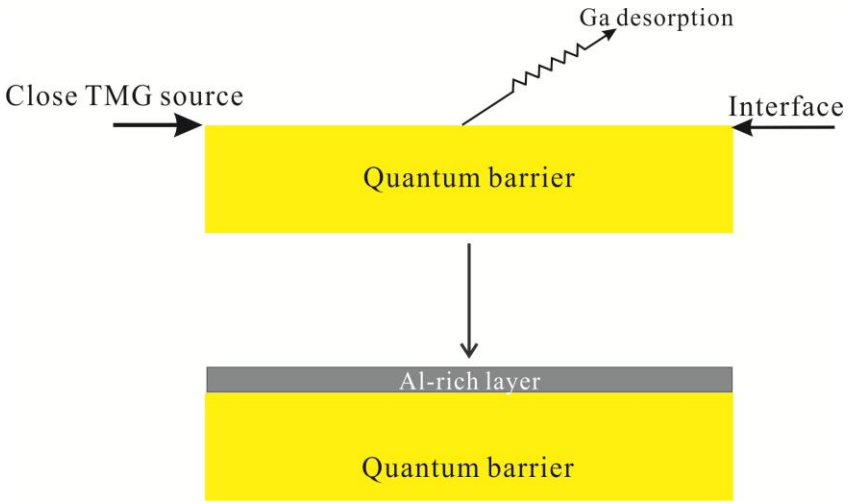

FIG. 6.10 Schematic diagram illustrating the formation of an Al-rich layer at the QB/QW interface due to TMG close time in the one-TMG growth method.

6.3.2. Optical Properties of DUV Lasers Grown by One and Two TMG Sources

CL spectra are recorded in a modified scanning electron microscope. Electrons are injected the top surface exciting valence band electrons to the conduction band. Excited electrons then fall back to the valence band emitting photons. The energy of

photons is equal to the energy difference between the initial and final states of the electrons. By studying the photon spectrum, information about energy band gaps, excitons, transition rates, etc. can be obtained.[16] CL spectra were taken by Dr. Alec Fischer.

Figure 6.11 shows the CL spectra of two samples, taken with the same excitation power. The sample grown using two-TMG method shows a higher efficiency than the one grown by 1 TMG source by a factor of 7. A peak shift is observed from 263 nm (4.71 eV) to 257 nm (4.82 eV).

In the sample grown using one-TMG method, the Al atoms mostly gather at the interfaces (the dark layers in Fig. 6.7), which lead to an ineffective quantum confinement as the width of the barrier is actually smaller than designed. This explains low efficiency of the using one-TMG method. The QW in this sample have a lower Ga content than 40% (less contrast in Fig. 6.7), which together with the Al-rich dark layers raises the ground state in the QW. This causes the emission peak to shift to higher energies.

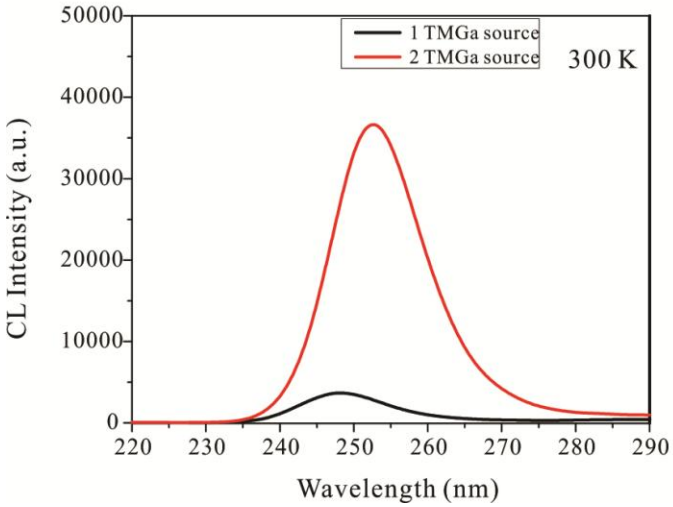

FIG. 6.11. CL spectra on MQWs using one-TMG growth method (lower emission) and two-TMG growth method (higher emission).

6.4. Conclusions

In summary, a comparative study has been performed to optimize the UV laser structure with modifying parameters such as substrate materials and different number of TMGa sources. The AlGaN based heterostructure grown on an (0001) single crystal AlN structure enables homoepitaxy AlN buffer layer. The subsequent DUV laser structure is fully strained on AlN and dislocation density is greatly reduced. MQWs grown by using one-TMG method faces the problem of Al accumulation at QW/QB interface. MQWs grown by two-TMG method have much better structure of QW and QB. CL spectra show that MQWs grown by two-TMG method have much higher emission efficiency than MQWs grown by one-TMG method. We propose that DUV laser structure grown on single crystal AlN substrate along with two-TMG method could help to achieve DUV lasing. AlGaN-based DUV laser structures lasing at sub 300 nm are reported for a few different wavelengths.[14,17,18]

References

[1] T. Cutler and J. Zimmerman, Anim. Health Res. Rev. **12**, 15 (2011).

[2] H. H. Chun, J. Y. Kim, and K. B. Song, Food Sci. Biotechnol. **19**, 547 (2010).

[3] K. Baxter, M. Castle, S. Barrington, P. Withers, V. Foot, A. Pickering, and N. Felton, Proc. Of SPIE **6739**, 67390Z (2007).

[4] J. R. Grandusky, S. R. Gibb, M. C. Mendrick, C. Moe, M. Wraback, and L. J. Schowalter, Appl. Phys. Express **4**, 082101 (2011).

[5] M. S. Shur and R. Gaska, IEEE Trans. Electron Devices **57**, 12 (2010).

[6] H. Hirayama, Y. Tsukada, T. Maeda, and N. Kamata, Appl. Phys. Express **3**, 031002 (2010).

[7] V. Adivarahan, A. Heidari, B. Zhang, Q. Fareed, S. Hwang, M. Islam, and A. Khan, Appl. Phys. Express **2**, 102101 (2009).

[8] A. Yasan, R. McClintock, K. Myes, D. Shiell, L. Gautero, S. Darvish, P. Kung, and M. Razeghi, Appl. Phys. Lett. **83**, 4701 (2003).

[9] J. Mickevičius, J. Jurkevičius, K. Kazlauskas, A. Žukauskas, G. Tamulaitis, M. S. Shur, M. Shatalov, J. Yang, and R. Gaska, Appl. Phys. Lett. **100**, 081902 (2012).

[10] H. Yoshida, Y. Yamashita, M. Kuwabara, and H. Kan, Appl. Phys. Lett. **93**, 241106 (2008).

[11] T. Takano, Y. Narita, A. Horiuchi, and H. Kawanishi, Appl. Phys. Lett. **84**, 3567 (2004).

[12] K. Ban, J. Yamamoto, K. Takeda, K. Ide, M. Iwaya, T. Takeuchi, S. Kamiyama, I. Akasaki, and H. Amano, Appl. Phys. Express **4**, 052101 (2011).

[13] A. Rice, R. Collazo, J. Tweedie, R. Dalmau, S. Mita, J. Xie, and Z. Sitar, J. Appl. Phys. **108**, 043510 (2010).

[14] Z. Locher, X. H. Li, T. T. Kao, M. M. Satter, H. J. Kim, S. C. Chen, P. D. Yoder, J. H. Ryou, R. D. Dupuis, K. Sun, Y. Wei, T. Li, A. M. Fischer, and F. A. Ponce, Phys. Status Solidi A **210**, 1768 (2013).

[15] P. Nellist, S. Pennycook, Adv. Imaging Electron Phys. **113**, 147 (2000).

[16] B. G. Yacobi, D. B. Holt, J. Appl. Physics. **59**, R1 (1986).

[17] Z. Lochner, T. T. Kao, Y. S. Liu, X. H. Li, M. M. Satter, S. C. Shen, P. D. Yoder, J. H. Ryou, R. D. Dupuis, Y. Wei, H. Xie, A. M. Fischer, and F. A. Ponce, Appl. Phys. Lett. **102**, 101110 (2013).

[18] T. T. Kao, Y. S. Liu, M. M. Satter, X. H. Li, Z. Lochner, P. D. Yoder, T. Detchprohm, R. D. Dupuis, S. C. Shen, J. J. Ryou, A. M. Fischer, Y. Wei, H. Xie, and F. Ponce, Appl. Phys. Lett. **103**, 211103 (2013).

CHAPTER 7

SUMMARY AND FUTURE WORK

7.1. Summary

In this dissertation, several fundamental material issues of III-nitride semiconductors have been investigated by means of physical characterization from a microscopic point of view. Firstly, the strain relaxation mechanism in InGaN/GaN heterostructures grown by MME and in InGaN/AlN heterostructures grown by ENABLE has been investigated. Secondly, the influence of different substrates and number of TMG sources on the optical and structural properties has been clarified.

In Chapter 4, the microstructure evolution of $In_xGa_{1-x}N$ films with indium composition x in the range from 0.22 to 0.67 was studied. The films were grown by metal-modulated epitaxy at low temperatures (~ 400 ℃) to facilitate indium incorporation, and with precursor modulation to enhance surface morphology and metal adlayer diffusion. A high density of crystalline defects, consisting mainly of stacking faults associated with island growth, is observed in the lower range (x = 0.22). The microstructure evolves into fine columnar domains devoided of stacking faults in the mid-range (x = 0.46). A significant improvement in the crystalline quality and optical properties is observed for $x \geq 0.60$, with strain relaxation at the interface evidenced by the presence of moiré fringes. High luminescence intensity, low defect density, and a near complete misfit strain relaxation are observed for x = 0.67. The efficient misfit strain relaxation can be explained by a critical thickness value of the order of a monolayer. This behavior is reproducible in variations of the growth technique, and provides an approach for growth under high lattice mismatch conditions.

In Chapter 5, ENABLE-MBE growth of high-indium-content InGaN thick films on AlN buffer/sapphire substrate were analyzed for developing new technologies for InGaN based solar cells. Transmission electron microscopy and photoluminescence were used to study $In_xGa_{1-x}N$ thick films with x = 0.48, 0.54, 0.60, 0.78, 0.84 and 1.0. $In_xGa_{1-x}N$ films with $x > 0.54$ have near-complete misfit strain relaxation at the interface. For $x = 0.84$, indium clusters are observed at interface. Partial misfit strain relaxation is observed at $x = 0.48$. The introduction of a high quality AlN buffer is observed to produce high quality, fully relaxed thick InGaN films in the range of $0.54 < x < 1$. Growth of InGaN films by the innovative ENABLE technique, produces high quality AlN buffer layers and a critical thickness below one lattice parameter c which contribute to the growth of high quality thick InGaN films.

In Chapter 6, the effect of different substrates and number of TMGa sources on the microstructure of AlGaN-based deep ultraviolet laser was studied. It is found that defects in epitaxial layer are greatly reduced when the structure is deposited on a single crystal AlN substrate. Two TMGa sources used for the growth of multiple quantum wells active region are of great help in improving the quality of quantum well and quantum barrier structures. These efforts contribute to the realization of lasing at a sub-300-nm regime.

7.2. Future Work

Former group members have done a detailed study of strain relaxation mechanisms of $In_xGa_{1-x}N$ with lower indium composition ($x < 0.16$) alloys grown by MOCVD. In this dissertation, we observed that the fully misfit strain relaxation by misfit dislocation at the interface of $In_xGa_{1-x}N$ with higher indium composition ($x > 0.48$) by modified MBE

growth technique. This suggests we can use the MOCVD growth for low indium-composition InGaN film growth and MBE growth of fully strain relaxed InGaN film with higher indium composition. Due to the larger lattice mismatch between InGaN and AlN, we can achieve fully relaxation $In_xGa_{1-x}N$ with $x > 0.48$, while the fully relaxed $In_xGa_{1-x}N$ on GaN buffer happens at $x > 0.60$, so we can consider to grow high-indium-content InGaN on AlN buffer. We can also consider growing high-indium-content InGaN films on single crystal AlN substrates to further improve InGaN film quality. We have done PL study for InGaN alloys with wide range of indium composition. The PL emission peaks can be used to estimate InGaN bandgaps. For ternary alloys, a bowing parameter is used to approximately describe their bandgaps:

$$E_g(In_xGa_{1-x}N) = x\,E_g(InN) + (1-x)E_g(GaN) - bx(1-x) \qquad (7.1)$$

It would be interesting to investigate the bowing parameter for InGaN alloy system based on PL emission peaks.

The second research topic is to improve the critical thickness models for InGaN/GaN. It should be noted that several assumptions and approximations are made in critical thickness calculations, not only in the mathematical methods used but also in the values of the materials parameters. The latter, such as the Poisson's ratio and shear modulus are not well known. The critical thickness calculation for $x > 0.40$ is unavailable due absence of solutions in the transcendental equation used in these models. These works could help to get better understanding of strain relaxation mechanism of InGaN on different underlayers and hence realize high quality InGaN over the entire indium composition range.

REFERENCES

A. Kazimirov, G. Scherb, J. Zegenhagen, T. L. Lee, M. J. Bedzyk, M. K. Kelly, H. Angerer, and O. Ambacher, Appl. Phys. Lett. **84**, 1703 (1998).

A. M. Andrews, J. S. Speck, A. E. Romanov, M. Bobeth, and W. Pompe, J. Appl. Phys **91**, 1933 (2002).

A. M. Fischer, Ph.D. Dissertation, Arizona State University, 8-13 (2009).

A. M. Fischer, Y. O. Wei, F. A. Ponce, M. Moseley, B. Gunning, and W. A. Doolittle, Appl. Phys. Lett. **103,** 131101 (2013).

A. R. Acharya. Ph. D. dissertation: Indium Nitride Surface Structure, Desorption Kinetics and Thermal Stability (Georgia State University, 2013).

A. Rice, R. Collazo, J. Tweedie, R. Dalmau, S. Mita, J. Xie, and Z. Sitar, J. Appl. Phys. **108**, 043510 (2010).

A. Y. Cho, Surf. Sci. **17**, 494 (1969).

A. Yasan, R. McClintock, K. Myes, D. Shiell, L. Gautero, S. Darvish, P. Kung, and M. Razeghi, Appl. Phys. Lett. **83**, 4701 (2003).

B. Williams, and C. B. Carter, Transmission Electron Microscopy, (Springer, 1996), chapter 38, p. 655-663.

C. A. M. Fabien, M. Mosely, B. Gunning, W. A. Doolittle, A. M. Fischer, Y. O. Wei, and F. A. Ponce, IEEE Journal of Photovoltaics, **4**, 601 (2014).

C. J. Neufeld, N. G. Toledo, S. C. Cruz, M. Iza, S. P. DenBaars, and U. K. Mishra, Appl. Phys. Lett. **93**, 143502 (2008).

D. Chandrasekhar, D. J. Smith, S. Strite, M. E. Lin, and H. Morkoc, J. Crystal Growth. **152**, 135 (1995).

D. Chidambarrao, G. R. Srinivasan, B. Cunningham, and C. S. Murthy, Appl. Phys. Lett. **57**, 1001 (1990).

E. Okunishi, H. Sawada, and Y. Kondo, Micron **43**, 538-544 (2012).

F. A. Ponce and D. P. Bour, Nature (London) **386**, 351 (1997).

F. A. Ponce, MRS Bull. **22**, 51 (1997).

F. A. Ponce, D. P. Bour, W. T. Young, M. Saunders, and J. W. Steeds, Appl. Phys. Lett. **69**, 337 (1996).

F. A. Ponce, in *Introduction to Nitride Semiconductor Blue Lasers and Light Emitting Diodes*, edited by S. Nakamura and S. F. Chichibu, Taylor and Francis Ltd, London, Chapter 4 (2000).

F. A. Ponce, S. Srinivasan, A. Bell, L. Geng, R. Liu, M. Stevens, J. Cai, H. Omiya, H. Marui, and S. Tanaka, Phys. Stat. Sol. A **240**, 273 (2003).

F. Bernardini, V. Fiorentini, D. Vanderbilt, Phys. Rev. B 56, R10024 (1997).

F. C. Frank, Acta Cryst. **18**, 862, 1965.

G. Yacobi, D. B. Holt, J. Appl. Physics. **59**, R1 (1986).

H. Amano, N. Sawaki, I. Akasaki, and Y. Toyoda, Appl. Phys. Lett. **48**, 353 (1986).

H. H. Chun, J. Y. Kim, and K. B. Song, Food Sci. Biotechnol. **19**, 547 (2010).

H. Hamzaoui, A. S. Bouazzi, and B. Rezig, Solar Energy Materials & Solar Cells **87**, 595 (2005).

H. Hirayama, Y. Tsukada, T. Maeda, and N. Kamata, Appl. Phys. Express **3**, 031002 (2010).

H. Yoshida, Y. Yamashita, M. Kuwabara, and H. Kan, Appl. Phys. Lett. **93**, 241106 (2008).

I. Ho and G. B. Stringfellow, Appl. Phys. Lett. **69**, 2701 (1996).

I. Vurgaftman, J. R. Meyer, J. Appl. Phys. **94**, 3675 (2003).

J. Mickevičius, J. Jurkevičius, K. Kazlauskas, A. Žukauskas, G. Tamulaitis, M. S. Shur, M. Shatalov, J. Yang, and R. Gaska, Appl. Phys. Lett. **100**, 081902 (2012).

J. R. Grandusky, S. R. Gibb, M. C. Mendrick, C. Moe, M. Wraback, and L. J. Schowalter, Appl. Phys. Express **4**, 082101 (2011).

J. W. Matthews and A. E. Blakeslee, J. Cryst. Growth **27**, 118 (1974).

J. Wu, W. Walukiewicz, K. M. Yu, J. W. Ager III, E. E. Haller, H. Lu, W. J. Schaff, Y. Saito, and Y. Nanishi, Appl. Phys. Lett. **80**, 3967 (2002).

K. Ban, J. Yamamoto, K. Takeda, K. Ide, M. Iwaya, T. Takeuchi, S. Kamiyama, I. Akasaki, and H. Amano, Appl. Phys. Express **4**, 052101 (2011).

K. Baxter, M. Castle, S. Barrington, P. Withers, V. Foot, A. Pickering, and N. Felton, Proc. Of SPIE **6739**, 67390Z (2007).

L. Liu and J. H. Edgar, Materials Science and Engineering **R37**, 61 (2002).

M. Moseley, B. Gunning, J. Greenlee, J. Lowder, G. Namkoong, and W. A. Doolittle, J. Appl. Phys. **112**, 014909 (2012).

M. P. Maruska and J. J. Tietjen, Appl. Phys. Lett. **15**, 327 (1969).

M. S. Shur and R. Gaska, IEEE Trans. Electron Devices **57**, 12 (2010).

O. Ambacher, J. Phys. D: Appl. Phys. **31**, 2653 (1998).

O. Ambacher, M. S. Brandt, R. Dimitrov, T. Metzger, M. Stutzmann, R. A. Fischer, A. Miehr, A. Bergmaier, and G. Dollinger, J. Vac. Sci. Technol. B **14**, 3532 (1996).

O. Jani, I. Ferguson, C. Honsberg, and S. Kurtz, Appl. Phys. Lett. **91**, 132117 (2007).

P. D. Nellist, Scanning Transmission Electron Microscopy: Imaging and Analysis, (Chapter 2, Springer, 2011), chapter 2, p. 91-116.

P. Hartel, H. Rose, and C. Dinges, Ultramicroscopy **63**, 93 (1996).

P. Nellist, S. Pennycook, Adv. Imaging Electron Phys. **113**, 147 (2000).

R. Dahal, B. Pantha, J. Li, J. Y. Lin, and H. X. Jiang, Appl. Phys. Lett. **94**, 063505 (2009).

R. Ishikawa, E. Okunishi, H. Sawada, Y. Kondo, F. Hosokawa, and E. Abe, Nature Matierials **10**, 278 (2011).

R. Liu, A. Bell, F. A. Ponce, C. Q. Chen, J. W. Yang, and M. A. Khan, Appl. Phys. Lett. **86**, 021908 (2005).

R. Liu, J. Mei, S. Srinivasan, F. A. Ponce, H. Omiya, Y. Narukawa, and T. Mukai, Appl. Phys. Lett. **89**, 201911 (2006).

R. Liu, J. Mei, S. Srinivasan, H. Omiya, F. A. Ponce, D. Cherns, Y. Narukawa, and T. Mukai. Jpn. J. Appl. Phys. **45**, L549 (2006).

R. People and J. C. Bean, Appl. Phys. Lett. **47**, 322 (1985).

S. Srinivasan, L. Geng, R. Liu, F.A. Ponce, Y. Narukawa, and S. Tanaka, Appl. Phys. Lett. **83**, 5187 (2003).

T. Cutler and J. Zimmerman, Anim. Health Res. Rev. **12**, 15 (2011).

T. L. Williamson, J. J. Williams, J. C. D. Hubbard, and M. A. Hoffbauer, J. Vac. Sci. Technol. B, **29**, 03C132 (2011).

T. Matsuoka, H. Okamoto, M. Nakao, H. Harima, and E. Kurimoto, Appl. Phys. Lett. **81**, 1246 (2002).

T. T. Kao, Y. S. Liu, M. M. Satter, X. H. Li, Z. Lochner, P. D. Yoder, T. Detchprohm, R. D. Dupuis, S. C. Shen, J. J. Ryou, A. M. Fischer, Y. Wei, H. Xie, and F. Ponce, Appl. Phys. Lett. **103**, 211103 (2013).

T. Takano, Y. Narita, A. Horiuchi, and H. Kawanishi, Appl. Phys. Lett. **84**, 3567 (2004).

V. Adivarahan, A. Heidari, B. Zhang, Q. Fareed, S. Hwang, M. Islam, and A. Khan, Appl. Phys. Express **2**, 102101 (2009).

V. Adivarahan, A. Heidari, B. Zhang, Q. Fareed, S. Hwang, M. Islam, and A. Khan, Appl. Phys. Express **2**, 102101 (2009).

V. Crewe, and J. Wall, J. Mol. Biol. **48**, 375 (1970).

V. Y. Davydov, A. A. Klochikhin, R. P. Seisyan, V. V. Emtsev, S. V. Ivanov, F. Bechstedt, J. Furthmuller, H. Harima, A. V. Mudryi, J. Aderhold, O. Semchinova, and J. Garul, Phys. Status Solidi **B 229**, 1 (2002).

Z. H. Wu, K. Nonaka, Y. Kawai, T. Asai, F. A. Ponce, C. Q. Chen, M. Iwaya, S. Kamiyama, H. Amano, and I. Akasaki, Appl. Phys. Express **3**, 111003 (2010).

Z. Liliental-Weber, D. N. Zakharov, K. M. Yu, J. W. Ager, W. Walukiewicz, E. E. Haller, H. Lu, W. J. Schaff, Journal of Electron Microscopy **54(3)**, 243 (2005).

Z. Lochner, T. T. Kao, Y. S. Liu, X. H. Li, M. M. Satter, S. C. Shen, P. D. Yoder, J. H. Ryou, R. D. Dupuis, Y. Wei, H. Xie, A. M. Fischer, and F. A. Ponce, Appl. Phys. Lett. **102**, 101110 (2013).

APPENDIX A

LIST OF PUBLICATIONS DURING THE STUDY TOWARDS THE DOCTORAL DEGREE

Publications resulted from my work at ASU are listed below:

[1] **Y. O. Wei**, J. J. Williams, T. L. Williamson, A. M. Fischer, N. N. Faleev, F. A. Ponce, *Growth of high-quality high-indium-content InGaN layers by modified molecular beam epitaxy*. In preparation.

[2] **Y. O. Wei**, A. M. Fischer, F. A. Ponce, M. Moseley, B. Gunning, and W. A. Doolittle, *Microstructure of $In_xGa_{1-x}N$ (x = 0.2 to 0.67) by metal-modulated epitaxy*. Submitted on Nov 6th, 2014.

[3] W. Doolittle, C. A. M. Fabien; B. P. Gunning; A. M. Fischer, **Y. O, Wei**; H. Xie; F. A. Ponce, *Low-Temperature Growth of InGaN Films over the Entire Composition Range by MBE*. Submitted on Nov, 2014.

[4] X. H. Li, T. T. Kao, M. Satter, **Y. O. Wei**, S. Wang, H. Xie, S. C. Shen, P. Yoder, A. Fischer, F. Ponce, T. Detchprohm, and R. Dupuis, *Demonstration of transverse-magnetic dominant deep-ultraviolet stimulated emission from AlGaN multiple-quantum-well lasers on sapphire substrates*, submitted on Oct, 2014

[5] X.-H. Li, T. Detchprohm, Y.-S. Liu, T.-T. Kao, M. M. Satter, S.-C. Shen, P. D. Yoder, R. D. Dupuis, S. Wang, **Y. O. Wei**, H. Xie, A. M. Fischer, F. A. Ponce, T. Wernicke, C. Reich, M. Martens, and M. Kneissl. *Low-threshold stimulated emission at 249 nm and 256 nm from AlGaN-based multiple-quantum-well lasers grown on sapphire substrate.* Applied Physics Letters, **105**, 141106 (2014).

[6] C. A. M. Fabien, M. Moseley, B. Gunning, W. A. Doolittle, A. M. Fischer, **Y. O. Wei**, and F. A. Ponce. *Simulations, practical limitations, and novel growth technology for InGaN-based solar cells.* IEEE Journal of Photovoltaics, March 2014, Vol. **4**, pp. 601-606. DOI: 10.1109/JPHOTOV.2013.2292748.

[7] J. J. Williams, T. L. Williamson, M. A. Hoffbauer, **Y. Wei**, N. N. Faleev, and C. Honsberg. *Growth of high crystal quality InN by ENABLE-MBE*. Physica Status Solidi (c), **11**, 577 (2014).

[8] T.-T. Kao, Y.-S. Liu, M. M. Satter, X.-H. Li, Z. Lochner, P. D. Yoder, T. Detchprohm, R. D. Dupuis, S.-C. Shen, J.-H. Ryou, A. M. Fischer, **Y. O. Wei**, H. Xie, and F. A. Ponce. *Sub-250 nm, low-threshold deep-ultraviolet AlGaN-based heterostructure laser employing HfO2/SiO2 dielectric mirrors*. Applied Physics Letters, 18 November 2013, Vol. **103**, 211103. DOI: 10.1063/1.4829477.

[9] A. M. Fischer, **Y. O. Wei**, F. A. Ponce, M. Moseley, B. Gunning, and W. A. Doolittle. *Highly luminescent, high-indium-content InGaN film with uniform composition and full misfit-strain relaxation.* Applied Physics Letters, 24 September 2013. Vol. **103**, 131101. DOI: 10.1063/1.4822122.

[10] Z. Lochner, X.-H. Li, T.-T. Kao, M. M. Satter, H. J. Kim, S.-C. Shen, P. D. Yoder, J.-H. Ryou, R. D. Dupuis, K. W. Sun, **Y. O. Wei**, T. Li, A. M. Fischer, and F. A. Ponce. *Stimulated emission at 257 nm from an optically-pumped AlGaN/AlN heterostructure on AlN substrate.* Physica Status Solidi A, 9 September 2013. Vol. **210**, pp 1768-1770. DOI: 10.1002/pssa.201329013.

[11] Z. Lochner, T.-T. Kao, Y.-S. Liu, X.-H. Li, M. M. Satter, S.-C. Shen, P. D. Yoder, J.-H. Ryou, R. D. Dupuis, **Y. O. Wei**, H. Xie, A. M. Fischer, and F. A. Ponce. *Room-temperature optically pumped AlGaN-AlN multiple-quantum –well lasers operating at < 260 nm grown by metalorganic chemical vapor deposition.* Proceedings of SPIE, 11 April 2013, Vol. **8625**, 862519. DOI: 10.1117/12.2008830.

[12] Z. Lochner, T.-T. Kao, Y.-S. Liu, X.-H. Li, M. M. Satter, S.-C. Shen, P. D. Yoder, J.-H. Ryou, R. D. Dupuis, **Y. O. Wei**, H. Xie, A. M. Fischer, and F. A. Ponce. *Deep-ultraviolet lasing at 243 nm from photo-pumped AlGaN/AlN heterostructure on AlN substrate.* Applied Physics Letters, 14 March 2013, Vol. **102**, 101110. DOI: 10.1063/1.4795719.

[13] Y. Shen, R. K. Singh, S. Sanghavi, **Y. Wei**, R. V. Chamberlin, B. H. Moeckly, J. M. Rowell and N. Newman. *Characterization of Josephson and quasi-particle currents in MgB_2/MgB_2 and Pb/Pb contact junctions. Supercond. Sci. Technol.* **23**, 075003 (2010)